

Fluctuations in freely suspended
smectic-A films

ISBN 90-9010608-1

subject headings: liquid crystals/freely suspended smectic-A films/fluctuations/
(diffuse) x-ray reflectivity

Omslag: Jacco Farla

Fluctuations in freely suspended smectic-A films

Fluctuaties in vrijstaande smectisch-A films

(met een samenvatting in het Nederlands)

Proefschrift

ter verkrijging van de graad van doctor aan de Universiteit Utrecht op gezag van de Rector Magnificus, Prof. dr. J. A. van Ginkel, ingevolge het besluit van het College van Decanen in het openbaar te verdedigen op dinsdag 3 juni 1997 des namiddags te 2.30 uur

door

Elisabeth Anna Lucia Mol

geboren op 14 augustus 1967 te Breda

Promotores: Prof. dr. ir. W. H. de Jeu
Open Universiteit Heerlen en
FOM-Instituut voor Atoom- en Molecuulfysica te Amsterdam

Prof. dr. D. Frenkel
Faculteit der Scheikunde van de Universiteit Utrecht en
FOM-Instituut voor Atoom- en Molecuulfysica te Amsterdam

The work described in this thesis was performed at the FOM-institute for Atomic- and Molecular Physics, Kruislaan 407, 1098 SJ Amsterdam. The work is part of the research program of the Stichting voor Fundamenteel Onderzoek der Materie [Foundation for Fundamental research on Matter (FOM)] and was made possible by financial support from the Nederlandse Organisatie voor Wetenschappelijk Onderzoek [Netherlands Organisation for the Advancement of Research (NWO)].

Contents

1	Introduction	9
1.1	Liquid crystals	9
1.2	Ordering	12
1.3	Fluctuations	13
1.4	Freely suspended films	16
1.5	This thesis	17
2	X-ray reflectivity	19
2.1	Introduction	19
2.2	Fresnel theory	20
2.3	Dynamical theory	23
2.4	Scattering in the Born approximation	26
2.5	Rough interfaces	28
2.6	The model	31
3	Experimental	35
3.1	The two-circle diffractometer	35
3.1.1	The x-ray source	35
3.1.2	The diffractometer	36
3.1.3	Scan types	40
3.1.4	Corrections to the data	43
3.1.5	Resolution	45
3.2	The (2+2) diffractometer	49
3.2.1	The (2+2) surface scattering setup	49
3.2.2	Scan types	52
3.2.3	Corrections to the data	53

3.2.4	Resolution	54
3.3	The sample and its environment	55
3.3.1	Sample preparation	55
3.3.2	Sample holders	56
3.3.3	Sample ovens and temperature control	57
3.4	Appendix	59
3.4.1	The spectrometer	59
3.4.2	Alignment of the sample	60
4	Elastic theory	63
4.1	Introduction	63
4.2	Bulk smectic-A systems	64
4.3	Freely suspended films	68
4.4	The elastic constants	72
5	Conformal thermal fluctuations	79
5.1	Introduction	79
5.2	Experimental	81
5.2.1	Sample preparation	81
5.2.2	Scattering configuration	82
5.3	Intensity calculation	82
5.4	Fitting parameters	84
5.5	Experimental results	86
5.6	Discussion	88
5.7	Conclusions	93
6	Loss of conformality	95
6.1	Introduction	95
6.2	Experimental	97
6.2.1	The sample	97
6.2.2	Scattering configuration	98
6.3	Thinning transitions	99
6.3.1	Results	99
6.3.2	Discussion	100
6.4	Loss of Conformality	103
6.4.1	Results	103

6.4.2	Discussion	105
6.5	Conclusions	109
7	The molecular formfactor	111
7.1	Introduction	111
7.2	Experimental results	113
7.3	Discussion	116
7.4	Conclusions	120

1

Introduction

1.1 Liquid crystals

Although the existence of liquid crystals has been known for over a century now, the interest in the field seems undiminished. A vast amount of experimental results has emerged during the past decades. This is partly due to the present availability of powerful experimental light sources, such as *e.g.* lasers and synchrotron radiation facilities. Not to be neglected, however, is the stimulus from the applications of liquid crystals in displays. The way liquid crystals orient in an electric field combined with their high mobility makes them very suitable for this purpose. The aim of improving displays has stimulated research on the interaction of liquid crystals with various surfaces. Practically, many of the applications of liquid crystals involve devices composed of thin layers. However, thin liquid crystalline films are of interest both for practical and fundamental reasons. Fundamentally, liquid crystals have been studied extensively as experimental model systems, as they provide a variety of different phases and phase transitions. The availability of films of variable thickness allows the study of the crossover from three to two dimensional behaviour, as well as the influence of the surfaces on the morphology and phase behaviour.

Central in this thesis are x-ray reflectivity studies of freely suspended liquid crystalline films. In this first chapter I hope to justify the work which is presented,

but before doing so, some definitions have to be made. The first of which is the term liquid crystal. Liquid crystalline phases possess, as the name strongly suggests, mechanical and symmetry properties intermediate between those of a solid and a liquid. They are formed when an organic solid does not melt directly from the crystalline into the isotropic phase, but undergoes transitions to liquid crystalline or mesomorphic phases (mesomorphic: of intermediate form) [1, 2]. Not all compounds can exist in a liquid crystalline phase, the molecules must be either elongated or disk-like. Several types of compounds can form these phases: small elongated or discoid organic molecules, polymers and self-assembling structures such as soap-water systems. The work presented in this thesis is restricted to

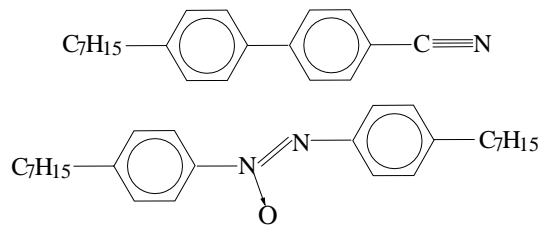


Figure 1.1: *Structure formulas of two extensively studied liquid crystals with a rigid core of phenyl rings, an alkyl chain and a cyano group: 4,4'-heptyl-cyanobiphenyl (7CB) (top) and two flexible alkyl chains: 4,4'-diheptyl-azoxybenzene (7AB) (bottom).*

small elongated molecules, two examples of which are shown in Fig. 1.1. In those molecules the core of phenyl rings can be regarded as more or less rigid, while the alkyl chains are relatively flexible. Typical lengths of the molecules are 20-30 Å, while the width is approximately 5 Å.

Having outlined which types of systems form a liquid crystalline phase, it is useful to look at the distinctions between solids, liquids and liquid crystals. In a solid the centres of gravity of the molecules are located on a three dimensional (3D) lattice. Thus, the positional correlation between two layers approaches a constant in the limit of infinite separation. In the case of elongated molecules long-range orientational order of the long axes of the molecules exists as well, as pictured in Fig. 1.2. In a liquid the centres of gravity of the molecules are not ordered, nor does long range orientational order of the axes exist, this is pictured in Fig. 1.2 as well. Therefore, the order will be short range and the correlation lengths decay exponentially, typically over some molecular dimensions. When a

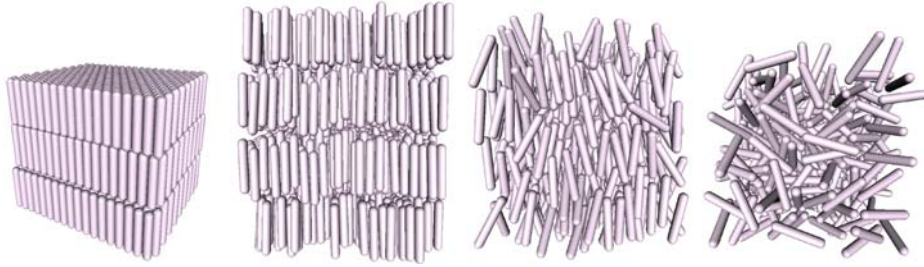


Figure 1.2: *Schematic representations of some of the different phases that can be distinguished in liquid crystalline materials. From left to right: a solid, a smectic-A phase, a nematic and a liquid. For simplicity the elongated molecules are represented as rods.*

crystal melts into a liquid crystalline phase, however, some order will be retained. In the case of the lowest ordered liquid crystalline phase, nematic liquid crystals (N), the positional order is lost, while the orientation of the long axes of the rod-like molecules is on average along a preferred direction (see Fig. 1.2). This direction is specified by a unit vector named the director \mathbf{n} . The direction of \mathbf{n} is arbitrary, and is often imposed by external fields or by the substrate and walls. The length scales ξ over which the correlations in the position of the centres of gravity of nearby molecules decay is liquid-like, aside from the anisotropy: $\xi_{\parallel} \neq \xi_{\perp}$. The indices indicate the directions parallel and perpendicular to \mathbf{n} . The nematic phase is (usually) uniaxial, *i.e.* all the directions orthogonal to \mathbf{n} are indistinguishable. Moreover, \mathbf{n} and $-\mathbf{n}$ are equivalent, thus, asymmetric molecules have an equal probability to point their heads up or down. Finally, the molecules must be achiral, or if not, the whole system must be racemic. Optically active molecules give rise to phases with additional chiral ordering, such as the cholesteric phase which has a helical structure. However, these molecules are not considered in this thesis. Nematic liquid crystals are widely used in liquid crystalline displays.

When a nematic is cooled, smectic phases can appear, while some liquids freeze directly into a smectic phase. Likewise, compounds exist that do not possess a smectic phase. Several types of smectic phases can exist, which all have a layered structure in common. In this thesis only the Smectic-A (SmA) phase will occur, while the Smectic-C (SmC) phase will be briefly mentioned. In the SmA phase the director is perpendicular to the layers and parallel to the z direction, as shown in Fig. 1.2, while it has a constant uniform tilt angle with respect to z in the

SmC phase. The SmA phase is still uniaxial, while the SmC phase is biaxial. Both the SmA and SmC phase can be described as a one-dimensional stacking of equidistant two-dimensional liquid layers. Thus, long-range orientational order of the elongated molecules exists, while the translational order is lost in the two directions perpendicular to z . Like nematics, smectic phases can be oriented by adjoining walls, such as substrates. Also, the anisotropy of the physical properties, such as the index of refraction, with respect to directions parallel or perpendicular to \mathbf{n} , is maintained.

On further cooling hexatic smectic phases can occur. In this case the molecules are located on a triangular 'lattice', the positional order decays over distances not larger than a few 100 Å. Although long-range bond orientational order exists, each layer is still a two-dimensional liquid [1]. Orthogonal as well as tilted hexatics exist. In general, tilted phases appear at lower temperatures than orthogonal phases. Finally, smectic phases possessing true long-range three dimensional positional and orientational order exist. Those systems consist of three dimensional stacks of layers that are weakly attached to each other. Although it is relatively easy to impose plastic deformations, they are in fact true crystals [1, 2].

1.2 Ordering

As both the nematic and SmA phase are uniaxial, and assuming effectively uniaxial molecules, the orientational distribution function $f(\theta)$ of the long axes of uniaxial molecules depends on the angle θ between those axes and \mathbf{n} . The degree of orientational alignment can be described by the nematic order parameter S , which because z and $-z$ are equivalent, is defined as

$$S = \left\langle \frac{3}{2} \cos^2 \theta - \frac{1}{2} \right\rangle = \frac{1}{2} \int_{-1}^1 (3 \cos^2 \theta - 1) f(\theta) d \cos \theta. \quad (1.1)$$

In the isotropic phase $S = 0$, in the crystalline phase $S \approx 1$, while in the nematic phase $S \approx 0.3 - 0.7$ [2], growing to $S \approx 0.7 - 0.9$ in the smectic phase.

Several types of SmA phases exist. In 'the' SmA phase the molecules are up-down symmetric in the layers. Therefore, the layer spacing d is approximately equal to the molecular length l . An example of a molecule forming such a phase is 7AB, which is pictured in Fig. 1.1. When strong dipoles are present at the end of a molecule, such as in 7CB shown in the top of Fig. 1.1, the formation of a dimer SmA_d phase with a partial overlap, so that $l < d < 1.5l$, can be energetically

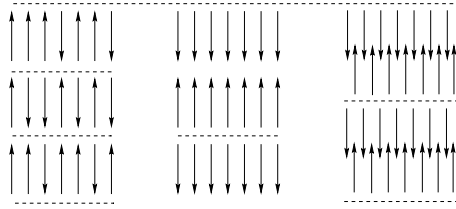


Figure 1.3: *Different types of SmA phases that differ in up-down ordering. The arrows represent asymmetric molecules. Shown are the SmA, the SmA₂ and the SmA_d phase, respectively.*

favourable. The formation of an SmA_d phase depends on the competition between a more favourable dipolar energy and a lower packing entropy. Alternatively, an anti-ferroelectric SmA₂ phase exists with polarised layers of alternating orientation and a periodicity $d = 2l$. The various SmA phases are shown in Fig. 1.3¹.

1.3 Fluctuations

Three-dimensional solids exhibit true long-range order; the particles vibrate around well-defined 3D lattice positions with an amplitude small compared to the layer spacing. The translational order as it exists in a solid can not exist in two dimensions, it would be destroyed by thermal fluctuations. As the dimensionality is decreased, fluctuations become more and more important [3]. In one dimension fluctuations destroy all long-range order. The spatial dimension at which thermal fluctuations prevent the existence of long-range order is the lower marginal dimensionality. Two-dimensional behaviour is expected if the correlation length in one direction is much smaller than those in the other two directions. A lower marginal dimensionality of two is found for solids and many other systems [4]. In these cases, the positional correlation decays algebraically as a function of distance [3].

SmA and SmC liquid crystals are other examples of systems with a lower marginal dimensionality of two, but contrary to the above case, they are 3D systems. For these systems as well the correlation function decays algebraically as $\mathbf{r}^{-\eta}$ [5], where η is small and positive. The correlation function can be studied by x-ray scattering. While a solid shows true δ -function Bragg peaks with diffuse tails, for 2D systems algebraic decaying singularities have been observed [6, 7].

¹The SmA₁ and the Sm \tilde{A} will not be discussed in this thesis

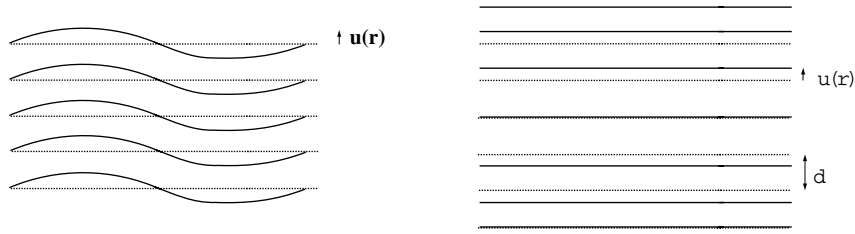


Figure 1.4: *The bending and compression of the smectic layers, which are characterized by the elastic constants B and K , respectively. The displacement of a layer from its equilibrium position is indicated by $u(\mathbf{r})$.*

The long-range order is destroyed by the thermal fluctuations of the system. The thermal fluctuation modes in smectics are the bending and compression of the layers, characterized by the elastic constants K and B , respectively, as shown in Fig. 1.4. Although the algebraic decay is slow, in the thermodynamic limit the mean square layer displacement diverges. If $u(\mathbf{r})$ is the layer displacement from its equilibrium position, $\langle u^2(\mathbf{r}) \rangle$ is found to diverge logarithmically with sample size (Landau-Peierls instability) [2], as will be discussed in detail in sec. 4.2:

$$\langle u^2(\mathbf{r}) \rangle \sim \frac{T}{\sqrt{KB}} \ln\left(\frac{L}{d}\right). \quad (1.2)$$

Here L is the thickness of the system and T the temperature. A similar divergence due to long wavelength modes makes the 2D crystals unstable [3].

The mass density distribution normal to the smectic layers, along z , can be

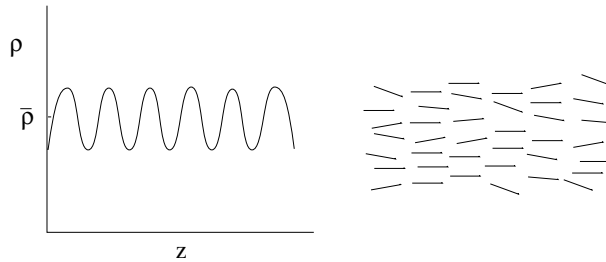


Figure 1.5: *Schematic of smectic layers and the electron density projected on the z axis. The SmA and SmC phase can be considered as a 1D mass density wave in a 3D liquid.*

developed in a Fourier series [1, 3]

$$\rho(z) = \bar{\rho} + \sum_{n=0}^{\infty} \rho_n \cos(nq_0z), \quad (1.3)$$

where $\bar{\rho}$ is the average density and $q_0 = 2\pi/d$ is the period. This is sketched in Fig. 1.5. This density profile can be considered as a convolution of the molecular formfactor of a single layer and the molecular distribution function of the centres of gravity [8]. The formfactor depends on the average conformation and orientation of the molecules, while the distribution function depends both on the collective displacement of the layers and the individual motion of molecules. The latter can generally be written as a Fourier series

$$f(z) = \sum_n \tau_n \cos(nq_0z), \quad (1.4)$$

where τ_n are the translational order parameters and $n \neq 0$. They are defined by

$$\tau_n = \langle \cos(nq_0z) \rangle. \quad (1.5)$$

Obviously, $\tau_n = 0$ in nematics. The lowest order parameter, τ_1 , is related to the amplitude of the sinusoidal harmonic of the density modulation. It is usually called *the* smectic order parameter, which is however only correct if the contribution of the higher harmonics to the density modulation can be neglected. The next order parameter τ_2 indicates the deviation from the sinusoidal form, *i.e.* it measures the 'sharpness' of the smectic layering [9].

The smectic order parameter at the surface of a liquid crystalline system can be higher than the one in the bulk [10], as surfaces enhance ordering. For not only substrate-molecule interactions result in surface induced positional and orientational order [11], even the free surface of a liquid crystal enhances positional ordering [11, 12]. This in contrast to solids which exhibit quite often surface-induced disorder. Thus, in the case of liquid crystals surface freezing [13–16] rather than surface melting [17, 18] occurs. An explanation is the breaking of spatial symmetry by the surface, so that for example in a nematic liquid crystal the translational invariance is broken by the surface. Thus, the centres of mass of the molecules nearest to the surface have a tendency to be located in a plane parallel to the surface. The intermolecular interactions due to this layer result in the formation of a second one, so that eventually several smectic layers can be formed [11].

1.4 Freely suspended films

A unique property of smectic liquid crystals is the ability, due to their layered structure, to form films that are freely suspended or free-standing over an aperture in a frame. In a freely suspended film the smectic layers align parallel to the two air-film surfaces, which tend to be flat as the surface tension minimizes the surface area of the film. Apart from the edges such films can be considered as substrate free. Thus, in essence the films can be seen as membranes consisting of several smectic layers. This property of smectics has been known since the beginning of this century [19], but the interest in freely suspended smectic films was renewed in the seventies by a series of optical experiments [20, 21]. These experiments were followed by numerous calorimetric, mechanical, hydrodynamical and x-ray studies, a number of which are collected in ref. [22].

The films have a high degree of uniformity, the orientational alignment of the molecules is almost perfect, allowing to study single domain samples of various thicknesses. The surface area can be as large as to several cm^2 , while the thickness of free-standing films can be easily varied from thousands of molecular layers (some μm) down to two layers (60 \AA)². Films of hundreds of layers can be considered as bulk systems. Thus, besides the influence of the surfaces on the physical properties, the crossover from 3D to 2D behaviour can be studied by changing the ratio of surface and volume. In fact, in studies of freely suspended crystalline smectic films the effects of reduced dimensionality have been found to be in competition with the surface enhanced order [4, 25, 26].

Experimental observations of surface enhanced ordering in freely suspended films are numerous [11, 12, 27]. Several reconstructions of the surface layers are possible. Well-known is the existence of a different phase in the boundary layers, which corresponds to a lower temperature phase of the material [25], compared to the interior of the film. However, evidence for the appearance of new phases in the surface layers, that are non-existent in the bulk system, exists as well [25]. Another possibility is the occurrence of a higher smectic order parameter in the surface layers compared to the interior of the film. This can cause a change in the nature of the phase transitions, from first to second order, as well as a shift of the transition temperature [12, 27].

The presence of the surfaces influences both the structure and the thermal

²Although one layer films were reported previously, *e.g.* in refs. [21, 23, 24], we never managed to make them.

fluctuations of a smectic liquid crystalline film. Recently continuum models which describe the thermal fluctuations in freely suspended films have been developed [28, 29]. Besides the bending and compression of the layers the surface tension is taken into account in those models. The theory predicts that the surface tension can either suppresses or enhance the amplitude of the fluctuations at the surface, compared to the interior of the film. Therefore, understanding the properties of the surfaces is crucial. Experimentally the fluctuations in freely suspended films have been hardly investigated. The aim of this thesis is to present measurements of the correlations between the thermal fluctuations of freely suspended films. It will be shown, in agreement with the theory, that at large in-plane length scales all the layers in a freely suspended film fluctuate 'conformally', *i.e.* in unison, while at shorter in-plane length scale the fluctuations of top and bottom are independent. An example of conformally undulating layers is displayed in Fig. 1.4.

1.5 This thesis

The correlations in the fluctuations have been studied using a combination of specular and diffuse x-ray reflectivity. The specular reflectivity is sensitive to the change in the index of refraction on either side of an interface. An x-ray beam that hits an interface under an angle θ_i will be reflected under the same angle ($\theta_i = \theta_o$). In layered films interference of reflected waves will occur as given by Bragg's law: $2d \sin \theta = n\lambda$, where λ is the wavelength of the x-rays. Therefore, specular reflectivity reveals both the layer spacing d and the film thickness L .

Of course, interfaces are never perfectly smooth: single crystal surfaces may have steps, polycrystalline surfaces may have a distribution of facet heights and orientations, surfaces can be warped or curved and in the case of liquids and liquid crystals thermally induced fluctuations occur. All these phenomena produce roughness over a range of in-plane length scales. Surface roughness contributes lateral modulations to the electron density profile of the sample and causes x-rays to be scattered in non-specular or diffuse directions ($\theta_i \neq \theta_o$).

In the case of freely suspended films the roughness is only determined by the thermal layer fluctuations. This is contrary to the case of substrate-film interfaces, where the roughness of the film is induced by the shape of the substrate. Thus, measurement of the diffusely scattered intensity of freely suspended films as a function of in-plane distance gives direct information about the thermal fluctua-

tions of the interfaces. Furthermore, the interference of diffusely scattered x-rays reveals the correlations between the fluctuations of the different layers. Thus, this technique is sensitive to the degree of conformality of a fluctuating film.

The correlations between the thermal fluctuations have been studied in freely suspended films of various thicknesses. Two systems are addressed; the first is a fluorinated liquid crystal which is stiff. As a consequence the compressional elastic constant B is large. The second system is an azoxybenzene studied close to a second-order SmA-N phase transition, thus in a regime where the interior of the film is expected to be less ordered than the outer layers, and where B is expected to be small. These differences between the two systems will be shown to have a strong influence on the behaviour of the fluctuations of the layers, which depends only on the surface tension and the elastic constants for compression and bending of the layers. It will be shown that films of the fluorinated compound are highly conformal, even at short in-plane distances, while in the second case a crossover to independent fluctuations of top and bottom layers has been observed.

The outline of this thesis is as follows: Chapter 2 starts with an introduction to the theory of x-ray reflectivity. It concludes with the model to calculate the scattered intensity of freely suspended films, which has been used in the analysis of the data. In chapter 3 the x-ray scattering setups used in the experiments will be described. Most experiments were performed in-house, and some at the European synchrotron radiation facility in Grenoble. It will be shown that the specific scattering geometry used in the latter case allowed us to probe in-plane distances as small as the molecular distance. This chapter also contains a discussion on the choices for the experimental resolution, which allows to model the scattered intensity without separating the specular and diffuse contribution.

The continuum model used to describe the correlations between the thermal fluctuations is central to chapter 4. It predicts the in-plane length scales at which top and bottom of the film fluctuate in unison. The final model used to calculate the scattered intensity, using the resolution function from chapter 2 and the correlation function from chapter 4, is applied to the analysis of the data of the fluorinated liquid crystal in chapter 5 and the azoxybenzene in chapter 6. The combination of specular and diffuse scattering allows the separation of the thermal fluctuations and the molecular formfactor. Finally, the consequences of the model chosen for the molecular formfactor used in the analysis of the data will be discussed in chapter 7.

2

X-ray reflectivity

This chapter introduces the theory of x-ray reflectivity. The exact dynamical model and the Born approximation of the calculation for the electron density profiles of smooth surfaces. An exact model for the scattering from rough surfaces is given within the Born approximation.

2.1 Introduction

X-rays interact with electrons through electromagnetic forces. When a beam of x-rays passes through a medium where electron density variations are present, a fraction of the x-rays will scatter out of the forward direction. In the scattering process the electrons in the medium can be regarded as free electrons due to the high energy of the x-ray photons. For the systems addressed in this thesis the scattering is assumed to be elastic, *i.e.* the photon energy E , or wavelength λ , remains unchanged in the process.

In the case of a planar interface the scattering is described in terms of reflection and we speak of x-ray reflectivity. In the last decade x-ray reflectivity has emerged as a powerful non-destructive technique in studying the properties of surfaces and interfaces, such as solid-vapour [30, 31] and liquid-vapour interfaces [32–35]. Of particular interest in our situation are the studies on the structure of liquid crystalline samples [15, 22, 36], polymer films [37], and freely suspended liquid

crystalline films [38, 39]. X-ray reflectivity provides information on the thickness of a film, the electron density gradients perpendicular to the interfaces and the roughness of the interfaces. It allows the study length of scales varying from 0.1 Å-1 μm . Reviews on x-ray reflectivity can be found in refs. [28, 36, 37, 40–44]. Recently, the diffuse scattering of surfaces has gained much interest [42, 45–50]. While specular scattering is sensitive to the laterally averaged electron density profile, the diffuse scattering provides information on the height-height correlations of an interface, *i.e.* on the in-plane structure.

In general, the distribution of the scattered intensity can be related to a model of the electron density distribution in the film, via an inverse Fourier transformation. However, phase information is lost and therefore a unique solution is usually not available. Theoretical descriptions of x-ray reflectivity can be classified in two groups; the dynamical and kinematical methods. The exact dynamical approach, using Maxwell's equations, was originally derived by Parrat [51]. In the kinematical approach, or Born approximation, refraction and multiple scattering are neglected [36, 45]. In this chapter we will briefly discuss the theory of x-ray reflectivity, starting in the next section with the exact Fresnel theory for the reflection from a sharp and flat interface. Next, we will extend this to reflection from layered systems, still using dynamical theory. Subsequently, the Born approximation is discussed in section 2.4. Finally, the roughness of interfaces will be taken into account within the Born approximation, resulting in the model for the scattered intensity used in the analysis of the data presented in this thesis.

2.2 Reflectivity from a sharp, flat interface: Fresnel theory

The scattering of a plane wave incident on a flat interface can be described in terms of a macroscopic index of refraction n , which characterizes the average properties of radiation on either side of the interface

$$n \approx 1 - \delta + i\beta. \quad (2.1)$$

where $\delta = \rho_e r_e \lambda^2 / 2\pi$, in which ρ_e is the electron density and r_e is the classical radius of the electron, and $\beta = \mu \lambda / 4\pi$, where $1/\mu$ is the absorption length of x-rays in the medium. For the materials addressed in this thesis the index of refraction

is only slightly less than one, with typical values for δ and β of the order of 10^{-6} and 10^{-8} , respectively.

Figure 2.1a pictures an interface in the (x, y) plane separating two regions of constant index of refraction, n_1 and n_2 . Thus, the electron density variation is a

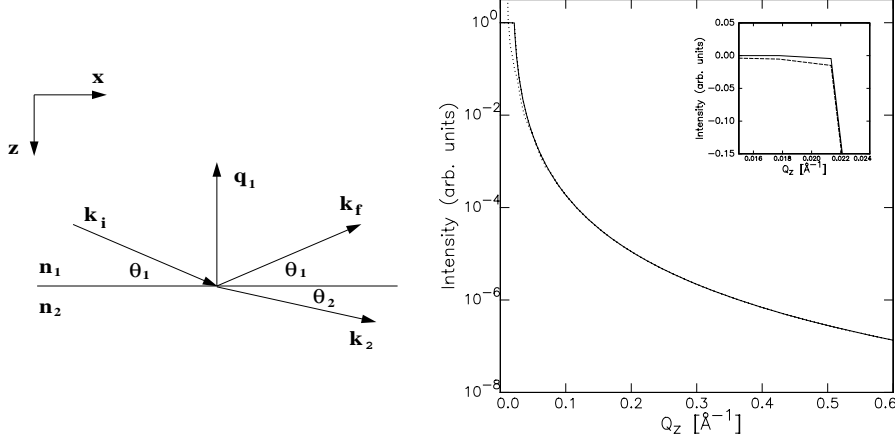


Figure 2.1: *Schematic of the scattering geometry for reflection of light with incident angle θ_1 on an interface separating two materials with indices of refraction n_1 and n_2 (left), and (right) reflectivity of a sharp, flat single interface in vacuum. The solid line is the exact reflectivity given by Eq. (2.6) and the dotted line is the approximation Eq. (2.10). The inset shows the effect of absorption on the reflectivity near the critical angle. In the calculation $\delta_2 = 4 \times 10^{-6}$ and $\beta_2 = 1 \times 10^{-8}$ is used.*

step function across a flat, smooth interface. X-rays with wave vector \mathbf{k}_i , where $k_i = 2\pi/\lambda$, are incident at glancing angle θ_1 . The outgoing x-ray beam is partly reflected at an angle θ_1 and partly refracted at an angle θ_2 . The wave vector of the reflected wave, \mathbf{k}_f , is in the plane of the incident wave vector and the surface normal. For elastic scattering $|\mathbf{k}_i| = |\mathbf{k}_f| = |\mathbf{k}|$ and the wave vector transfer is given by $\mathbf{q}_1 = \mathbf{k}_f - \mathbf{k}_i$, where $q_1 = 2k \sin \theta_1$. In general, we can write for medium j

$$q_j = 2k_j \sin \theta_j . \quad (2.2)$$

The incident and refracted angle are related by Snell's law of refraction, which

states that

$$n_1 \cos \theta_1 = n_2 \cos \theta_2 \quad (2.3)$$

When the incoming angle is smaller than the critical angle, $\theta_1 < \theta_c$, the incident wave is totally reflected from the interface, *i.e.* $\theta_2 = 0$ and only an evanescent wave is travelling parallel to the surface. It is clear from Eq. (2.1) that in the case of x-rays the critical angle exists for a transition from a more dense to a less dense medium, opposite to the case of visible light. For the liquid crystalline materials in this thesis $\theta_c \approx 0.15^\circ$ for $\lambda = 1.54 \text{ \AA}$, and the $1/e$ penetration depth of the x-ray is, neglecting absorption, $\Lambda = (2k\sqrt{\theta_c^2 - \theta_1^2})^{-1} \approx 50 - 400 \text{ \AA}$. For small angles, since $1 \gg \delta \gg \beta$, Eq. (2.3) gives $\cos \theta_c = 1 - (n_2/n_1)^2$, which can be approximated by

$$\theta_c \approx \sqrt{2\delta_2 - 2\delta_1}. \quad (2.4)$$

This simplifies to $\theta_c \approx \sqrt{2\delta_2}$ in the case of an interface between vacuum and a non-absorbing medium, where $n_1 = 1$ and $n_2 < n_1$.

The wave vector transfer in the second medium can be obtained using Eq. (2.3) and $n_1\lambda_1 = n_2\lambda_2$ and is given by

$$q_2^2 = q_1^2 - q_c^2. \quad (2.5)$$

The standard derivation from optics leads to the Fresnel law [52] for parallel polarization

$$R_F = \left[\frac{n_1 \sin \theta_1 - n_2 \sin \theta_2}{n_1 \sin \theta_1 + n_2 \sin \theta_2} \right]^2, \quad (2.6)$$

$$T_F = \left[\frac{2n_1 \sin \theta_1}{n_1 \sin \theta_1 + n_2 \sin \theta_2} \right]^2, \quad (2.7)$$

where the reflectivity R_F is defined as the ratio of the intensities of the reflected and the incoming beam and the transmission T_F as the ratio of transmitted and incident beam. Using Eq. (2.5) and (2.6) we can write

$$R_F = \left[\frac{1 - \sqrt{1 - (q_c^2/q_1^2)}}{1 + \sqrt{1 - (q_c^2/q_1^2)}} \right]^2 \approx \left[\frac{q_c}{q_1 + q_2} \right]^4, \quad (2.8)$$

$$T_F = \left[\frac{2}{1 + \sqrt{1 + (q_c^2/q_1^2)}} \right]^2. \quad (2.9)$$

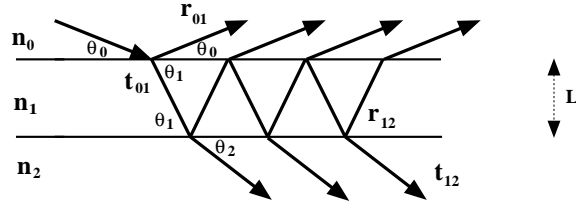


Figure 2.2: Schematic representation of multiple reflections from a smooth thin film of thickness L .

In the limit $q_1 \gg q_c$ refraction is negligible; $q_1 \approx q_2$ and Eq. (2.8) can be expanded. Neglecting higher orders we get

$$R_F \approx \left[\frac{q_c}{2q_1} \right]^4. \quad (2.10)$$

Thus, at large angles the reflected intensity decays as q_1^{-4} . We will later see that this behaviour is reproduced in the Born approximation (see sec. 2.4). Owing to the rapid fall-off in intensity with increasing angle, the wave vector transfer range in reflectivity measurements is small. For the systems investigated in this thesis the upper limit is typically $q \approx 0.6 \text{ \AA}^{-1}$. Equation (2.6) is valid for light polarised perpendicular to the scattering plane. In the in-house experiments presented in this thesis the incident x-rays were unpolarised, which leads to a correction factor $P = [1 + \cos(2\theta)]/2$. However, at the small used angles this correction is small. Figure 2.1b shows the calculated Fresnel reflectivity for a hypothetical smooth solid or liquid interface and as the dotted line the approximation in Eq. (2.10). The effect of absorption on the Fresnel reflectivity is shown as the dotted line in the inset of this figure. The index of refraction used in the calculations is typical for liquid crystals. It is obvious that absorption plays a minor role for these systems (see sec. 2.4).

2.3 Dynamical theory

Let us now consider the case of a flat film of thickness L and uniform density, in contact with a substrate (medium 2) and vacuum (medium 0), as shown in Fig. 2.2. The reflectivity can be calculated using the dynamical matrix method, which is also known as box or slab model, derived by Parrat using optical methods

[51, 52]. For a single slab the reflectance is

$$\begin{aligned} r &= r_{0,1} + t_{0,1}t_{1,0}r_{1,2} \exp(-iq_1L) + t_{0,1}t_{1,0}r_{1,2}^2r_{1,0} \exp(2iq_1L) \\ &+ t_{0,1}t_{1,0}r_{1,0}^2r_{1,2}^3 \exp(-3iq_1L) + \dots, \end{aligned} \quad (2.11)$$

where $t_{i,j}$ and $r_{i,j}$ are the Fresnel transmission and reflection coefficients at the interface between medium i and j , q_1 is the wave vector transfer on reflection between mediums 1 and 2. Defining $q_z \equiv q_0$, the ratio of reflected to incident intensity of the total film becomes

$$R_F(q_z) = rr^* . \quad (2.12)$$

The series in Eq. (2.11) can be written as

$$r = r_{0,1} + \frac{t_{0,1}t_{1,0}r_{1,2} \exp(-iq_1L)}{1 - r_{1,0}r_{1,2} \exp(-iq_1L)} . \quad (2.13)$$

Using $t_{1,0} = t_{0,1}$, $r_{1,0} = -r_{0,1}$, and $t_{0,1} = 1 + r_{0,1}$ [40], we finally arrive at

$$r = \frac{r_{0,1} + r_{1,2} \exp(-iq_1L)}{1 + r_{0,1}r_{1,2} \exp(-iq_1L)} . \quad (2.14)$$

Figure 2.3a shows the reflectivity of a 900 Å film with sharp interfaces in vacuum ($n_0 = n_2 = 1$), thus without a substrate. The reflectivity curve exhibits a series of oscillations; the Kiessig fringes [53] which can be understood from Eq. (2.14). The phase of the reflections is $\exp(-iq_1L)$, so that constructive and destructive interference of x-rays reflected from top and bottom of the film occurs with a period $2\pi/L$. The amplitude of these oscillations depends on the electron density contrast between substrate and film and is maximum when a substrate is absent. In an experiment the resolution also has to be taken into account (see section 3.1.5).

The dynamical calculations can easily be extended to a film with electron density variations along the film normal. The electron density profile in the film can be described by slabs of constant density, which can be arbitrary or may correspond to real layers. Consider the case of N slabs, where $j = 1$ indicates the interface between film and vacuum or air and $j = (N + 1)$ the film-substrate interface. Now the reflectance between the $(j - 1)$ th slab and the j th slab is given by

$$r'_{j-1,j} = \frac{r_{j-1,j} + r_{j,j+1} \exp(-iq_jd_j)}{1 + r_{j-1,j}r_{j,j+1} \exp(-iq_jd_j)} , \quad (2.15)$$

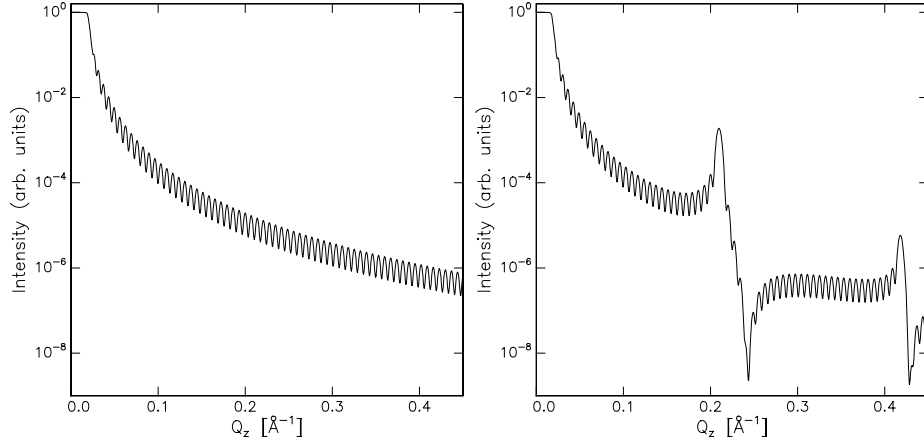


Figure 2.3: *Reflectivity of a smooth single layer film of 900 Å in vacuum, using $\delta_1 = 3 \times 10^{-6}$ and $\beta_1 = 1 \times 10^{-8}$ (left) and (right) a film with internal structure with $d=30$ Å, using $\delta_1 = 3 \times 10^{-6}$ and $\delta_2 = 2 \times 10^{-6}$, respectively, and $\beta_{1,2} = 1 \times 10^{-8}$.*

where d_j is the thickness of slab j , the prime indicates that internal reflections at the interfaces between slab $(j-1)$ and j and between slab j and $(j+1)$, respectively, are included. The reflectances are given by the Fresnel coefficients [37, 52]

$$r_{j,j+1} = \frac{q_{j+1} - q_j}{q_{j+1} + q_j}. \quad (2.16)$$

The reflectance between the $(j-2)$ th and the $(j-1)$ th layer is

$$r'_{j-2,j-1} = \frac{r_{j-2,j-1} + r'_{j-1,j} \exp(-iq_{j-1}d_{j-1})}{1 + r_{j-2,j-1}r'_{j-1,j} \exp(-iq_{j-1}d_{j-1})}. \quad (2.17)$$

Starting at the substrate this recursion is applied until the vacuum-sample interface is reached, so that finally,

$$R(q_z) = r'_{0,1}r_{0,1}^*. \quad (2.18)$$

In Fig. 2.3b the reflectivity of a smooth periodic film in vacuum with thickness L and N layers with spacing d is displayed, the Kiessig fringes and the finite size Bragg peaks determine L and d , respectively. Interference between Fresnel reflection and Bragg scattering enhances and extinguishes scattered intensity at q_z positions lower and higher than the Bragg positions, respectively.

In conclusion, the dynamical approach is valid over the full range of wave vector transfers and it takes multiple scattering, refraction and absorption properly into account. For systems with only a few repeat units in the electron density profile the slab model is quite straightforward. Problems arise if the profile is continuous, which leads to many slabs and a time consuming modelling, or if other information on the electron density profile in the film is not available.

2.4 Scattering in the Born approximation

Although the dynamical approach has the advantage of being exact, it is often acceptable to make approximations. In the first Born approximation or kinematical theory it is assumed that the amplitude of the incident wave is equal to the total wave amplitude in the medium, thus the scattered amplitude is negligible [52, 54]. For this reason multiple scattering can be neglected compared to single scattering, except for angles close to the critical angle. In the Born approximation refraction is discarded as well, which is a valid assumption for samples with low electron densities; e.g. without heavy (metal) particles. In fact, both assumptions are valid only for weakly scattering systems. We start with the neglect of multiple reflection. Within single scattering theory Eq. (2.15)-(2.17) gives for the reflectance of film with N slabs

$$r = r_{0,1} + r_{1,2} \exp(-iq_1 d_1) + r_{2,3} \exp[-i(q_1 d_1 + q_2 d_2)] + \dots + r_{N,N+1} \exp \left[-i \left(\sum_{j=1}^N q_j d_j \right) \right]. \quad (2.19)$$

Eq. (2.19) can be written as [55]

$$r = r_{0,1} \prod_j [1 + f_j \exp(-iq_j d_j)] \quad \text{with} \quad f_j = r_{j,j+1}/r_{j-1,j}, \quad (2.20)$$

where the Fresnel coefficients are given by Eq. (2.16). Note that total external reflection is not accounted for by Eq. (2.20), contrary to the exact calculation in Eq. (2.18).

The next approximation made in the kinematical theory [45, 52] is the neglect of refraction. The index of refraction is so close to unity that, except for angles near the critical angle, the refracted wave within the material is indistinguishable

from the incident wave and refraction can be discarded. Analogous to Eq. (2.5) we can write

$$q_j^2 = q_z^2 - q_{c,j}^2, \quad (2.21)$$

where $q_{c,j}$ is the critical wave vector transfer for reflection in medium j . Now Eq. (2.16) can be expanded in the limit $q_z \gg q_{c,j}$. Neglecting higher orders this gives

$$r_{j,j+1} = \frac{(q_{c,j+1})^2 - (q_{c,j})^2}{4q_z^2} = \frac{4\pi(\rho_{j+1} - \rho_j)}{q_z^2}, \quad (2.22)$$

where $q_{c,j} = (16\pi\rho_j)^{1/2}$, in which $\rho = \rho_e r_e$, as obtained from Eq. (2.4). Using Eq. (2.21) we can rewrite Eq. (2.19) as

$$r = \sum_{j=0}^N r_{j,j+1} \exp\left(-iq_z \left[\sum_{i=1}^j d_i \sqrt{1 - (q_{c,i}^2/q_z^2)}\right]\right), \quad (2.23)$$

where the exponent still contains the refraction corrected path length up to the j th slab. For $q_z \gg q_{c,i}$ the expression in the sum can be replaced by d_j , so that

$$r = \frac{4\pi}{q_z^2} \sum_{j=0}^N [\rho_{j+1} - \rho_j] \exp(-iq_z d_j). \quad (2.24)$$

In the limit of an infinite number of infinitesimally thin slabs Eq. (2.24) can be rewritten as [36, 41]

$$r = \frac{4\pi}{q_z^2} \int_{-\infty}^{\infty} \frac{d\rho(z)}{dz} \exp(-iq_z z) dz, \quad (2.25)$$

where Eq. (2.22) is inserted as well. Als-Nielsen *et al.* [36, 41] used this expression to model the electron density profile of a layered system as a Fourier series, where the number of Bragg peaks determines the number of Fourier components. In this way the number of fit parameters is minimized compared to the slab model, however multilayers with only a few or no repeat units are less suited for a representation in a Fourier series.

The Born approximation is valid in the weakly interacting limit where q_z is larger than four or five times the critical angle q_c and diverges in the regime of total reflection. In this regime the distorted wave Born approximation (DWBA) [45] can be applied. Although the DWBA correctly describes the scattering at

small momentum transfer, it fails at larger ones. For weakly scattering systems a good compromise between the Born approximation and the DWBA can be found in replacing the wave vector transfer q_z in the exponent in Eq. (2.24) by the average wave vector transfer in the film;

$$q_z'^2 = (q_z^2 - q_c^2). \quad (2.26)$$

Thus, only individual slab refraction corrections are neglected. This expression behaves well in the entire range of q_z [45]. This adjustment to the kinematical theory is taken into account in the analysis of the data. Furthermore, in order to obtain the correct positions for the Bragg angles we use in our model the single scattering slab model to calculate the Fresnel reflectivity of a single smectic layer. Therefore, the prefactor to the sum in Eq. (2.24) is replaced Eq. (2.20).

2.5 Rough interfaces

In the previous sections we have assumed the interfaces to be perfectly smooth. Of course such interfaces do not exist in reality; a few causes of roughness have been given in sec. 1.5. They all produce roughness over a range of in-plane length scales, which contributes lateral modulations to the electron density profile of the sample and causes x-rays to be scattered in non-specular or diffuse directions. Specular reflectivity is only sensitive to the laterally averaged density gradient normal to the film interfaces. It is restricted to the specular ridge, although a finite amount of diffuse scattering will be detected along with the specular since the instrumental resolution function is not a true δ function.

A useful concept in a discussion of the effect of roughness on different length scales is the lateral coherence length, as shown in Fig. 2.4. The coherence length l_c is defined as the maximum in-plane distance over which waves still interfere coherently at the detector. The coherence length in the direction out of the scattering plane can be larger than the one in the scattering plane (see sec. 3.1.5), so the area involved in coherent scattering will in general be anisotropic. If the outgoing waves are coherent, the total amplitude is the sum of the amplitudes of the individual waves. This is relevant for roughness on length scales short compared to the coherence length. The specular reflection will be weaker, since part of the light is reflected in diffuse directions. If the outgoing waves are incoherent, the measured signal is a sum of the individual intensities, resulting from different orientations

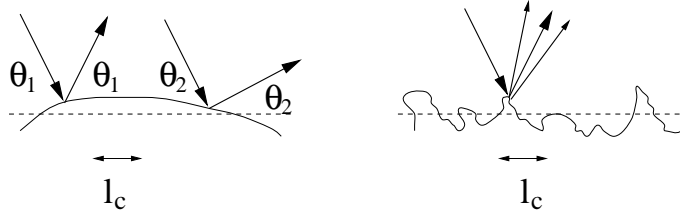


Figure 2.4: *Different types of roughness: macroscopic roughness (left), and microscopic roughness (right).*

and positions of the interface. This is relevant for roughness on length scales long compared to the coherence length; the interface is locally flat and the signal will be specularly reflected. Thus, the first case produces genuine diffuse scattering, while the second produces distortions of the specular reflectivity.

Usually the specularly reflected component of the scattering is analysed as the Fresnel reflectivity multiplied with a Debye-Waller factor which takes the roughness into account as a Gaussian broadening.

$$r_{i,j} = \frac{q_i - q_j}{q_i + q_j} \exp\left(-\frac{1}{2}q_i q_j \langle \sigma_{i,j} \rangle^2\right), \quad (2.27)$$

where $\langle \sigma_{i,j} \rangle^2$ is the mean square deviation and i and j are indices of the interfaces. Note that an expression similar to Eq. (2.27) is found for a flat graded interface where the electron density profile is an error function, as sketched in Fig. 2.5. On the basis of specular reflectivity one cannot discriminate between these two cases. However, the rough surface scatters diffusely as well, while the graded interface does not.

The diffuse component is related to the height-height correlations of the rough surface, as shown in Fig. 2.6. In the case of a freely suspended film the roughness is due to the displacement-displacement correlations between the thermal fluctuations. An estimate of the diffuse scattering is important, as the diffuse scattering is centred around the specular ridge. It becomes comparable or may become even greater than the specular reflectivity at large angles. An example of diffuse scattering is displayed in Fig. 2.7, which shows two in-plane transverse or “rocking” scans across the specular ridge for a freely suspended film. The scans were measured at the first and second Bragg peak, respectively, by varying the angles α and β with respect to the surface, while keeping $2\theta = \alpha + \beta$ equal. The presence of only a single peak in Fig. 2.7 proves the validity of the use of the Born approximation in

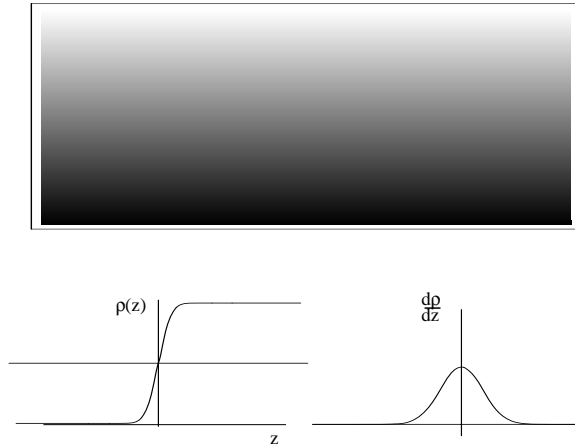


Figure 2.5: A graded interface with a continuous change in electron density across the interface.

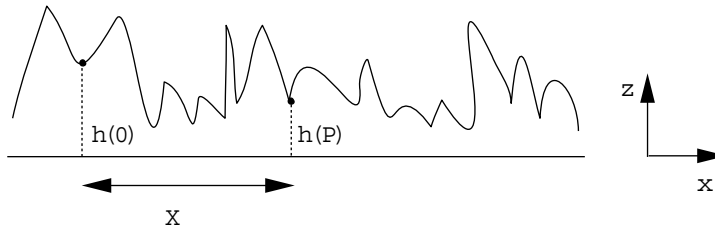


Figure 2.6: Schematic of a sharp rough surface where x is along the average surface, z is normal to the surface and $h(P)$ is the height above the surface at point P .

the case of scattering from freely suspended smectic films. For whenever α or β are equal to the critical angle θ_c extra peaks can occur on either side of the central peak. These are the so-called Yoneda or angel's wings [56]. The physical origin for these peaks lies in the fact that when α or β are equal to θ_c the electric field in the evanescent wave at the surface reaches a maximum of twice the incident field, resulting in a greater diffuse scattering. The same effect can occur when either the incident or the reflected wave satisfies a lower angle Bragg condition. Both the Yoneda wings and the Bragg-like peaks are caused by multiple scattering processes, so they have a purely dynamical nature. They can be modelled in the DWBA, which includes the complex transmittivities. Neither the Yoneda wings, nor the Bragg-like peaks appear however for these weakly scattering layered

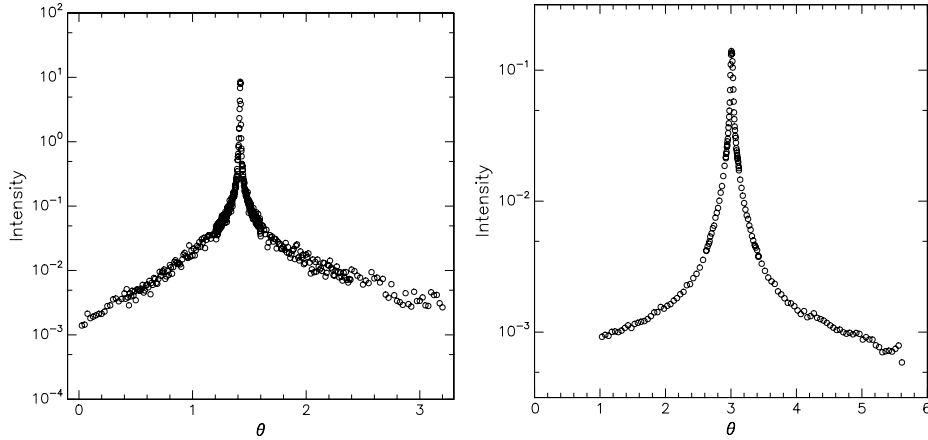


Figure 2.7: *In-plane (transverse) scans across the specular ridge at the first Bragg peak (left) and the second Bragg peak (right), for a freely suspended film of 34 layers. The central peaks are limited by the experimental resolution. Both scans were corrected for the change in illuminated area during the scan. The asymmetry in the left figure is due to the asymmetric resolution used in the experiment.*

systems.

2.6 The model

Let us first consider a rough surface, such as the one in Fig. 2.6, with displacements $h(x, y)$ from a reference smooth interface; the (x, y) plane. Within the first Born approximation the differential cross section per unit surface area for scattering as a function of \mathbf{q} is written as [45]

$$\frac{d\sigma}{d\Omega} = \Delta\rho^2 \int_V dr^3 \int_V dr'^3 \exp(-i\mathbf{q}(\mathbf{r} - \mathbf{r}')), \quad (2.28)$$

where the term $\Delta\rho$ takes the change in electron density at the surface into account. The integral is taken over the volume of material inside the coherence volume. For an enclosed volume the integral over the enclosing surface can be used instead:

$$\int_V (\nabla \mathbf{f}) d^3 = \oint_S d\mathbf{S} \cdot \mathbf{f}, \quad (2.29)$$

where $d\mathbf{S}$ represents the differential surface vector parallel to the surface normal and \mathbf{f} is an arbitrary function inside the volume. We define unit vector $\hat{\mathbf{z}}$ such that

$\mathbf{f} = \hat{\mathbf{z}} \exp(-i\mathbf{q} \cdot \mathbf{r})$. Then the integral in Eq. (2.28) becomes

$$\int_V d\mathbf{r}^3 \exp(-i\mathbf{q} \cdot \mathbf{r}) = \frac{1}{-i\mathbf{q}\hat{\mathbf{z}}} \int_V (\nabla\mathbf{f}) d\mathbf{r}^3. \quad (2.30)$$

Next we use Eq. (2.29), where $d\mathbf{S} \cdot \hat{\mathbf{z}}$ is the projection onto the (x, y) plane of the surface element dS , which is located at height $h(x, y)$ from the plane. Therefore, $\int_S d\mathbf{S} \cdot \hat{\mathbf{z}} = \int_{S_0} dx dy$, where S_0 is the coherence area of the beam on the sample. Then the differential scattering cross section can be written as

$$\begin{aligned} \frac{d\sigma}{d\Omega} &= \frac{\Delta\rho^2}{q_z^2} \int \int_{S_0} dx dy \int \int_{S_0} dx' dy' \exp(-iq_z[h(x, y) - h(x', y')]) \\ &\quad \times \exp(-i[q_x(x - x') + q_y(y - y')]). \end{aligned} \quad (2.31)$$

It is assumed that $[h(x, y) - h(x', y')]$ is a Gaussian random variable which depends on the relative coordinates $(X, Y) \equiv (x' - x, y' - y)$, so that

$$\langle \exp(-iq_z[z(x, y) - z(x', y')]) \rangle = \exp(-q_z^2 g(X, Y)/2), \quad (2.32)$$

where the correlation function $g(X, Y) = \langle [h(x, y) - h(x', y')]^2 \rangle$ has been introduced. Furthermore, $\langle h(0, 0)^2 \rangle = \sigma^2$. Therefore, the cross section per unit surface area is given by

$$\frac{d\sigma}{d\Omega} = \frac{\Delta\rho^2}{q_z^2} \int \int_{S_0} dX dY \exp(-q_z^2 g(X, Y)/2) \exp(-i[q_x X + q_y Y]). \quad (2.33)$$

Note that the integral reduces to the Fourier transform of the correlation function in the limit of small q_z . Using Eq. (2.1) the prefactor can be replaced by

$$\rho^2 \approx [\pi/\lambda^2(1 - n^2)] = q_c^4/32\pi^2 \quad (2.34)$$

and it is obvious that Eq. (2.33) can be rewritten to regain the Fresnel reflectivity for a smooth surface in the large angle limit.

Equation (2.33) is valid for a single rough surface. The derivation can easily be extended to scattering from a layered film

$$\begin{aligned} \frac{d\sigma}{d\Omega} &= \frac{\Delta\rho_m \Delta\rho_n}{q_z^2} \sum_{m=1}^N \sum_{n=1}^N \exp[-iq_z(m - n)d] \\ &\quad \times \int \int dX dY \exp[-q_z^2 g_{mn}(X, Y, z_m, z_n)/2] \exp(-i[q_x X + q_y Y]), \end{aligned} \quad (2.35)$$

where the double sum runs over all N interfaces. The correlation function

$$g(X, Y, z_m, z_n) = \langle [u_m(X, Y) - u_n(0)]^2 \rangle = 2\sigma^2 + 2\langle u_m(X, Y)u_n(0) \rangle \quad (2.36)$$

has now been defined to include correlations between different heights in one interface or between different interfaces.

In experiments absolute intensities are measured, therefore the scattering cross sections have to be summed over the detector solid angle Ω_d , *i.e.* the acceptance of the detector, and over the angular spread of the incident beam. These factors will be taken into account as a convolution with the experimental resolution R , for convenience expressed as a function of \mathbf{q} (see chapter 3)

$$\frac{I(\mathbf{q})}{I_0} = \int \frac{d\sigma}{d\Omega} R(\mathbf{q} - \mathbf{q}') d\mathbf{q}' . \quad (2.37)$$

Using the prefactor R_F obtained from Eq. (2.20), which describes the Fresnel reflectivity of a single smectic layer, and the average wave vector transfer in the film q'_z , as obtained from Eq. (2.26), we get finally

$$\begin{aligned} \frac{I(\mathbf{q})}{I_0} &= |R_F|^2 \exp(-q_z'^2 \sigma_{loc}^2) \sum_{m=1}^N \sum_{n=1}^N \exp[-iq'_z(m-n)d] \\ &\times \int \int dXdY \exp[-q_z'^2 g_{mn}(X, Y, z_m, z_n/2)] \exp(-i[q_x X + q_y Y]) \\ &* R(\mathbf{q}) . \end{aligned} \quad (2.38)$$

R_F is smeared with a Gaussian of width σ_{loc} to approximate the uncorrelated (short wavelength) contribution to the roughness. The symbol '*' indicates a convolution.

It should be noted that if correlations exist between different interfaces, the exponential term with $q_z d(m-n)$ gives the interference between diffusely scattered amplitudes. Therefore, if the roughness is conformal, *i.e.* the interfaces fluctuate in unison, the diffuse scattering will show maxima and minima, *e.g.* Bragg peaks and Kiessig fringes, at the same positions in q_z as the specular reflectivity [42, 45]. For completely uncorrelated roughness, the correlation function vanishes for $m \neq n$ and the diffuse scattering is the incoherent superposition of the diffuse scattering from the roughness of each interface. The interfaces pictured in fig. 2.8 fluctuate conformal at long length scales and non-conformal at shorter length scales. It will

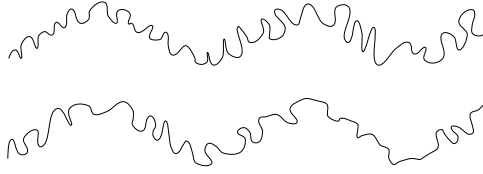


Figure 2.8: *Schematic showing two surfaces whose roughnesses are conformal on long length scales, but independent on shorter length scales.*

be clear from Eq. (2.38) that the specular reflectivity, *i.e.* $q_x, q_y = 0$, depends on the overall roughness of the film and is insensitive to whether the roughness is conformal or not:

$$\frac{I(\mathbf{q})}{I_0} = |R_F|^2 \exp(-q_z'^2 \sigma_{tot}^2) \sum_{m=1}^N \sum_{n=1}^N \exp[-iq_z'(m-n)d] * R(\mathbf{q}), \quad (2.39)$$

where $\sigma_{tot}^2 = \sigma^2 + \sigma_{loc}^2$. An explicit expression for the displacement-displacement correlation function of the thermal fluctuations of freely suspended smectic-A films will be calculated in chapter 4. The resolution function used in the analysis of the data will be discussed in the next chapter.

3

Experimental

This chapter is divided into three sections. The first section describes the in-house reflectivity setup consisting of a rotating anode and a two circle diffractometer. In order to compare the measured reflectivity with the reflectivity calculated from a model, it is necessary to include geometrical and resolution-function correction factors. The procedure to make these corrections in relation to the various scan types described is treated in some detail. The second section deals with the (2+2) surface scattering setup at beam-line BM32 of ESRF, which was used for the experiments described in chapter 6. It includes a discussion of the scan types performed and the correction factors for this setup. The emphasis is on corrections that differ from those in the two circle diffraction setup. Subsequently, in the last section the preparation of freely suspended films, the sample holders, and the two-stage ovens used are described. Finally, the chapter contains an appendix about the alignment procedure of the in house instrument.

3.1 The two-circle diffractometer

3.1.1 The x-ray source

The in-house setup consists of a x-ray generator with a rotating anode and a two circle spectrometer. X-rays are produced when high energy electrons hit the copper anode. Most of the kinetic energy of the incoming electrons is converted to heat,

Table 3.1: *Wavelengths and relative intensities of the strong intensity lines and the Bragg angles of graphite, germanium and silicon monochromators*

line	λ (Å)	k (Å ⁻¹)	intensity	Ge(111) (°)	C(002)(°)	Si(111)(°)
$K_{\alpha 1}$	1.5405	4.0787	1.0	13.642	13.264	14.221
$K_{\alpha 2}$	1.5443	4.0686	0.5	13.676	13.298	14.257
$K_{\beta 1}$	1.3922	4.5131	0.2	12.307	11.968	12.827
$K_{\beta 1}$	1.3810	4.5497	-	12.206	11.870	12.722

which can be relatively efficiently released by a rotating anode. Part of the energy is emitted as unpolarised radiation, which consists of a continuous contribution spanning a range of wavelengths with superimposed a few sharp peaks of high intensity. The continuum arises from rapid deceleration of the electrons which sink in the anode, the Bremsstrahlung. The peaks result from a process where first an incoming electron knocks out an electron of an inner shell of a copper atom, followed by an electron of a higher shell dropping into the vacancy, emitting the excess energy as x-ray radiation. The sharp lines are $K_{\alpha 1}$, $K_{\alpha 2}$, $K_{\beta 1}$ and $K_{\beta 2}$, where K indicates the shell the electron was originally removed from and the suffix α, β the original shell of the electron that fills the vacancy (α for L and β for M). Each line is split into a doublet due to spin-orbit coupling. The wavelength, λ , the wave number k and the relative intensities of the respective lines are summarized in table 3.1.

The actual x-ray source is a Rigaku RU-300H generator with a rotating copper anode, which is usually operated at 18 kW maximum power. The focal spot-size of the electron beam on the anode was $0.5 \times 10 \text{ mm}^2$. A narrow cone from the x-ray radiation emitted by the anode is selected, which makes an angle of 6° with the anode surface. Thus, the effective spot-size is $0.5 \times 1.0 \text{ mm}^2$. The generator is computer controlled via an IEEE-488 interfacing system using a program in *Basic*, which monitors the status of the generator and can restart the generator in case of power trips, turn up the power, as well as open and close the safety shutters.

3.1.2 The diffractometer

Figure 3.1 shows a top-view of the setup used in the experiments described in chapters 5 and 7. The triple axis spectrometer, originally built at Risø National

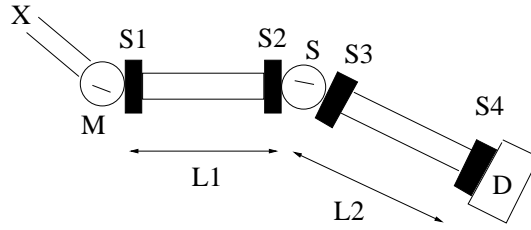


Figure 3.1: A top-view of the two circle diffractometer with x-ray source (X), bent graphite monochromator (M), 4 pairs of slits ($S1, S2, S3, S4$), the sample (S) and the scintillation detector (D).

Laboratory (Roskilde, Denmark), can be used both in a reflectivity and a transmission geometry. The latter geometry will not be described in this thesis. Following the path of the x-rays they first leave the anode housing (X) through a beryllium window, pass through an evacuated flight path and enter the monochromator housing (M). The monochromator crystal, placed on a turntable at 380 mm from the source, reflects the beam according to Bragg's law: $2d \sin \theta = n\lambda$, where d is the spacing of the lattice planes and θ the reflecting angle. The monochromator table has two additional translation modes and tilts in order to align the monochromator (see Appendix). For the work presented in this thesis, depending on the resolution required, a flat germanium (111) monochromator or a bent pyrolytic graphite (002) monochromator (radius $R = 115$ mm), each with size 20×20 mm² was used. In the latter case the monochromator is bent in the vertical plane, perpendicular to the scattering plane (along y), in order to focus the beam onto the sample. The focal length f of the monochromator is given by $f = R/2 \sin \theta \approx 250$ mm.

The Bragg angles of the two monochromators used are shown in table 3.1. The intensity gain of bent graphite compared to germanium is a factor of 100, while the resolution is a factor 10 worse. This thesis treats only the moderate resolution setup using bent graphite, while the high resolution setup using a germanium monochromator and an analyser, instead of detector slits, is extensively described in ref. [57].

The graphite monochromator is positioned so that the K_α lines are reflected, thus K_β is eliminated here. Unlike in the case of a high resolution setup $K_{\alpha 1}$ and $K_{\alpha 2}$ cannot be separated further downstream. They are both selected and a weighted average of the wave-vector is used with $|\mathbf{k}| = 4.075 \text{ \AA}^{-1}$ [58]. Next the x-ray beam enters an evacuated flight path with slits on both sides, at 60 and 510

mm from the monochromator, respectively. The slits are adjustable both in the in-plane and out-of-plane direction, defined with respect to the scattering plane, but are only motorized in the in-plane direction. The slits in front of the sample are Huber (H3013) slits, calibrated to within 10 μm . In the moderate resolution setup the in-plane divergence, indicated by i , is determined by this set of slits $S1_i$ and $S2_i$:

$$\Delta\alpha \approx \tan^{-1} \left(\frac{S1_i + S2_i}{L1} \right), \quad (3.1)$$

where $L1$ is the distance between the slits. Typical values were $S1_i = 0.3$ mm, $S2_i = 0.05$ mm and $L1 = 450$ mm, giving $\Delta\alpha \approx 0.044^\circ$ full width at half maximum (FWHM).

The sample is mounted vertically on a two-circle diffractometer, which allows the angle between the incident beam and the face of the sample (α), and the angle between incident beam and reflected beam (2θ), to be varied independently. The two turntables for α and 2θ are at the base of a column, which is placed on an air table to enable positioning of the coinciding rotation axes of the two circles in the centre of the beam. The lower turntable is attached to an arm which supports the detector. On top of the upper turntable is a cradle for tilting the sample in the xy -plane to $\pm 20^\circ$. Finally, the sample is mounted on two translation tables in the x and z direction, where the z table serves to translate the face of the sample into the centre of the beam. The distance $S2$ -sample was typically 60-70 mm.

The flight path between sample and detector again has slits on both sides. The slits $S4$ in front of the detector are again Huber slits. $S4_i$ determines the in-plane divergence $\Delta\beta$ of the outgoing beam. Assuming a point source at the sample position we can write

$$\Delta\beta \approx \tan^{-1} \left(\frac{S4_i}{L2} \right), \quad (3.2)$$

where $L2$ is the distance sample- $S4$. Typical values are $S4_i = 0.3 - 0.35$ mm and $L2 = 420$ mm so that $\Delta\beta \approx 0.044^\circ$ FWHM. The slits $S3$ behind the sample X serve to reduce the background scattering and were typically set at $S3_i = 0.7$ mm.

The slits in the out-of-plane direction were wide open, except for $S2_o$ in front of the sample. $S2_o$ determines the slice of the sample which is vertically illuminated and varied between 3-5 mm. With the above slit settings the beam-size at the sample position was approximately $0.1 \times S2_o$ mm² (H×V). The determination of

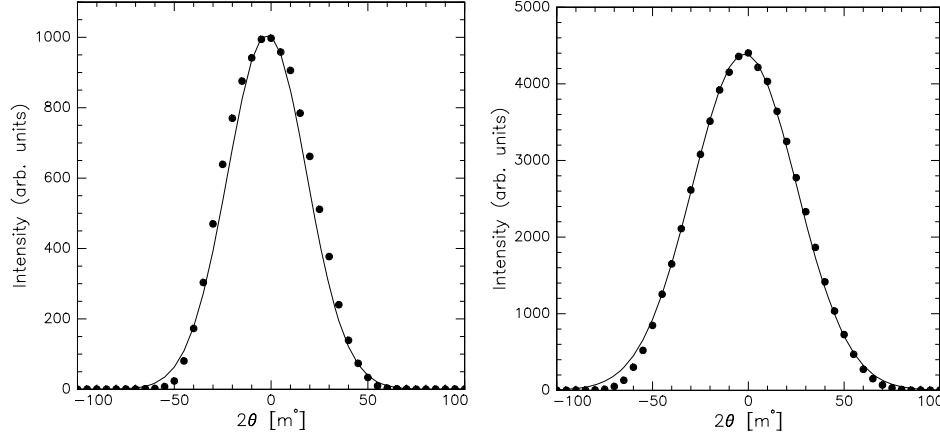


Figure 3.2: An example of the in-plane divergences fit to Gaussians for $\Delta\alpha$, measured with slits $S4_i$ narrow compared to $S2_i$ (left), and the detector scan of the main beam in situation $\Delta\alpha = \Delta\beta$ (right).

the first value is described in the Appendix. Experimentally $\Delta\alpha$ can be measured as the full width of the main beam when scanning the 2θ -arm, while the detector slits are very narrow compared to $S2_i$. $\Delta\alpha$ can be approximated as a Gaussian, as shown by the example in Fig. 3.2a. Figure 3.2b shows the main beam detector scan with the actual detector slit setting, again fit to a Gaussian. For the values given above we find $\Delta 2\theta = \sqrt{\Delta\alpha^2 + \Delta\beta^2} \approx 0.062$ FWHM.

Finally the x-rays enter the beryllium window of the NaI scintillation detector, which has a photo-multiplier attached to it. Photons absorbed in the NaI crystal cause an electric pulse as output of the photo-multiplier. The pulses are multiplied and fed into a single channel analyser [57], with an energy window set to cut of the noise of the detection system at the low energy side and to cut the higher harmonics $\lambda/2, \lambda/3$, etc. at the high energy side. A second NaI detector, or monitor, is positioned perpendicular to the scattering plane to detect scattering from a thin mylar sheet placed in the flight path just before the pre-sample slits $S2$. The mylar scatters less than 0.1% of the direct beam. The monitor serves as a measure of the incident beam intensity on the sample, as the generation of x-rays can vary over a period of time. All flight paths are sealed with kapton windows and are evacuated to reduce background due to air scattering. This enhances the intensity by approximately 15-20%. In the scattering configuration

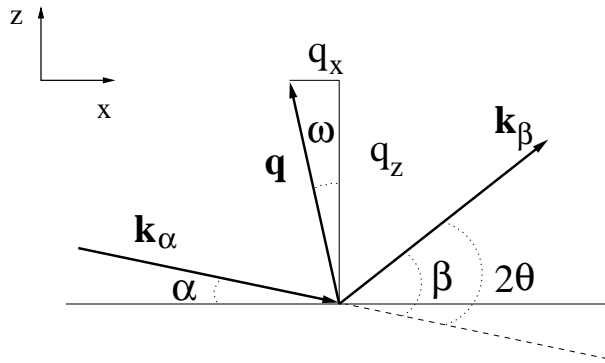


Figure 3.3: The scattering geometry; the wave vector transfer is defined as $\mathbf{q} = \mathbf{k}_\beta - \mathbf{k}_\alpha$

described, an incident main beam intensity of 8×10^7 ct/s could be obtained, while the background scattering was near dark-count levels of 0.07 ct/s. This allowed a dynamic range of nine orders of magnitude in the measured intensity.

Slow-syn stepper motors, operated by Huber SMC 9000 motor controllers, are used to position the turntables (step-size 1 m°) and translational stages (step-size $1 \text{ }\mu\text{m}$). The motor controllers and the x-ray detection system are linked to a computer via an IEEE interfacing system using an in-house written program in *Turbo Pascal 5.0* [59].

3.1.3 Scan types

A schematic of the scattering geometry is depicted in Fig. 3.3, where α and β are the angles of the incoming and outgoing wave vectors with respect to the surface of the sample and $\mathbf{q} = \mathbf{k}_\beta - \mathbf{k}_\alpha$. In general, data were obtained using three types of scans, as shown in Fig. 3.4. This allows mapping of the distribution of the scattered intensity in different cuts through reciprocal space. Figure 3.4a shows the specular reflectivity ($\theta, 2\theta$ scans), in which α and β are varied together while keeping them equal. Figure 3.4b shows transverse diffuse (rocking) scans in which ω is varied but the total scattering angle $\alpha + \beta$ is kept fixed. Finally, 3.4c depicts the radial diffuse scans where α and β are varied while the sample is offset from the specular condition by a constant angle $\omega = (\beta - \alpha)/2$. In reciprocal space, specular scans probe the scattered intensity along q_z with $q_x = 0$, in radial diffuse scans both q_z and q_x are varied, and for small angles transverse diffuse scans probe essentially

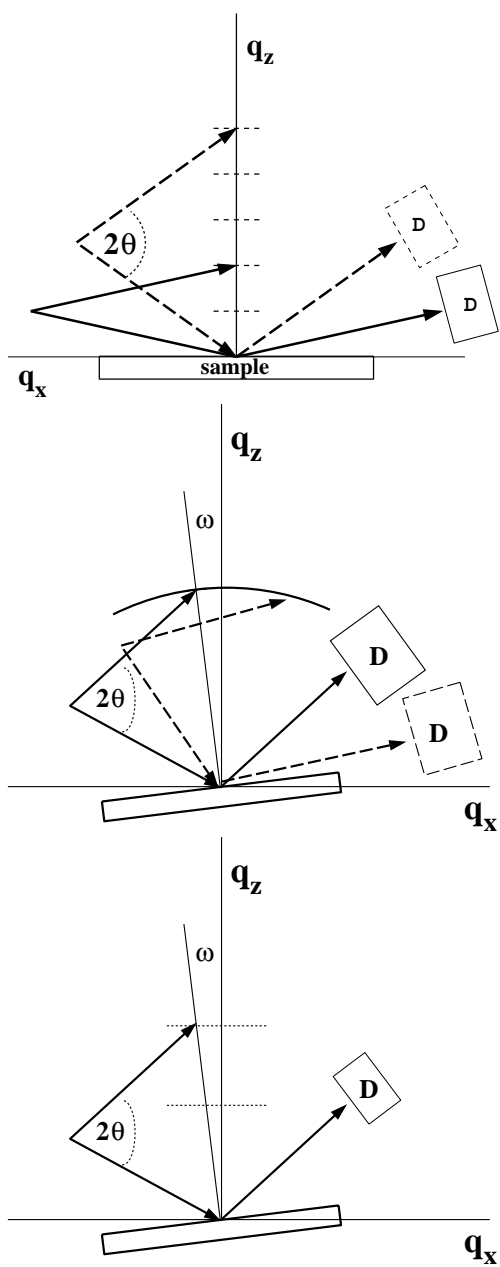


Figure 3.4: *The types of scans: specular scans along q_z (top), transverse 'rocking' diffuse scans in which ω is varied and $\alpha + \beta$ is kept fixed (middle), and radial diffuse scans where the sample is offset by a constant angle $\omega = (\beta - \alpha)/2$ (bottom).*

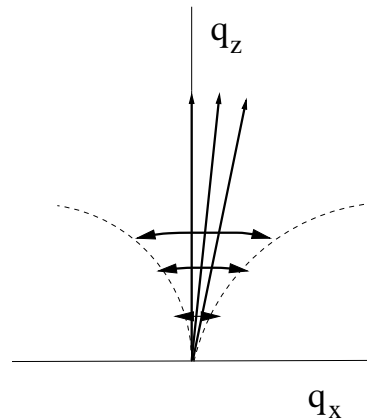


Figure 3.5: *The accessible in-plane q -range, indicated by the dashed lines, is a function of q_z in a transverse scan. Also shown are specular scans parallel to the z axis and radial diffuse scans which probe both q_z and q_x .*

along q_x at fixed q_z . Note that we define specular scans as strictly confined to the q_z axis.

In transverse scans the diffuse scattering is measured by rocking the sample in the beam, in which case an in-plane q -range limited by $\omega = \pm\theta$ is accessible before the sample surface blocks either the incident or exit beam. Thus, the accessible in-plane momentum transfer q_x depends on q_z , as illustrated in Fig. 3.5. For freely suspended films the intensity is in general too low beyond the second Bragg peak, where $q_x^{\max} \approx 0.022 \text{ \AA}^{-1}$, to perform diffuse measurements [60, 48]. Consequently at this Bragg angle the maximum values for q_x are reached.

Specular scans usually span several decades of intensity. In order not to saturate the detector, which occurs above 30.000 ct/s, a scan actually consists of several smaller scans, each at different power settings of the generator and counting times and, if necessary, attenuation. At high power the data is normalized to monitor counts, while at low power the signal is unnormalized due to insufficient statistics of the monitor signal. The transverse data presented in this thesis consist of several scans, in which the step-size was increased the larger the offset from the specular ridge.

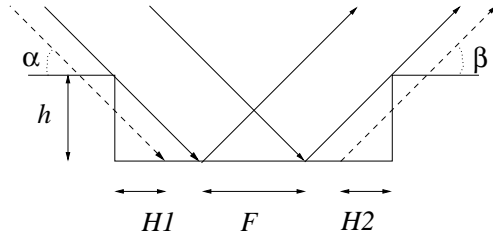


Figure 3.6: Part of the film is inaccessible as the film hangs below the holder surface.

3.1.4 Corrections to the data

The footprint F , as pictured in Fig. 3.6, of the beam on the sample is defined by

$$F = \frac{b1}{\sin \alpha}, \quad (3.3)$$

where $b1$ is the width of the beam at the sample position. Note that $b1$ will in general be larger than the pre-sample slit width $S2_i$ (see Appendix). The data have to be corrected for three geometrical effects that make the effective footprint smaller than F at small angles α and β . The first one occurs at small α when the beam overfills the sample and F is larger than the sample dimension L along the beam. For $b1 \approx 0.1$ and $L \approx 30$ mm overfilling occurs typically at $\alpha \leq 0.2^\circ$

The second effect happens when the free standing film hangs at a distance h below the surface of the sample holder, as shown in Fig. 3.6. At small α or β part of the sample will not be accessible to the incoming or outgoing beam. The inaccessible part is given by

$$H1 = \frac{h}{\tan \alpha} \quad (3.4)$$

and

$$H2 = \frac{h}{\tan \beta}. \quad (3.5)$$

Finally, the sample area visible by the detector is limited by the width $S4_i$ of the slits in front of the detector. Assuming the detector to be large and taking a parallel beam from the sample, the area seen by the detector is

$$W = \frac{S4_i}{\sin \beta}. \quad (3.6)$$

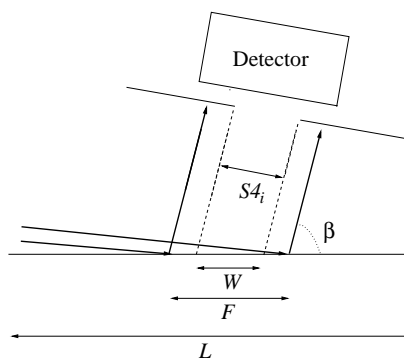


Figure 3.7: *Part of the x-rays are not visible by the detector*

A correction has to be made if $W < F$ which can occur if $\beta \gg \alpha$ and α small, as depicted in Fig. 3.7. The effective footprint of the beam on the sample is given by $(x_2 - x_1)$, with

$$x_1 = \max\left(\frac{L - F}{2}, \frac{L - W}{2}, H_1\right), \quad (3.7)$$

$$x_2 = \min\left(\frac{L + F}{2}, \frac{L + W}{2}, L - H_2\right). \quad (3.8)$$

The measured intensity I_0 needs to be corrected with the ratio of F to the effective footprint

$$I = I_0 \frac{F}{(x_2 - x_1)}. \quad (3.9)$$

Data-points with negative values of $(x_2 - x_1)$, which can occur at very small α , when shadowing (see Fig. 3.6) prevents the beam to reach the sample at all, are omitted.

In addition to the above corrections, transverse and radial scans are multiplied with the factor $(\sin \alpha / \sin \theta)$ to account for the change of the illuminated area as a function of α when $\alpha \neq \beta$. Without this correction the transverse scans are asymmetric, as can be seen in Fig. 3.8. All transverse scans are background subtracted, where the background was calculated from scans with no film present and/or from data for which $\alpha \leq 0$ or $\beta \leq 0$. The models of radial scans have a constant background added.

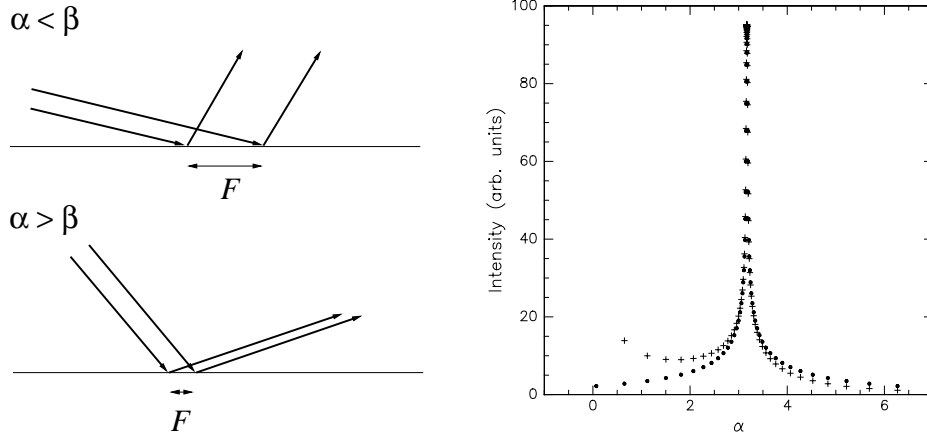


Figure 3.8: During a transverse scan the illuminated area changes (left); Transverse scan corrected for the change in illuminated area (dots) and the uncorrected scan (crosses) (right).

3.1.5 Resolution

(a) The in-plane divergence of incoming and outgoing wave vector

Calculation of the scattered intensity according to Eq. (2.38) requires a convolution with the resolution function $R(\mathbf{q})$. The relevant angles have been defined in Fig. 3.3. The momentum transfer \mathbf{q} can be decomposed as

$$q_z = k(\sin\beta + \sin\alpha) , \quad (3.10)$$

$$q_x = k(\cos\alpha - \cos\beta) . \quad (3.11)$$

Out of the scattering plane the resolution is poor due to the focusing of the monochromator and the widely set detector slits; thus the intensity is effectively integrated over this direction. Differentiating Eqs. (3.10) and (3.11) with respect to α and β leads to

$$\delta q_z = k(\cos\beta\delta\beta + \cos\alpha\delta\alpha) + \delta k_0(\sin\beta + \sin\alpha) , \quad (3.12)$$

$$\delta q_x = k(\sin\beta\delta\beta - \sin\alpha\delta\alpha) + \delta k_0(\cos\beta - \cos\alpha) , \quad (3.13)$$

where δk_0 is related to the wavelength by $\delta k_0 = -k_0\delta\lambda$. With the assumption that $\delta\alpha$ and $\delta\beta$ are randomly distributed and neglecting the wavelength dispersion, the

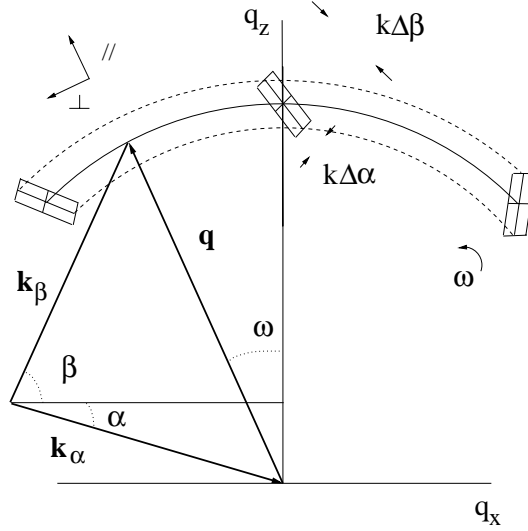


Figure 3.9: The resolution area is determined by $k\Delta\alpha$ and $k\Delta\beta$

resolution widths in q_x and q_z are given by

$$\Delta q_z = k[\cos^2\beta(\Delta\beta)^2 + \cos^2\alpha(\Delta\alpha)^2]^{1/2}, \quad (3.14)$$

$$\Delta q_x = k[\sin^2\beta(\Delta\beta)^2 + \sin^2\alpha(\Delta\alpha)^2]^{1/2}. \quad (3.15)$$

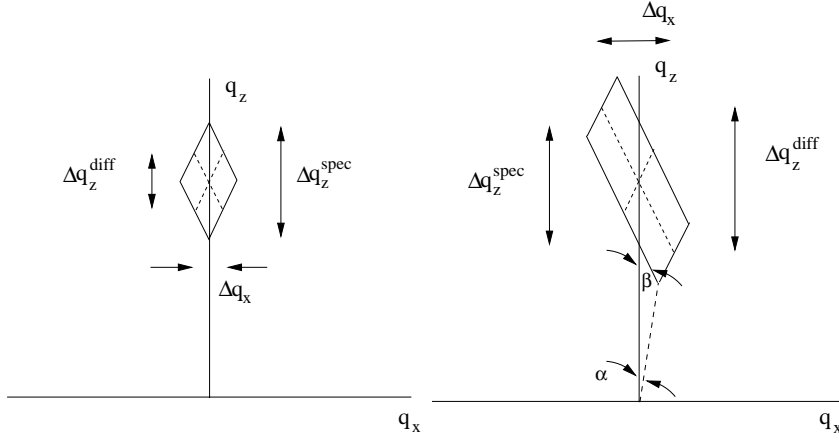
We have seen in Fig. 3.2 that the resolution widths or in-plane divergences $\Delta\alpha$ and $\Delta\beta$ can be approximated by Gaussians. This leads to a resolution area in the scattering plane determined by $k\Delta\alpha$ and $k\Delta\beta$, as shown in Fig. 3.9. For small angles the divergences can be approximated by [58]:

$$\Delta q_z = k[(\Delta\beta)^2 + (\Delta\alpha)^2]^{1/2}, \quad (3.16)$$

$$\Delta q_x = k[\beta^2(\Delta\beta)^2 + \alpha^2(\Delta\alpha)^2]^{1/2}, \quad (3.17)$$

$$= \frac{q}{2} \sqrt{\left(1 + \frac{\omega}{\theta}\right)^2 (\Delta\alpha)^2 + \left(1 - \frac{\omega}{\theta}\right)^2 (\Delta\beta)^2}, \quad (3.18)$$

In order to measure specular reflectivity the detector slits are usually set much wider than the pre-sample slits, so that $\Delta\beta \gg \Delta\alpha$ [45, 58]. However, for diffuse reflectivity measurements it is often advantageous to work with a symmetric resolution (see chapter 5). Figure. 3.10 shows the resolution area along q_z for both the situations $\Delta\beta \gg \Delta\alpha$ and $\Delta\beta = \Delta\alpha$. For a specular scan strictly confined to the q_z -axis the resolution Δq_z is given by the length along q_z enclosed by the resolution area, so that $\Delta q_z^{\text{spec}} = 2k\Delta\alpha$. The resolution Δq_x and Δq_z^{diff} of a diffusely

Figure 3.10: The resolution area for (a) $\Delta\beta \geq \Delta\alpha$ and (b) $\Delta\beta = \Delta\alpha$.Table 3.2: The resolution along q_z and q_x

		$\Delta\beta \gg \Delta\alpha$	$\Delta\beta = \Delta\alpha$
Δq_z^{spec}		$2k\Delta\alpha$	$2k\Delta\alpha$
Δq_z^{diff}		$k\Delta\beta$	$\sqrt{2}k\Delta\alpha$
Δq_x^{diff}	$\omega \approx 0$	$q\Delta\beta/2$	$q\Delta\alpha/\sqrt{2}$
	$\omega/\theta \approx 1$	$q\Delta\alpha$	$q\Delta\alpha$
	$\omega/\theta \approx -1$	$q\Delta\beta$	$q\Delta\alpha$

reflected signal are determined by the projection of the resolution area on the q_z axis. The results for both the situations $\Delta\beta \gg \Delta\alpha$ and $\Delta\beta = \Delta\alpha$ are given in Table 3.2.

(b) *The resolution function*

From this point on, $\Delta\alpha$ and $\Delta\beta$ will be expressed as Gaussian half widths, a factor $2\sqrt{2\ln 2}$ smaller than the corresponding FWHM in sec. 3.1.2. The resolution as a function of α and β is given by:

$$R(\delta\alpha, \delta\beta) = \exp\left(\frac{-\delta\alpha^2}{\Delta\alpha^2}\right) \exp\left(\frac{-\delta\beta^2}{\Delta\beta^2}\right), \quad (3.19)$$

This expression is separable in α and β because α and β are statistically independent, even though the distributions $k\Delta\alpha$ and $k\Delta\beta$ are in general not orthogonal. In order to express the resolution function as a function of q_z and q_x , for small angles Eq. (3.12) and (3.13) can be rewritten as

$$\delta\alpha = \frac{\delta q_z \beta + \delta q_x}{k(\alpha + \beta)} = \frac{\delta q_z \beta + \delta q_x}{q_z}, \quad (3.20)$$

$$\delta\beta = \frac{\delta q_z \alpha - \delta q_x}{k(\alpha + \beta)} = \frac{\delta q_z \alpha - \delta q_x}{q_z}. \quad (3.21)$$

This leads to the following expression, which is in general not separable in q_x and q_z [61]

$$R(\delta q_x, \delta q_z) = \exp\left(\frac{(\delta q_z)^2(\alpha^2 \Delta\alpha^2 + \beta^2 \Delta\beta^2) + (\delta q_x)^2(\Delta\alpha^2 + \Delta\beta^2) + 2\delta q_z \delta q_x(\beta \Delta\beta^2 - \alpha \Delta\alpha^2)}{(-q_z \Delta\alpha \Delta\beta)^2}\right). \quad (3.22)$$

In the case $\Delta\alpha = \Delta\beta$, Eq. (3.23) simplifies to

$$R(\delta q_x, \delta q_z) = \exp\left(\frac{-(\delta q_z)^2(\alpha^2 + \beta^2)}{2(\Delta q_z)^2 \alpha^2}\right) \exp\left(-\frac{(\delta q_x)^2(\alpha^2 + \beta^2)}{2(\Delta q_x)^2 \alpha^2}\right) \\ \times \exp\left(\frac{-\delta q_z \delta q_x \sqrt{\alpha^2 + \beta^2}(\beta - \alpha)}{\sqrt{2} \alpha^2 \Delta q_z \Delta q_x}\right). \quad (3.23)$$

The cross-term containing $\delta q_x \delta q_z$, which is proportional to $(\beta - \alpha)$, causes a tilt of the resolution area in a scan across ω , as can be seen in Fig. 3.9, and prevents separation of the resolution function into terms containing only δq_x or δq_z . Similarly, a cross-term proportional to $(\Delta\beta - \Delta\alpha)$ arises if $\alpha = \beta$ with $\Delta\alpha \neq \Delta\beta$. The cross-terms only disappear for $\alpha = \beta$, *i.e.* for specular reflectivity *and* a symmetric resolution $\Delta\alpha = \Delta\beta$. This coupling term implies that a two-dimensional convolution is required to compare the experimental data with the calculated structure factor. However, the use of a symmetric resolution and a simple trick can simplify this problem. The cross-term disappears if the resolution function is expressed as a function of q_{\parallel} and q_{\perp} , the components parallel and perpendicular to \mathbf{q} , respectively. Fig. 3.9 shows that both \mathbf{q} and the resolution area rotate with ω ; neither Δq_{\parallel} nor Δq_{\perp} varies as a function of ω . Therefore, we get for all α and β

$$R(\delta q_{\parallel}, \delta q_{\perp}) = R(\delta q_z, \delta q_x)|_{\alpha=\beta}. \quad (3.24)$$

Using the Gaussian resolution half widths perpendicular and parallel to \mathbf{q} :

$$\Delta q_{\parallel} = \sqrt{2} k \Delta\alpha, \quad (3.25)$$

$$\Delta q_{\perp} = (q_z/2k)\Delta q_{\parallel} \quad (3.26)$$

and $q_z = 2k\alpha$, we can write for Eq. (3.24)

$$R(\delta q_{\parallel}, \delta q_{\perp}) = \exp\left(-\frac{\delta q_{\parallel}^2}{\Delta q_{\parallel}^2}\right) \exp\left(-\frac{\delta q_{\perp}^2}{\Delta q_{\perp}^2}\right). \quad (3.27)$$

At small angles $q_{\parallel} \approx q_z \approx |\mathbf{q}|$ and $q_{\perp} \approx q_x$, however, Δq_{\parallel} and Δq_{\perp} differ from Δq_z and Δq_x , respectively. In conclusion, the use of a symmetric resolution, $\Delta\alpha \approx \Delta\beta$, allows the separation of the resolution function into components parallel and perpendicular to the wave vector transfer, so that a complicated two dimensional resolution convolution is not necessary in the analysis of the data. The resolution function thus obtained is applicable in the analysis of diffuse radial scans and diffuse transverse scans, as described in section 3.1.3, and will be used to obtain an expression for the scattered intensity without artificial separation of the specular and diffuse component in chapter 5 and 6.

3.2 The (2+2) diffractometer

3.2.1 The (2+2) surface scattering setup

The so called (2+2) surface scattering setup [62], as pictured in fig. 3.11, owes its name to the two independent degrees of freedom for the detector and for the sample. The surface normal of the sample is defined to be in the z direction. The detector angles are γ and δ , with the γ axis collinear with the x axis. The δ circle is mounted on the γ circle so that the δ axis passes through the origin perpendicular to the x axis. The detector, which is mounted on the δ circle is always facing the origin. The sample angles are χ and ψ , with the χ axis collinear with the x axis and the ψ axis perpendicular to the x axis.

The experiment described in chapter 6 is performed at the multi-technique goniometer for in-situ study of interfaces, at bending magnet beam-line BM32 (IF CRG) at the European Synchrotron Radiation Facility in Grenoble, France. This diffractometer is designed to allow diffraction and reflectivity, and can be operated both in horizontal and vertical geometries. We operated the diffractometer in the vertical geometry for optimum use of the in-plane resolution and polarization. Table 3.3 contains some of the characteristics of the source and optical elements of BM32 [63], while a sketch of the beam-line is displayed in Fig. 3.12. A motorized

Table 3.3: *The source characteristics of the bending magnet and the optical elements at BM32*

source size	0.3 × 0.3 mm ² H×V FWHM	
vertical source divergence	0.1 mrad at 20keV	
horizontal acceptance	1.5 mrad	
distance source-sample	56.2 m (<i>L1</i>)	
distance sample-detector	0.72 m (<i>L2</i>)	
optical elements	mirror	double crystal monochromator
distance from source	28 m (<i>L3</i>)	31 m (<i>L4</i>)
focusing type	vertical collimation	horizontal focusing
reflecting element	Ni/Pt coating	Si(111)
beam size at sample	0.30 × 3mm ² (H×V)	
spectral range	4-30 keV	
energy resolution $\Delta E/E$	$\approx 0.5 \times 10^{-4}$ Si(311)	$\approx 2 \times 10^{-4}$ Si(111)
expected flux at sample	10^{11} photon/s	

translation table can bring the sample to the centre of the goniometer, while two cradles allow further aligning of the sample in the beam. All turntables or translation tables have an accuracy of 1 m° or 1 μ m, respectively. The goniometer is operated by the program *SPEC*. In the experiment described in chapter 6 the pre-sample slits *S6*, at 150 mm from the sample, were set at 0.05 mm in the in-plane direction and 0.1 mm in the out-of-plane direction. The distance sample–detector *L2* was 720 mm, with detector slits *S8_i*, *S8_o* both set at 0.5 mm. The post-sample slits *S7*, at a sample-slit distance of 220 mm, were also set to these values. The in-plane divergence $\Delta\alpha_i$ is determined by the double crystal monochromator and the slits *S3_i* in front of the monochromator [64]

$$\Delta\alpha = \frac{S3_i \times L4/(L5)}{(L1 - L4)}, \quad (3.28)$$

where *L5* = 29 m is the distance from the source to slits *S3*. The in-plane divergence $\Delta\beta_i$ depends on the width of the detector slits *S8_i* and the distance *L2*, as given by Eq. 3.2. The out-of-plane divergence is mainly determined by the mirror. The widths of the main beam in the in-plane and out-of-plane directions, obtained

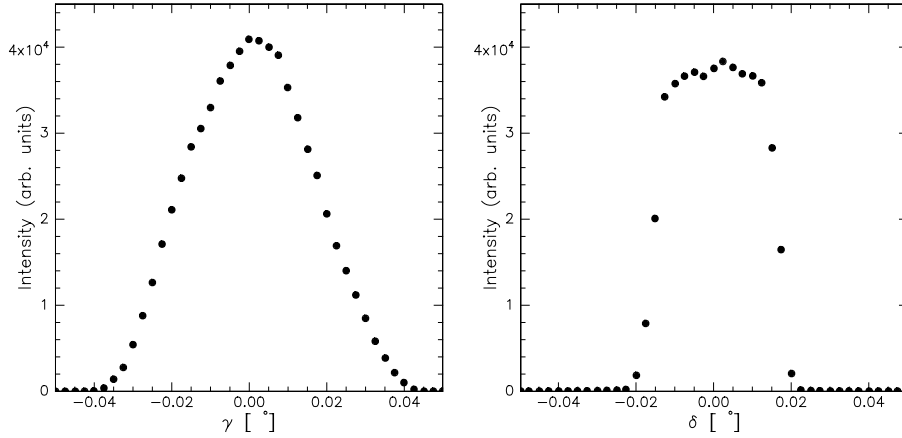


Figure 3.13: *The direct beam in the direction in-plane (left) and out-of-plane (right).*

by scanning γ and δ , respectively, are pictured in Fig. 3.13. The full widths of the main beam finally obtained are $\Delta\gamma = 0.044^\circ$ FWHM and $\Delta\delta = 0.036^\circ$ FWHM. All measurements were performed at $\lambda = 0.689 \text{ \AA}$, which corresponds to an energy of 18 keV. In the configuration used the incident beam intensity was 5×10^9 ct/s while the background was typically 0.4 ct/s. Thus, a dynamical range of ten orders of magnitude could be obtained.

3.2.2 Scan types

A schematic of the scattering geometry used in the experiment described in chapter 6 is shown in Fig. 3.14. Three types of scans were performed: specular longitudinal scans, diffuse longitudinal scans, and diffuse transverse scans, they are depicted in Fig. 3.14. In the case of specular scans the situation is the same as originally shown in Fig. 3.4 (top). Specular scans probe the scattered intensity along q_z with $q_y = 0$ and $q_x = 0$ in reciprocal space, by varying α and β with respect to the sample surface while $\alpha = \beta$. Thus $\chi = \gamma/2$ and $\sin \alpha = \sin \beta = \sin \chi$, at an out-of-plane detector angle $\delta = 0$. Transverse diffuse scans measure the scattered intensity along q_y at fixed q_z , while $q_x = 0$; by keeping $\alpha = \beta$ constant with respect to the surface and moving the detector out of plane over angle an δ , while rotating the sample over $\psi = \delta/2$. Finally, in longitudinal diffuse scans q_z

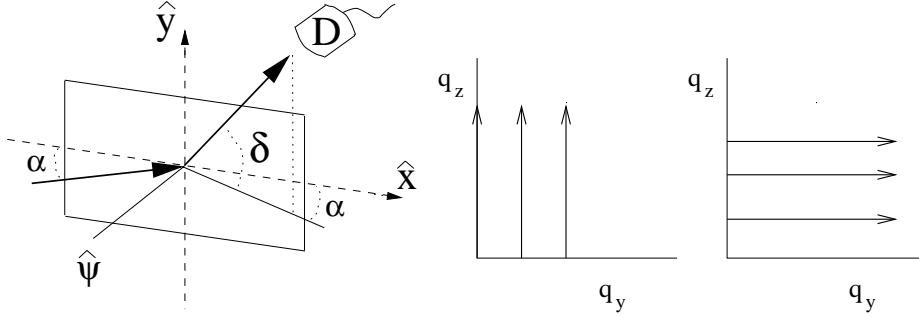


Figure 3.14: *The scattering geometry for the (2+2) setup and (left), and the various scans, with specular scans along q_z , longitudinal diffuse scans at an offset q_y parallel to the q_z axis (middle) and transverse diffuse scans at constant q_z parallel to the q_x axis (right).*

is varied at constant finite q_y and $q_x = 0$. In this case α and β are varied, while keeping them constant with respect to the surface, at a fixed angle $\psi = \delta/2$.

The calculation of the scattering angle 2θ is not straightforward in the (2+2) scattering geometry as the reflection plane is not fixed with respect to the laboratory coordinate system. We can write

$$\cos 2\theta = \cos \delta \cos^2 \alpha - \sin^2 \alpha, \quad (3.29)$$

with still $|\mathbf{q}| = 2k \sin \theta$ and $q_z = 2k \sin \alpha$. Note that in the (2+2) geometry transverse diffuse scans with large in-plane momentum transfer q_y are possible even at small q_z where the scattered intensity is high, contrary to the case of transverse 'rocking' scans using a two circle diffractometer (see sec. 3.1.3). It should also be noted that transverse scans can only be measured in the positive q_y direction, as the windows of the oven will block the beam in the other direction (see Fig. 3.18).

3.2.3 Corrections to the data

In the present scattering geometry the effective footprint can become smaller than F when the beam overfills the sample. This occurred in the specular and longitudinal diffuse scans in chapter 6 for typically $\alpha \approx 0.2^\circ$. Eqs. (3.4) and (3.5) from section 3.1.4 and the $(\sin \alpha / \sin \theta)$ correction do not apply in this situation. However, an extra area-dependent correction has to be taken into account for

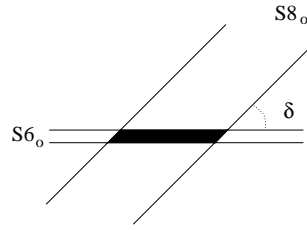


Figure 3.15: *The area visible by the detector depends on the out-of-plane detector angle δ , and the out-of-plane pre-sample ($S6_o$) and detector slits ($S8_o$).*

the out-of-plane measurements. Now the active surface area A of the sample, the illuminated area visible by the detector, depends on the out-of-plane angle δ and the slit widths $S6_o$ and $S8_o$, as shown in Fig. 3.15. When $\delta = 0$ we find $A = A_0 = S8_o \times F$, where F is still the footprint, while for finite angles δ

$$A = \frac{S6_o S8_o}{\sin \delta}. \quad (3.30)$$

For small δ , when $L_2 > F$, the parallelogram in Fig. 3.15 can 'walk' of the edges of A_0 and a more complicated correction is necessary. However, this correction is negligible as $S8_o > S6_o$ and $S8_o/F \ll 1$, so we approximate A by A_0 in these cases. The polarization factor for a bending-magnet beam-line polarised in the z -direction is given by [62, 65]

$$P = 1 - \sin^2 \alpha \cos^2 \delta. \quad (3.31)$$

For small α we find $P \approx 1$. Therefore we end up with following correction to the measured intensity I_0 :

$$I = I_0 \frac{A_0}{AP}. \quad (3.32)$$

All scans were background subtracted. The background was again calculated from scans with no film present.

3.2.4 Resolution

In sec. 3.1.5, the resolution was integrated over the y -direction, due to the widely set detector slits. For the out-of-plane scans in this section the calculation of the intensity involves a resolution deconvolution in the y direction, as well as in the x and z directions. For convenience it will again be assumed that all contributions

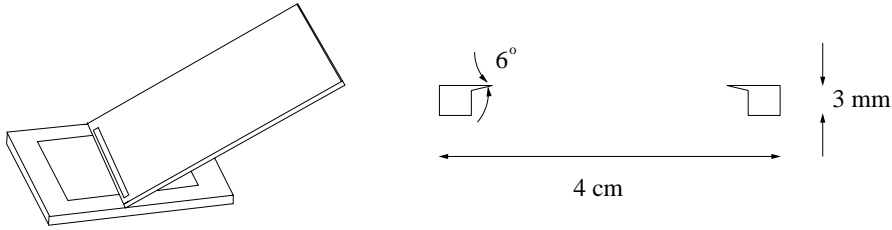


Figure 3.16: *The preparation of a freely suspended film by moving a spreader over the sample holder (left), and a schematic of the sample holder (right).*

to the resolution are Gaussian. The resolution for the specular reflectivity, strictly confined to the q_z -axis, is unchanged

$$\Delta q_z = 2k\Delta\alpha_i. \quad (3.33)$$

Here $\Delta\alpha_i$ is the in-plane incoming divergence of the beam. The out-of-plane transverse scans are basically specular scans 'on the side'. Therefore the expression will be similar, although now depending on the out-of-plane slits:

$$\Delta q_y = 2k\Delta\alpha_o. \quad (3.34)$$

The off-specular longitudinal scans, however, will depend both on the in-plane and the out-of-plane resolution. During a scan the resolution volume will tilt. Empirically was determined that

$$\Delta q_x = k \sin\psi \sqrt{(\Delta\beta_o)^2 + (\Delta\alpha_o)^2} / \sin\alpha \quad (3.35)$$

described the resolution well. However, this issue is still under investigation. In the analysis of the data in chapter 6 we will furthermore assume that the resolution function is separable in δq_x , δq_z and δq_y .

3.3 The sample and its environment

3.3.1 Sample preparation

The freely suspended films are drawn manually by moving a metal spreader with a narrow slit, filled with liquid crystal, over a hole in a holder, as shown in Fig. 3.16. By spreading the liquid crystal in the high temperature region of the SmA phase, films with thicknesses varying between two and hundreds of layers can be obtained.

Although the existence of one layer films was shown in the past [21, 23, 24], we never succeeded in making them. The thickness of the films is influenced by temperature and drawing speed; thin films could be prepared at high drawing speed and at a relatively high temperature. The best strategy to obtain thick films ($N > 100$) is to move the spreader repeatedly over an already existent film spanned over the hole. Directly after preparation a film consists of regions of different thicknesses, from which it is allowed to equilibrate to a uniform thickness at a temperature well below the SmA-N or SmA-isotropic transition temperature. Usually the thinnest region grows at the expense of the thicker regions [66]. The equilibration time varies from minutes to days; the more constant the drawing speed and working temperature, the shorter the equilibration time. We have also observed that the equilibration time shortens when the sample is kept vertically. During the experiments parts of the specular scan were taken regularly to check the uniformity of the thickness of the film. The films usually remained stable for weeks, although it was found that both very thin films ($N \leq 3$) and thick films ($N > 100$) were less stable, while the latter were also less uniform for the compounds investigated.

3.3.2 Sample holders

In the experiments described in the next chapters two designs for the sample holders were used. For the work presented in chapter 5 the films covered an area of $28 \times 10 \text{ mm}^2$ determined by four razor blade edges spot-welded onto the edges of a rectangular hole in a polished stainless steel plate. The films were hanging approximately $50 \mu\text{m}$ below the holder surface. Thus, the effect of shadowing (see section 3.1.4) had to be taken into account. In the later experiments (chapter 6 and 7) an improved holder design was used, where the holder flatness was more controllable and shadowing was nearly absent ($h \leq 10 \mu\text{m}$). This holder consists of a polished plate with a rectangular hole of $25 \times 10 \text{ mm}^2$ possessing sharp knife like edges, as pictured in Fig. 3.16. The holders were made of Al_2O_3 (99.7 % pure, Alsint) with the edges machined ultrasonically, or of hardened steel (Impax) with the edges spark cut. It was found that stainless steel was too soft to maintain a flat surface at the edges. Two types of ceramic were used, which were different in porosity and softness. The use of the more porous and soft ceramic resulted in holders with well defined edges. All holders were finally polished with $1 \mu\text{m}$ Diaplast.

Both types of ceramic holders were used in the experiments described in chapter 7, while hardened steel plates were used to obtain the results of chapter 6. Although a systematic investigation was not performed, films of all liquid crystals used in our research could be maintained on steel holders, while on the ceramic holders dewetting occurred for some liquid crystals¹. Special care has been taken in the cleaning of the ceramic holders as the liquid crystal material can easily penetrate the holder. A rigorous way to remove all material is to complete the cleaning process by heating the holder in vacuum at 400 °C.

The mosaic spread of the film, $\Delta\omega_{mos}$, is mainly due to non-flatness of the holder. For a proper analysis of the diffuse scattering signal, it is important that $\Delta\omega_{mos}$ is small compared to the experimental resolution, or at least that it can be considered constant over the range of the measurements. The $\Delta\omega_{mos}$ contribution to the resolution width in the perpendicular direction is given by

$$\Delta q_{\perp}^2(tot) = \Delta q_{\perp}^2(\Delta\alpha, \Delta\beta) + q^2\Delta\omega_{mos}^2, \quad (3.36)$$

while Δq_{\parallel} remains constant. The holder flatness was determined by performing transverse diffuse scans at various positions across the specular ridge, using a high resolution (Ge monochromator and analyser) setup. The mosaic spread of the holders with razor blades was found to be essentially constant as a function of incident angle, and thus beam footprint. For the smallest measured incident angle $\alpha = 0.4^{\circ}$, where the footprint was 11 mm² at a vertical slit-size of 0.5 mm, the film mosaic was nearly Gaussian with a width $\Delta\omega_{mos} = 0.035^{\circ}$ FWHM. The film mosaic increased Δq_{\perp} by less than 10% in the moderate resolution setup described. The mosaic spread of the second holder type was much narrower for all materials used. At a comparable vertical slit-size and a footprint of 20 mm a mosaic spread of 0.006° FWHM was found, which decreased to $\Delta\omega_{mos} = 0.002^{\circ}$ FWHM at a footprint of 2.6 mm², as shown in the rocking scan in Fig. 3.17.

3.3.3 Sample ovens and temperature control

Two types of sample ovens were used in the experiments described in this thesis. For the experiments described in the chapters 5 and 7 the oven design originally described in ref. [57] was used. The sample holder was mounted vertically in a

¹We also tried single crystal Si(111) holders, which are very smooth. Stable films could not be obtained on these holders with the compounds used. A systematic study of these holders with various liquid crystals was not done, however.

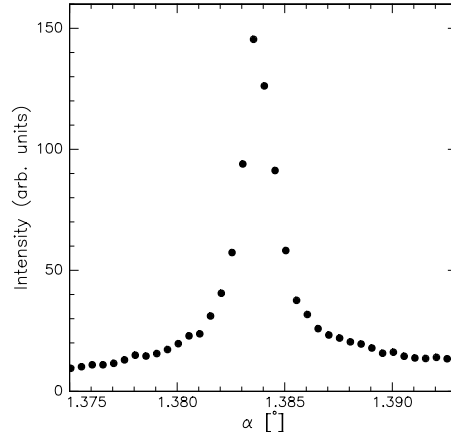


Figure 3.17: A transverse scan showing a film mosaic of 2 m° due to minor imperfections of the sample holder.

rectangular, copper sample cell with inner dimensions of $40 \times 24 \times 10\text{ mm}^3$. The cell has kapton windows allowing the incident and reflected x-ray beam to pass at angles between 0 and 12° . The film holder was centred at the middle of the cell by pressing the backplate below the holder against the cover of the cell with a screw. The sample cell was contained in a vacuum tight aluminum outer oven with mylar windows. The temperature of both cell and oven was measured with platinum resistors and controlled independently by heating resistors attached to the respective outer walls. Temperatures were regulated using Eurotherm PID controllers to within 0.1°C . In the experiments the temperature of the outer oven was $1\text{-}2^\circ\text{C}$ lower than the cell. During the measurements the oven was evacuated to reduce air scattering.

For the experiments described in chapter 6 a new oven design was used, which consisted of a cylindrical copper inner and outer oven. A side-view of the oven is pictured in Fig. 3.18. The sample holder is confined to its position in a rectangular frame in the sample cell by two screws. In order to perform out-of-plane measurements both ovens have kapton windows allowing the out-of-plane reflected x-ray beam to pass at angles between 0 and 70° , while in-plane angles between 0 and 10° can be reached. During the synchrotron experiments the oven was mounted as shown in the figure. The oven can be mounted on the base plate in two ways, so that testing and preliminary measurements could be performed on the rotat-

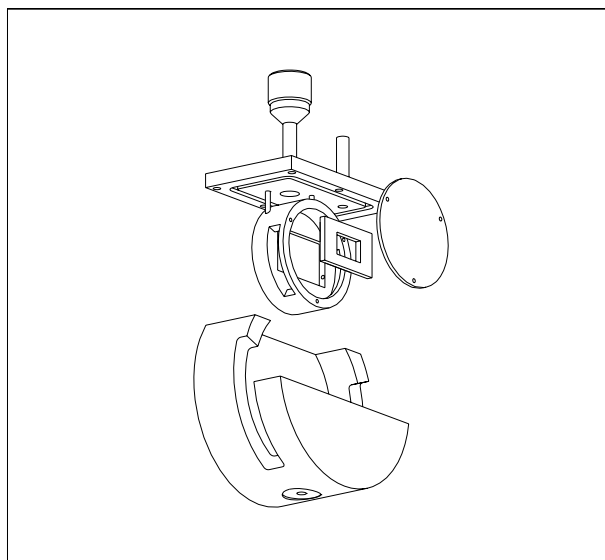


Figure 3.18: *View of the sample inner (top) and outer oven (bottom) used in chapter 6. The holder is shown as well.*

ing anode setup. The temperature control is as described above, although for this two-stage oven the temperature can be regulated to within 0.01°C . However, in the synchrotron experiment described in chapter 6 the temperature regulation was restricted to just the inner sample cell, giving a temperature control to within 0.1°C .

3.4 Appendix

Alignment of the two circle spectrometer in a moderate resolution setup

3.4.1 The spectrometer

In this section the alignment of the in house two circle spectrometer using a bent graphite monochromator is described. The alignment of a high resolution setup is extensively described in ref. [57]. During the alignment the generator is at minimum power $20 \times 10 \text{ kW}$ with sufficient absorbers. The proper monochromator

angle has to be selected and all parts of the spectrometer must be centred with respect to the beam. The alignment starts by placing the detector closely behind the monochromator. The use of Ni-foil blocks the K_β line, thus the monochromator can easily be rotated to the Bragg angle of the K_α doublet. Both $K_{\alpha 1}$ and $K_{\alpha 2}$ are present in the incident beam, giving a weighed wavelength of 1.542 Å. The monochromator can be translated in the x and z direction in its housing and two additional tilts in the xy and xz plane are present to focus the beam on the sample position. Next the goniometer arm carrying the post-monochromator flight-path is centred to allow passage of the x-ray beam. The pre-sample slits, followed by the post-monochromator slits are centred with the detector mounted on the column. Next the column with a needle in its centre is translated behind the flight-path, while the detector is positioned closely behind it. Now the rotation axis of the column can be centred with respect to the beam in an iterative process. A z translation scan will show a minimum in intensity at $z = z_0$ when the needle blocks the beam. This z -scan is repeated after rotating the sample table over 180° , giving a minimum at $z = z_{180}$. The needle will be in the centre of rotation if $z = (z_0 + z_{180})/2 = z_m$. So the column should be shifted until the minimum is at position z_m . Rotation of the sample table over 90° allows alignment in the x direction. At this stage of the alignment the monochromator can be tilted to increase intensity at the sample position and to obtain a round-spot shape at the sample position, using an x-ray eye. In addition the height of the beam can be determined by closing down the vertical slits to find the region of maximum intensity of the spot. Alternatively, the height of the beam can be adjusted to the desired height by placing a needle in the beam.

The detector arm must be positioned so that the beam can hit the detector. After placing the detector at its final position, the in-plane divergence $\Delta\alpha$ can be measured in a detector scan scanning the 2θ arm with very narrow detector slits compared to $S2_i$. The width of the detector slits is determined by the resolution required. Finally, the post-sample slits are set to reduce background scattering by closing them until they just touched the beam.

3.4.2 Alignment of the sample

Initially the sample oven is roughly aligned with respect to the beam by eye. The sample holder is first aligned in the direct beam by setting the detector angle to $2\theta = 0$ and translating the sample holder, using the z -table, so that the main beam

intensity is halved. By rotating the sample around its axis (ω -scan) the orientation of the sample face with the direct beam is varied. During this scan the edges of the sample cut the beam and the intensity measured by the detector should steadily decrease the less parallel the position of the sample is with respect to the beam. If the intensity increases to the main beam intensity during this scan, the sample is too far from the direct beam and should be translated further inwards. This iterative process of ω -scans and translation scans is performed until the sample is parallel with the beam and cuts half of its intensity.

The above procedure was used to determine the beam width at the sample position, using a Si wafer. Starting with $S2_i = 0.05$ mm a wafer of 12 mm diameter blocked the beam totally in an ω scan at $\pm 0.5^\circ$ so that $b1 = L \sin \alpha \approx 0.1$ mm was the beam-size at the sample position. After determining the beam size once, the above procedure can be used to align a sample. If the final ω -scan of the sample does not look triangular but has slopes, either the sample face is irregular or the sample is not properly vertically aligned. Then the sample cradle can be used to correct for this to within 0.5° .

Finally the sample is aligned on at least two positions in ' θ - 2θ ' (along q_z), determined by a rough specular scan, by performing ω -scans. Possible positions in θ - 2θ are the Bragg peak and a maximum of an interference fringe. Several of these alignment scans minimize the risk of 'falling of the specular ridge' during a scan. A missetting of the sample can easily be corrected by redefining the centre of the ω -scan as θ . For freely suspended films z translation scans must also be done as the film can be situated up to $50 \mu\text{m}$ below the sample holder. This also explains why it is impossible to align the sample below the critical angle, in the region of total reflectivity.

4

Elastic theory

*A continuous model is presented to calculate the displacement-displacement correlations in freely suspended films. The correlation function depends on the elastic constants of compression and bending of the layers, and on the surface tension. The model is equivalent to the original discrete model of Holyst [Phys. Rev. A **44**, 3692 (1991)], but computationally more efficient. Two characteristic in-plane lengths are introduced: R_l , above which the distance dependence of the correlation function follows a logarithmic law, and R_c above which the layers throughout the film fluctuate in unison, i.e. conformally.*

4.1 Introduction

For SmA systems the translational order between two layers is not truly long-range but decays algebraically with position. The fluctuations of the smectic layers are responsible for the absence of true long-range order; the mean square layer displacement diverges logarithmically with sample size (Landau-Peierls instability) [2]. Experimentally information about the fluctuations can be obtained using x-ray scattering. As shown in chapter 2 the diffuse scattering reduces in the limit of small q_z to the Fourier transform of the displacement-displacement correlation function, while the Gaussian attenuation along q_z contains information about the the mean square layer displacements.

The aim of this chapter is to present a model to calculate the displacement-displacement correlation function and the average layer fluctuation amplitudes for freely suspended films. We will first summarize the Landau-de Gennes free energy for bulk smectic systems [1] in sec. 4.2, which depends on the elastic constants for compression and bending of the layers. Recently theoretical models of thin free-standing smectic films have been developed [28, 29, 67–69] which include the effect of surface tension at the interfaces. The original formulation by Holyst [28] uses discretized fluctuations as a function of z . A later continuous version [67] has been shown to be equivalent. In section 4.3 we elaborate on the continuous version of the theory developed in [68], which is computationally most efficient. The influence of different values of the elastic constants and of the surface tension on the behaviour of the fluctuations is discussed in sec. 4.4. Central in this section are the length scales that determine whether the layers in the film fluctuate conformally, *i.e.* in unison. [48].

4.2 Bulk smectic-A systems

In the description of bulk SmA systems it is assumed that the sample is so large that effects from the boundaries, and thus the surface tension, can be neglected. As the layers are two-dimensional fluids the free energy should not depend on the in-plane components of the layer displacements, but only on the z -component, perpendicular to the layers. The layer displacement from the equilibrium position, $z = nd$, where n the layer index, is denoted as $u(\mathbf{r})$. The terms that may enter the free energy must be invariant to operations that leave the smectics unperturbed, such as a uniform translation of the layers. Thus, the free energy can only depend on derivatives of $u(\mathbf{r})$ and not on $u(\mathbf{r})$ itself. The free energy is also invariant with respect to in-plane rotations, which correspond to a mere rotation of the system where the orientation of the molecules with respect to the layers is unchanged. Thus, only second order derivatives parallel to the smectic planes, which describe a curvature of the planes, are allowed. Furthermore, stability requires the lowest terms in the free energy to be quadratic. Finally, the system is invariant to reflection with respect to the xy -plane; z and $-z$ are equivalent. These considerations lead to the following expression for the Landau-de Gennes free energy [1, 70]:

$$F_B = \frac{1}{2} \int d^3r \left[B \left[\frac{\partial u(\mathbf{r})}{\partial z} - \frac{1}{2} (\nabla u(\mathbf{r}))^2 \right]^2 + K [\Delta u(\mathbf{r})]^2 \right]. \quad (4.1)$$

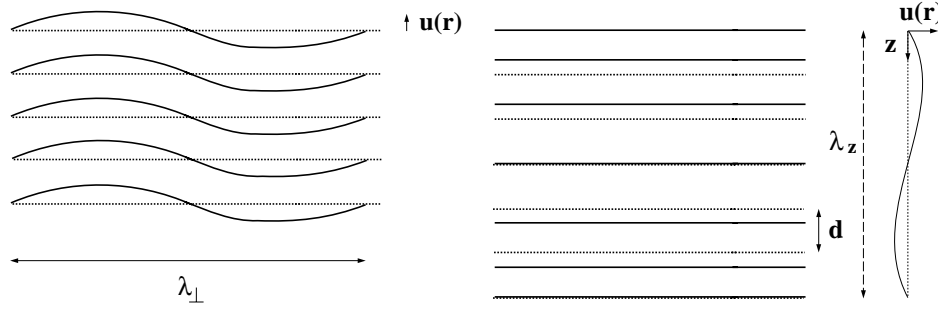


Figure 4.1: *The two basic fluctuation modes of the smectic layers where the dotted lines indicate the equilibrium positions of the layers, while the solid lines denote the actual layer positions; bending mode (left), and compressional mode (right).*

Here B and K are the elastic constants for compression and bending of the smectic layers, respectively, and the integration is carried out over the volume of the system. For typical experimental systems the anharmonic term, necessary to preserve the rotational invariance, can be neglected [28]. However, the final expression for the free energy would be of the same form when this term were taken into account, but B and K would be renormalized [71]. In the harmonic approximation $\text{grad } u$ is assumed to be small, which means that the layers are neither very much tilted from the x, y -plane nor strongly compressed [1, 28]. Thus, the second derivative of u with respect to z will be neglected to the first derivative. Therefore we can write

$$F_B = \frac{1}{2} \int d^3r \left[B \left[\frac{\partial u(\mathbf{r})}{\partial z} \right]^2 + K [\Delta_{\perp} u(\mathbf{r})]^2 \right], \quad (4.2)$$

where Δ_{\perp} is the Laplacian in x, y variables. In the following we shall write $\mathbf{q} = (q_x, q_y, q_z) \equiv (\mathbf{Q}, q_z)$, where $\mathbf{Q} = (q_x^2 + q_y^2)^{\frac{1}{2}}$. From Eq. (4.2) it is clear that bulk SmA systems have two long wavelength modes: the layer compressional modes parallel to z , which depend on B with wave vector $(0, 0, q_z)$, where $q_z = 2\pi/\lambda_z$ and the layer bending modes perpendicular to z , which depend on K with $\mathbf{q} = (Q, 0)$, where $Q = 2\pi/\lambda_{\perp}$. The bending and compression of the layers are illustrated in Fig. 4.1.

In order to calculate the average layer fluctuation amplitude, $\langle u^2(\mathbf{r}) \rangle$ the free energy in Eq. (4.2) has to be rewritten in terms of q_x, q_y and q_z . The displacement

$u(\mathbf{r})$ can be written as,

$$u(\mathbf{r}) = (2\pi)^{-3} \int d^3q u(\mathbf{q}) \exp(i\mathbf{q} \cdot \mathbf{r}). \quad (4.3)$$

Inserting the partial derivatives of Eq. (4.3) with respect to \mathbf{r} in Eq. (4.2) gives

$$F_B = \frac{1}{2}(2\pi)^{-6} \int d^3q \int d^3q' [-Bq_z q'_z + K\mathbf{Q}\mathbf{Q}'^2] u(\mathbf{q})u(\mathbf{q}') \int d^3r \exp[i(\mathbf{q} + \mathbf{q}') \cdot \mathbf{r}]. \quad (4.4)$$

Using

$$\delta(\mathbf{q} + \mathbf{q}') = (2\pi)^{-3} \int d^3r \exp[i(\mathbf{q} + \mathbf{q}') \cdot \mathbf{r}]. \quad (4.5)$$

and $u(-\mathbf{q}) = u(\mathbf{q}^*)$, where the asterisk denotes the complex conjugate, the free energy becomes

$$F_B = \frac{1}{2(2\pi)^3} \int d^3q [Bq_z^2 + KQ^4] |u(\mathbf{q})|^2. \quad (4.6)$$

The free energy can be written as a sum of contributions $F'_B(\mathbf{q})$ for each wave vector \mathbf{q} , because $\langle u(\mathbf{q})u(\mathbf{q}') \rangle = 0$, if $\mathbf{q} \neq -\mathbf{q}'$, so that

$$F_B = \frac{1}{(2\pi)^3} \int d^3q F'_B(\mathbf{q}), \quad (4.7)$$

with

$$F'_B(\mathbf{q}) = \frac{1}{2} [Bq_z^2 + KQ^4] |u(\mathbf{q})|^2. \quad (4.8)$$

According to the equipartition theorem each normal mode, *i.e.* each independent quadratic term, in the free energy has on average $\frac{1}{2}k_B T$ of energy and therefore

$$\frac{1}{2}k_B T = \frac{1}{2} [Bq_z^2 + KQ^4] \langle |u(\mathbf{q})|^2 \rangle. \quad (4.9)$$

Thus

$$\langle |u(\mathbf{q})|^2 \rangle = \frac{k_B T}{Bq_z^2 + KQ^4}. \quad (4.10)$$

Assuming that different modes of oscillation are uncorrelated and using Eqs. (4.3) and (4.9), the mean square fluctuations can be written as

$$\langle u(\mathbf{r})^2 \rangle = (2\pi)^{-3} \int d^3q \langle |u(\mathbf{q})|^2 \rangle = \frac{k_B T}{(2\pi)^3} \int \frac{d^3q}{Bq_z^2 + KQ^4}. \quad (4.11)$$

This integral can be evaluated using $d\mathbf{q} = 2\pi Q dQ dq_z$, while taking the range of integration into account. Wavelengths larger than the sample size L normal to

the layers and sample size W_x or W_y in the plane of the layers, are not possible. Similarly, modes with wavelengths shorter than the layer spacing or lateral molecular spacing a_0 are not allowed. We approximate $W_x = W_y = W$, so that the integration boundaries are $2\pi/W \leq Q \leq 2\pi/a_0$ and $2\pi/L \leq q_z \leq 2\pi/d$. In the case, $W \gg L$ and $a_0 < d$, the limits of integration can be expanded: $W \rightarrow \infty$ and $a_0 \rightarrow 0$. Consequently,

$$\begin{aligned} \langle u(\mathbf{r})^2 \rangle &= \frac{k_B T}{4\pi^2} \int \int dq_z dQ \frac{Q}{Bq_z^2 + KQ^4} \\ &= \frac{k_B T}{16\pi\sqrt{KB}} \ln\left(\frac{L}{d}\right). \end{aligned} \quad (4.12)$$

A similar expression can be derived for systems with infinite thickness and finite W [28]. Using the following values in Eq. (4.12): $B = 10^6$ N/m², $K = 10^{-11}$ N, $k_B T = 5 \times 10^{-21}$ Nm, $d = 30$ Å, we find $\sigma = \langle u^2(0, z) \rangle^{-1/2} = 11$ Å for a 1 m thick sample. Therefore, in all practical circumstances the layer displacement amplitude is significantly smaller than the layer spacing, consequently the smectic layers are still well defined.

In the thermodynamic limit the logarithmic divergence destroys long range order. However, even in this limit SmA systems possess quasi-long range order, because the translational order decays algebraically with position as $\mathbf{r}^{-\eta}$ [5, 72]. The exponent η is given by

$$\eta = \frac{q_m^2 k_B T}{8\pi\sqrt{KB}}, \quad (4.13)$$

where $q_m = 2\pi m/d$. Thus, over long distances the layers fluctuate in unison, resulting in a strong diffuse scattering from fluctuations of all length scales. This leads to singularities with algebraic decaying tails centred on the positions of the 'Bragg' peaks. These singularities have the form [5, 73]:

$$I(Q = 0, q_z) \sim (q_z - q_m)^{-2+\eta} \quad (4.14)$$

$$I(Q, q_z = q_m) \sim Q^{-4+2\eta}. \quad (4.15)$$

This behaviour has been observed in both thermotropic smectics [6] and in lyotropic lamellar phases [7]. There is a finite number of peaks according to Eq. (4.14); for large q_z where $\eta > 2$ one can find cusps in the intensity on the positions of the Bragg peaks instead of the divergences. Thus the maximum intensity of the quasi-Bragg peaks decreases rapidly with increasing m . In fact, in most thermotropic

smectics only the first Bragg peak is clearly present, which is expected to be at least partially related to the large value of η , and thus small B . It is important to note that *all* scattering in a bulk SmA phase is due to the fluctuations, to be contrasted with the Bragg peaks with diffuse tails found in three dimensional crystals. For finite size systems 'true' Bragg peaks appear on top of these singularities [73].

4.3 Freely suspended films

In order to calculate the displacement-displacement correlation function for freely suspended films we have to include the effect of the outer surfaces. The free-energy for a free standing smectic film can be written as the sum of the bulk contribution in Eq. (4.2) and of a surface contribution F_S [28]

$$F_S = \frac{1}{2}\gamma \int d^2r [[\nabla_{\perp} u(\mathbf{R}, z = L/2)]^2 + [\nabla_{\perp} u(\mathbf{R}, z = -L/2)]^2] . \quad (4.16)$$

The surface terms, which depend on the surface tension γ , describe the energy cost associated with an increase of the surface area of the two free surfaces located at $z = L/2$ and $z = -L/2$. For simplicity bulk elastic constants are used within the framework of the theory; therefore the values of B and K are independent of layer number and film thickness. Hence, the possible appearance of a higher smectic order parameter at the surface and thus a higher value of B , as described in chapter 1, will be neglected. Furthermore, we will not take the surface elastic constants for bending K_s [68] into account either. The introduction of K_s , which does not have to be related to K [67], would lead to a parameter $\gamma_{\text{eff}} = \gamma + Q^2 K_s$.

In this section we will extend the continuous version of the theory originally developed in Ref. [68]. The calculation of $\langle u^2(0, z) \rangle$ and of the layer displacement-displacement correlation function $C(R, z, z') = \langle u(\mathbf{R}, z)u(0, z') \rangle$ is central to the theoretical formalism. We define $\mathbf{r} = (\mathbf{R}, z)$ with \mathbf{R} in the plane of the film. The most convenient approach is to calculate $C(R, z, z')$ in the (\mathbf{Q}, z, z') -representation and subsequently take the inverse Fourier transform with respect to \mathbf{Q} . Substituting

$$u(\mathbf{Q}, z) = \int d\mathbf{R} \exp(-i\mathbf{Q} \cdot \mathbf{R}) u(\mathbf{R}, z) \quad (4.17)$$

in Eqs. (4.1) and (4.16) yields

$$F = \frac{1}{(2\pi)^2} \int d\mathbf{Q} F(\mathbf{Q}) , \quad (4.18)$$

where $F(\mathbf{Q})$ is the contribution of fluctuations with wave vector \mathbf{Q} given by

$$F(\mathbf{Q}) = \frac{1}{2} \int_{-L/2}^{L/2} dz [B|\partial_z u(\mathbf{Q}, z)|^2 + KQ^4|u(\mathbf{Q}, z)|^2] + \frac{1}{2} Q^2 \gamma [|u(\mathbf{Q}, z = L/2)|^2 + |u(\mathbf{Q}, z = -L/2)|^2] . \quad (4.19)$$

Partial integration of Eq. (4.19) allows rewriting of the free energy [68]. The obtained surface term vanishes if the fluctuation $u(\mathbf{Q}, z)$ satisfies the following boundary conditions

$$\gamma Q^2 u(\mathbf{Q}, \pm L/2) \pm B \partial_z u(\mathbf{Q}, \pm L/2) = 0 , \quad (4.20)$$

so that Eq. (4.19) transforms into a quadratic form

$$F(\mathbf{Q}) = \frac{1}{2} (u, \hat{A}u) = \frac{1}{2} \int_{-L/2}^{L/2} dz u^*(\mathbf{Q}, z) \hat{A}u(\mathbf{Q}, z) \quad (4.21)$$

with the operator

$$\hat{A} = (-B\partial_z^2 + KQ^4) . \quad (4.22)$$

It can be proven that the operator \hat{A} and its domain satisfy the following conditions [68]. Firstly, $\frac{1}{2}(u, \hat{A}u)$ coincides with $F(\mathbf{Q})$ for any arbitrary u from the domain. Secondly, \hat{A} is self-adjoint so that an arbitrary function can be expanded into its complete set of eigenfunctions $f_n(\mathbf{Q})$ (fluctuation modes) and eigenvalues $\lambda_n(\mathbf{Q})$. Third, all the eigenvalues are positive, which corresponds to the stability of the system. The use of boundary conditions does not impose restrictions on our consideration of the fluctuations; any given fluctuation can be approximated by a linear combination of eigenfunctions. Then, using the equipartition theorem, we can write

$$\langle u(\mathbf{Q}, z) u^*(\mathbf{Q}, z') \rangle = k_B T \sum \frac{1}{\lambda_n} f_n(\mathbf{Q}, z) f_n^*(\mathbf{Q}, z') . \quad (4.23)$$

This is the most conventional approach to calculate the correlation function, however, the analysis is not straightforward. Therefore we will continue with the approach developed in ref. [68], which is based on the expression

$$\langle u(\mathbf{Q}, z) u^*(\mathbf{Q}, z') \rangle = \frac{\int u(\mathbf{Q}, z) u^*(\mathbf{Q}, z') \exp(-F_Q/k_B T) Du}{\int \exp(-F_Q/k_B T) Du} , \quad (4.24)$$

where Du is the path integral over function u . All the integrals involved are well-defined if \hat{A} satisfies the requirements mentioned above. Equivalent to the case of

a variable ξ , where

$$\langle \xi^2 \rangle = \frac{\int d\xi \xi^2 \exp(-\frac{1}{2}\xi^2 a)}{\int d\xi \exp(-\frac{1}{2}\xi^2 a)} = a^{-1}, \quad (4.25)$$

we can write for the correlation function

$$\langle u(\mathbf{Q}, z) u^*(\mathbf{Q}, z') \rangle = k_B T \hat{A}^{-1}(z, z'), \quad (4.26)$$

where \hat{A}^{-1} is the inverse operator. Therefore,

$$\hat{A} \langle u(\mathbf{Q}, z) u^*(\mathbf{Q}, z') \rangle = k_B T \delta(z - z'), \quad (4.27)$$

so that in the case $z > z'$ or $z < z'$

$$\begin{aligned} \langle u(\mathbf{Q}, z) u^*(\mathbf{Q}, z') \rangle &= A_+(z') \exp(bz) + B_+(z') \exp(-bz) = u_+ \text{ if } z > z' \\ &A_-(z') \exp(bz) + B_-(z') \exp(-bz) = u_- \text{ if } z < z', \end{aligned} \quad (4.28)$$

where $b = Q^2 \sqrt{K/B}$. The boundary conditions in Eq. (4.20) yield

$$\begin{aligned} a [A_{\pm}(z') \exp(\pm bL/2) + B_{\pm}(z') \exp(\mp bL/2)] + \\ b [(A_{\pm}(z') \exp(\pm bL/2) - B_{\pm}(z') \exp(\mp bL/2))] = 0 \end{aligned} \quad (4.29)$$

with $a = \gamma Q^2/B$. Furthermore, the correlation function is continuous, so that

$$A_+(z') \exp(bz') + B_+(z') \exp(-bz') = A_-(z') \exp(bz') + B_-(z') \exp(-bz') \quad (4.30)$$

and finally,

$$\int_{z'-\epsilon}^{z'+\epsilon} dz \hat{A} \langle u(\mathbf{Q}, z) u^*(\mathbf{Q}, z') \rangle = \int_{z'-\epsilon}^{z'+\epsilon} dz k_B T \delta(z - z'), \quad (4.31)$$

thus,

$$\begin{aligned} -b [A_+(z') \exp(bz') + B_+(z') \exp(-bz')] + \\ b [A_-(z') \exp(bz') + B_-(z') \exp(-bz')] = k_B T. \end{aligned} \quad (4.32)$$

Using Eqs. (4.29), (4.30) and (4.31) one obtains

$$\begin{aligned} \langle u(\mathbf{Q}, z) u^*(\mathbf{Q}, z') \rangle &= \frac{k_B T}{2Bbh} \{ (b^2 - a^2) \cosh [b(z + z')] + [(b^2 + a^2) \cosh(bL)] \\ &+ 2ba \sinh(bL) \cosh [b(z - z')] - h \sinh(b|z - z'|) \}, \end{aligned} \quad (4.33)$$

with $h = (b^2 + a^2) \sinh(bL) + 2ba \cosh(bL)$.

After defining

$$\nu = \gamma/\sqrt{KB}, \quad (4.34)$$

$$\varrho = R/\sqrt{\lambda L}, \quad (4.35)$$

$$\text{and } \lambda = \sqrt{K/B}, \quad (4.36)$$

the Fourier transform finally gives the correlation function

$$\begin{aligned} C(R, z, z') &= \langle u(\mathbf{R}, z)u(0, z') \rangle \\ &= \frac{k_B T}{8\pi\sqrt{KB}} \int_{\xi_1}^{\xi_0} d\xi \frac{J_0(\sqrt{\xi}\varrho)}{\xi[(1+\nu)^2 - (1-\nu)^2 e^{-2\xi}]} f(\xi, z_+, z_-), \end{aligned} \quad (4.37)$$

where $\xi = L\lambda Q^2$, $\xi_0 = L\lambda(2\pi/a_0)^2$, $\xi_1 = L\lambda(2\pi/W)^2$, $z_+ = z + z'$ and $z_- = |z - z'|$ (with minimal value z_0). J_0 is the Bessel function of order zero, while the function f is given by

$$\begin{aligned} f(\xi, z_+, z_-) &= 2(1-\nu^2) \exp(-\xi) \cosh(\xi z_+/L) + (1+\nu)^2 \exp(-\xi z_-/L) \\ &\quad + (1-\nu)^2 \exp[-\xi(2-z_-/L)]. \end{aligned} \quad (4.38)$$

Instead of $C(R, z, z')$ we will use the full correlation function

$$g(R, z, z') = \langle [u(\mathbf{R}, z) - u(0, z')]^2 \rangle = \sigma^2(\mathbf{R}, z) + \sigma^2(0, z') - 2C(R, z, z'). \quad (4.39)$$

While each of the right hand terms diverges with increasing film size and, thus, requires an additional cutoff, this is not the case for $g(R, z, z')$. Therefore,

$$\begin{aligned} g(R, z, z') &= \frac{k_B T}{8\pi\sqrt{KB}} \int_0^{\xi_0} d\xi \frac{1}{\xi[(1+\nu)^2 - (1-\nu)^2 \exp(-2\xi)]} \\ &\quad \times \left[f(\xi, 2z, z_0) + f(\xi, 2z', z_0) - 2J_0(\varrho\sqrt{\xi}) f(\xi, z_+, z_-) \right]. \end{aligned} \quad (4.40)$$

Equation (4.40) is the expression for the correlation function used in the analysis of the experimental results. A cutoff chosen as $z_0 \simeq d/4$ reproduces essentially the results from the discrete model of Hołyst [28]. Such a cutoff is reasonable as the layers have a finite thickness and there is smearing of the layers due to the thermal motion of the molecules. Therefore, the z -coordinate of a single layer is not well defined. All calculations presented have been done with this choice of z_0 . The equivalence of the various models for calculating the displacement-displacement function is shown explicitly in Ref. [48].

As $z_0 > a_0$, the correlation function is not sensitive to the value of a_0 , because the integrand decays exponentially. This allows to expand the integration to infinity and, as a consequence, eliminates the second cutoff ξ_0 . Now the integration in Eq. (4.40) can be carried out analytically, using the following identities

$$\frac{1}{(1+\nu)^2 - (1-\nu)^2 \exp(-2\xi)} = \frac{1}{(1+\nu)^2} \sum_{n=0}^{\infty} \left(\frac{1-\nu}{1+\nu}\right)^{2n} e^{-2n\xi}$$

and [74]

$$\int_0^{\infty} dv \frac{1}{v} [e^{-\alpha v} - e^{-\beta v} J_0(\varrho\sqrt{v})] = A\left(\frac{\varrho^2}{4\beta}\right) + \ln\left(\frac{\beta}{\alpha}\right), \quad (4.41)$$

where $A(w) = \ln(w) + E_1(w) + c$. E_1 is the exponential integral function and c Euler's constant ($c = 0.5772\dots$). This leads to the following expression for the correlation function

$$\begin{aligned} g(R, z, z') = & \frac{k_B T}{8\pi\sqrt{KB}(1+\nu)^2} \sum_{n=0}^{\infty} \left(\frac{1-\nu}{1+\nu}\right)^{2n} \left\{ (1-\nu^2) \left[\ln\left(\frac{1+z_+/L+2n}{1+2z/L+2n}\right) + \right. \right. \\ & \ln\left(\frac{1+z_+/L+2n}{1+2z'/L+2n}\right) + \ln\left(\frac{1-z_+/L+2n}{1-2z/L+2n}\right) + \ln\left(\frac{1-z_+/L+2n}{1-2z'/L+2n}\right) \\ & + 2A\left(\frac{\varrho^2}{8n+4+4z_+/L}\right) + 2A\left(\frac{\varrho^2}{8n+4-4z_+/L}\right) \Big] \\ & + 2(1+\nu)^2 \left[\ln\left(\frac{z_-/L+2n}{z_0/L+2n}\right) + A\left(\frac{\varrho^2}{4z_-/L+8n}\right) \Big] \\ & \left. + 2(1-\nu)^2 \left[\ln\left(\frac{2-z_-/L+2n}{2-z_0/L+2n}\right) + A\left(\frac{\varrho^2}{8+8n-4z_-/L}\right) \right] \right\}. \quad (4.42) \end{aligned}$$

4.4 Influence of the elastic constants on the fluctuations

The displacement-displacement correlation function $C(R, z, z') = \langle u(\mathbf{R}, z)u(0, z') \rangle$ and the mean square layer displacements $\langle u^2(0, z) \rangle$ reveal information about the compressional modes, that depend on B , when $\mathbf{R} = 0$. By studying $C(R, z = z')$ information about undulations (and thus K) can be obtained. The fluctuation profile depends upon ν , as defined in Eq.(4.34); for $\nu > 1$ surface damping of the fluctuations is expected, while for $\nu < 1$ the fluctuation amplitudes will be enhanced at the surfaces. This is illustrated in Fig. 4.2 for various values of ν .

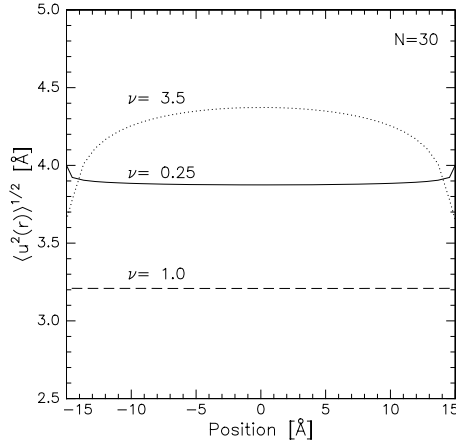


Figure 4.2: *The layer displacement fluctuation profile for a 30 layer film with $\gamma = 25 \times 10^{-3}$ N/m, $K = 10^{-11}$ N and $d = 29.4$ Å. Solid line: $\nu < 1$ ($B = 10^9$ N/m²); dotted line: $\nu > 1$ ($B = 5 \times 10^6$ N/m²); dashed line: $\nu = 1$ ($B = 6.3 \times 10^7$ N/m²).*

The fluctuations in the interior of the film are strongly influenced by \sqrt{BK} , so either a large B or K flatten the fluctuation profile. The surface fluctuations are strongly influenced by γ and depend hardly on L , unless γ is small [28, 48].

An important concept in this chapter, which was introduced originally in sec. 2.5, is conformality: at large separation R all the layers in a finite system fluctuate conformally, *i.e.* in unison, while the fluctuations are independent at shorter in-plane distances. Qualitatively the two regimes can be understood as follows: Figure 4.3 shows the effect of a small undulation at the surface of a bulk smectic liquid crystal. The distortion with in-plane wave number $Q = 2\pi/R$ decays slowly from one layer to the other, due to the small compressibility of the system in the z -direction. The characteristic decay-length of the distortion is given by $l(Q) = 1/(\lambda Q^2)$ [1]. Therefore, within this approximation a film is expected to fluctuate conformally for $R > R_c = 2\pi\sqrt{L\lambda}$, as determined by $l(Q_c) = L$. Although this argument explains, in principle, the two regimes and gives R_c for a thick film, it does not provide the proper value of R_c in a thin film, in which case the surface tension must be taken into account.

In the original analysis by Holyst [28] two regimes are obtained for the R -dependence of $C(R, z, z')$. At short distances R a strong dependence of $C(R, z, z')$

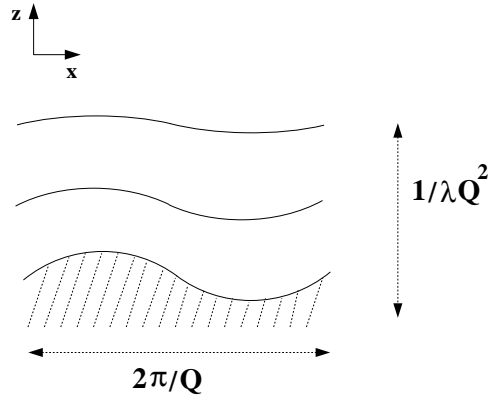


Figure 4.3: *Undulations at the surface of a smectic phase penetrate deep into the sample.*

on the layer position is found. At large separation all the layers fluctuate conformally and $C(R, z, z')$ decays logarithmically with increasing R . To find out how the surface tension affects R_c in a free-standing film we consider the first principal mode of the fluctuations, which gives the main contribution to the correlation function (see Eq. (4.23)). It corresponds to the smallest eigenvalue of the operator defined by Eq. (4.22). Solving

$$\hat{A}f(z) = \lambda f(z) \quad (4.43)$$

gives $f(z) = A \cos(n\kappa z) + C \sin(n\kappa z)$ where $\kappa = \frac{1}{B}[\lambda - KQ^4]$. The symmetry of the operator allows to treat odd and even eigenfunctions separately. It can be shown that the mode with the lowest eigenvalue is $\cos(\kappa z)$. Higher modes can be disregarded when the difference between the second and the first eigenvalue is larger than the first eigenvalue. As this difference is proportional to L^{-2} [68], the following consideration is valid only for thin films. The layers can be expected to fluctuate conformally if $\cos(\kappa z)$ does not change considerably across the film, *i.e.* if $\kappa L \ll 2\pi$. Using Eq. (4.20) κ is given by the minimal positive root of

$$\frac{\gamma Q^2}{B\kappa} = \tan(\kappa L/2) . \quad (4.44)$$

The boundary of the real-space range of conformality can be obtained by approximating $\tan(\kappa L/2) \approx \kappa L/2$ and $Q \approx 2\pi/R$. This yields

$$R \gg R_c \approx \sqrt{2\gamma L/B} . \quad (4.45)$$

If we take $L = 1830 \text{ \AA}$, $K = 10^{-11} \text{ N}$, $B = 2.5 \times 10^6 \text{ N/m}^2$ and $\gamma = 30 \times 10^{-3} \text{ N/m}$, Eq. (4.45) gives $R_c = 660 \text{ \AA}$, which is consistent with the numerical result for the same parameters used to obtain Fig. 1 of Ref. [28]. In the limiting cases of infinite B (a fully incompressible film) and zero B , R_c is equal to zero and infinity, respectively, as to be expected. The ratio $\varrho_c = R_c/\sqrt{L\lambda}$ is a function of ν and equals $\sqrt{2\nu}$ according to Eq. (4.45).

In the particular case of $\gamma = \sqrt{KB}$, and using $\varrho = R/\sqrt{L\lambda}$, Eq. (4.42) yields

$$g(R, z, z') = \frac{k_B T}{4\pi\gamma} \left[\ln \left(\frac{R^2}{4\lambda z_0} \right) + E_1 \left(\frac{R^2}{4\lambda z_-} \right) + c \right]. \quad (4.46)$$

The right-hand side of Eq. (4.46) does not depend on $z + z'$ and therefore the profile is completely flat (see also Ref. [68]). As a consequence information about the film thickness is lost; Eq. (4.46) does not contain L . It means that the smectic film can be described as if it were cut from a bulk smectic liquid crystal with a surface tension equal to \sqrt{KB} . The corresponding expression for a bulk SmA sample was derived for the first time by Caillé [5]. The two expressions coincide for $z_0 = d^2 e^{-c}/\lambda$. Equation (4.46) is also similar to an equation derived in Ref. [73] for an infinite sample, with the assumption $z_- \gg d$. A proper choice of z_0 makes them identical. Our choice of z_0 , as a cutoff parameter analogous to a_0 , is explained in sec. 4.3. The exponential decay of E_1 makes the second term in Eq. (4.46) negligible if the argument is larger than 1. For this range of R we find that $g(R, z, z')$ depends neither on z nor z' , but varies logarithmically with R . Since $z_- < L$, this range can be estimated as

$$R \ll R_l = 2\sqrt{L\lambda}, \quad (4.47)$$

still for $\nu = 1$. R_l is a second characteristic in-plane distance besides R_c .

In order to determine the range of R where $g(R, z, z')$ increases as $\ln(R)$ we return to Eq. (4.42), the full expression for the correlation function, for arbitrary values of ν . The logarithmic dependence can be written as $\partial_\varrho g(R, z, z') \sim R^{-1}$. Differentiating Eq. (4.42) and using

$$\frac{\partial A(c\varrho^2)}{\partial \varrho} = \frac{2}{\varrho} (1 - \exp(-c\varrho^2))$$

gives

$$\frac{\partial g(R, z, z')}{\partial \varrho} = \frac{k_B T}{2\pi\sqrt{KB}(1+\nu)^2} \frac{1}{\varrho} \left\{ \frac{(1+\nu)^2}{\nu} - \sum_{n=0}^{\infty} \left(\frac{1-\nu}{1+\nu} \right)^{2n} \right\} \times$$

$$\left[(1 - \nu^2) \exp\left(-\frac{\varrho^2}{8n + 4 + 4z_+/L}\right) + (1 - \nu^2) \exp\left(-\frac{\varrho^2}{8n + 4 - 4z_+/L}\right) + (1 + \nu)^2 \exp\left(-\frac{\varrho^2}{8n + 4z_-/L}\right) + (1 - \nu)^2 \exp\left(-\frac{\varrho^2}{8n + 8 - 4z_-/L}\right) \right] \}. \quad (4.48)$$

The derivative $\partial_\varrho g(R, z, z')$ is proportional to ϱ^{-1} is independent of z and z' if the result of the summation within the braces is much smaller than the preceding term. In that case Eq. (4.48) simplifies to

$$\frac{\partial g}{\partial \varrho} = \frac{k_B T}{2\pi\gamma\varrho}. \quad (4.49)$$

Integration leads to

$$g(R, z, z') = \frac{k_B T}{2\pi\gamma} \ln(\varrho) + D(z, z') = \frac{k_B T}{2\pi\gamma} \ln(R/\sqrt{L\lambda}) + D(z, z') \quad (4.50)$$

where the integration constant $D(z, z')$ is independent of R . As we shall see in the analysis of the experiments, the pre-factor defines the slope of a transverse diffuse scan in the appropriate region of R .

To determine the range of R where Eq. (4.50) applies, the summation in Eq. (4.48) must be carried out. Analytically this is not possible, but using a mild approximation, some answers can be obtained. In a narrow region around $\nu \approx 1$ the term with $n = 0$ gives the main contribution to the infinite sum. Taking only this term into account we arrive at the condition $\exp(-\varrho^2/4) \ll 1$ for the required range. It provides the same R_l as calculated from Eq. (4.46). If ν differs considerably from 1, the sum converges slowly and the main contribution comes from the tail of the sum. In this case terms in the denominators that are small compared to $8n$ can be neglected. Using in addition the approximation

$$\sum_{n=0}^{\infty} \exp(-an - b/n) \approx \int_0^{\infty} dx \exp(-ax - b/x), \quad \text{where } a = 2 \ln \left| \frac{1 + \nu}{1 - \nu} \right|, \quad b = \frac{\varrho^2}{8},$$

we can use [74]

$$\int_0^{\infty} dx \exp(-ax - b/x) = 2\sqrt{\frac{b}{a}} K_1(2\sqrt{ab})$$

so that the required condition for the logarithmic behaviour of $g(R, z, z')$ can be written as

$$\frac{2\varrho\nu}{(1 + \nu)^2 \sqrt{\ln|(1 + \nu)/(1 - \nu)|}} K_1\left(\varrho \sqrt{\ln \left| \frac{1 + \nu}{1 - \nu} \right|}\right) \ll 1. \quad (4.51)$$

Here K_n is a modified Bessel function of order n . This function contains an exponential decay as its argument gets larger, so that

$$R_l \approx \sqrt{\frac{L\lambda}{\ln|(1+\nu)/(1-\nu)|}}. \quad (4.52)$$

In the limiting case of $B \rightarrow \infty$ Eq. (4.52) evolves into

$$R_l \approx \sqrt{\frac{LK}{2\gamma}}, \quad (4.53)$$

while for $B \rightarrow 0$

$$R_l \rightarrow \sqrt{\frac{L\gamma}{2B}}. \quad (4.54)$$

An expression much simpler than Eq. (4.42) can be derived for incompressible freely suspended smectic films. Taking the limit $B \rightarrow \infty$ in Eq. (4.40) gives

$$g(R, z, z') = g(R) = \frac{k_B T}{2\pi\gamma} \int_0^{R_0 q_m} dv \frac{1 - J_0(Rv/R_0)}{v(1+v^2)}, \quad (4.55)$$

where $q_m = 2\pi/a_0$, $R_0 = \sqrt{LK/(2\gamma)}$, and $v = R_0 Q$. For a thin film of four layers with $d = 30 \text{ \AA}$, $K = 10^{-11} \text{ N}$, $\gamma = 30 \times 10^{-3} \text{ N/m}$, and $a_0 = 4 \text{ \AA}$ we find $R_0 q_m \approx 10$. Thus, keeping in mind that the integrand decays as v^{-3} , the upper limit can be replaced by infinity, except for the case of very thin films. With the expansion

$$\int_0^\infty dv \frac{1 - J_0(\varrho v)}{v(1+v^2)} = \int_0^\infty dv \left\{ \frac{v J_0(\varrho v)}{1+v^2} + \frac{\cos(\varrho v) - J_0(\varrho v)}{v} - \frac{1}{v} \left[\cos(\varrho v) - \frac{1}{1+\varrho^2 v^2} \right] + \frac{1}{v} \left[\frac{1}{1+v^2} - \frac{1}{1+\varrho^2 v^2} \right] \right\},$$

the integration can be carried out analytically. Using Ref. [74] to evaluate the first three terms we finally arrive at

$$g(\mathbf{R}) = \frac{k_B T}{2\pi\gamma} [\ln(R/R_0) + K_0(R/R_0) + c - \ln(2)], \quad (4.56)$$

It is easy to see that due to a fast decay of the Bessel function K_0 in this situation $R_c = 0$ and R_l coincides with R_0 . This is in agreement with Eq. (4.53) given above. Note that the pre-factor is the same as in Eq. (4.50). Figure 4.4 shows the dependence of $g(R, z, z')$ on R , calculated numerically on the basis of Eq. (4.40) and Eq. (4.56) for various values of B . The slopes for $R/R_0 > 1$ correspond to

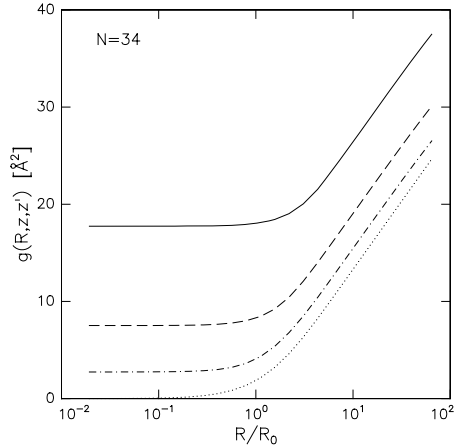


Figure 4.4: The full correlation function versus R/R_0 . R_0 is defined below Eq. (4.55); z and z' correspond to the top and bottom layers, respectively. The calculation is for a 34 layer film with $\gamma = 13 \times 10^{-3}$ N/m, $K = 10^{-11}$ N and $d = 29.4$ Å. The four curves, from top to bottom, correspond to B equal to 10^7 N/m², 10^8 N/m², 10^9 N/m² and ∞ , respectively.

the logarithmic law for the correlation function. The characteristic length R_l that limits this region starts at $R_l = R_0$ for infinite B and increases with decreasing values of B .

In summary we find that in general two characteristic in-plane lengths are needed to describe the fluctuations: R_l and R_c . For $R > R_l$ the correlation function has a logarithmic dependence on R and for $R > R_c$ the layers undulate conformally throughout the film. In the case of a thin film the surface tension strongly affects the fluctuations and $R_c = \sqrt{2\gamma L/B}$ (Eq. 4.45). If $\gamma \approx \sqrt{KB}$ we find $R_l \approx R_c \approx 2\sqrt{L\lambda}$. Eqs. (4.53) and (4.54) show how R_l depends on the physical parameters when the surface tension is much smaller and much larger than \sqrt{KB} , respectively. If B tends to infinity, R_c tends to zero, but R_l is finite. In the opposite range of B where $\nu \geq 1$, R_c and R_l are approximately equal. The pre-factor $k_B T/2\pi\gamma$ in the logarithmic region of the correlation function does not depend on the elastic parameters K and B , but is only affected by the surface tension. The continuous model described is, when a cutoff is taken into account, equivalent to the previous models of Holyst [69, 28, 67].

5

Conformal thermal fluctuations

The displacement-displacement correlations between thermal fluctuations of freely suspended Smectic-A films of a fluorinated liquid crystal have been determined using small angle specular and diffuse x-ray reflectivity. Data for 3 to 150 layer films are interpreted using the continuous theoretical model described in chapter 4. Values for the smectic bend and compression elastic constants as well as the surface tension are obtained from the wavelength dependence of the correlations. The obtained fluctuation profile depends only slightly on the film thickness and is nearly constant throughout the film. The fluctuations of all films investigated are conformal down to the smallest in-plane length scales measured. Furthermore, the collective long wavelength thermal fluctuations, which only depend on the diffuse scattering, can be separated from the local smectic disorder. The local contribution to the total fluctuation profile is found to be considerable.

5.1 Introduction

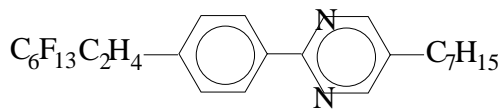
During the last decade freely suspended smectic films have been extensively studied using specular x-ray reflectivity [38, 39, 75]. Specular reflectivity probes

the laterally averaged density profile throughout the film. Recently the study of freely suspended films has been extended to diffuse x-ray scattering [48, 60], which probes the in-plane wave vector dependence of the long-wavelength thermal fluctuations. The combination of specular and diffuse scattering enables determination of the interlayer displacement-displacement correlation function, $C(R, z, z')$, without making assumptions about the local layer structure, as has usually been done up to now [39]. From $C(R, z, z')$ values for the surface tension and the elastic constants B and K of the smectic layers can be derived. The outcome of this investigation is presented in this chapter. Hitherto diffuse scattering has been used to gain insight into the lateral distribution of surface undulations of liquid [50, 76] and solid [31, 45–47, 49] surfaces, black soap films [77] and smectic liquid crystal polymer films on a substrate [78–80]. In the last case the layer fluctuations were dominated by the static undulations of the underlying substrate.

Once $C(R, z, z')$ is known from the diffuse scattering measurements, the local (uncorrelated) contribution of the smectic disorder to the total fluctuation profile can be obtained from the specular x-ray reflectivity, as described in chapter 2. The simplest possible slab model will be used to describe the electron density in a layer. The combination of specular *and* diffuse x-ray reflectivity measurements allows us to separate the extent of local smectic disorder and the magnitude of the long length scale thermal fluctuations. We find the local contribution to be non-negligible for the fluorinated compound investigated, contrary to the usual assumption.

At long in-plane length scales the thermal fluctuations are highly correlated as a result of the slow algebraic decay of the interlayer density-density correlation function. The layers fluctuate conformally, *i.e.* they undulate in unison. In this case the diffuse scattering will show maxima and minima at the same positions as the specular reflectivity. The shorter the in-plane length scale and the thicker the film, the more likely it is to lose this conformality, as discussed in chapter 4. The investigated films of the fluorinated compound used are conformal at the in-plane length scales that could be measured. The data for the thickest film (150 layers), however, indicate that conformality between top and bottom of the film might be lost.

In this chapter we first describe the sample preparation and the scattering configuration applied to measure the properties of interest. Section 5.3 contains the model used to calculate the scattered intensity and is followed by a section



Cryst. 72 SmC 79 SmA 123 I

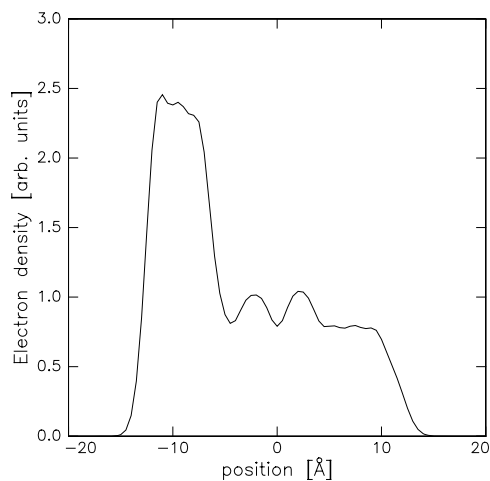


Figure 5.1: *The chemical structure of FPP with the bulk phase transition temperatures (top); and the calculated electron density of a single FPP molecule projected on the z-axis, where the electron density around each atom is assumed to be a Gaussian distribution of width $\sigma = 1 \text{ \AA}$ (bottom).*

discussing the effect of the various fitting parameters. Subsequently, in sec. 5.5 the experimental results are presented, followed by the discussion in sec. 5.6.

5.2 Experimental

5.2.1 Sample preparation

The compound investigated, 4-heptyl-2-[4-(2-perfluorhexylethyl)phenyl]-pyrimidin (FPP), is pictured in Fig. 5.1 where the phase sequence is also given. FPP was obtained from Merck (Darmstadt, Germany), and was used without further purification. FPP was chosen because the fluorinated tail causes the density variations along the molecule to be large and asymmetric, as shown in Fig. 5.1, producing strong Bragg peak scattering and in particular strong higher order peaks.

The films used in the experiment were hanging between four razor blades, as described in section 3.3.2. The films were drawn manually at 120–123 °C and allowed to equilibrate for several hours, until they reached their final thickness. During the equilibration period and the experiment films were kept at 88.0 ± 0.1 °C, well above the SmC-SmA phase transition. Measurements were performed on films of 3, 4, 6, 12, 20, 34 and 150 layers. The film thickness was constant during the experiment, as checked by scanning part of the specular reflectivity every day during the experiment. The thinnest film, however, remained only stable for a week, while the thickest film lost 9/10 of its thickness after approximately a week. A full set of measurements could not be completed for these two films.

5.2.2 Scattering configuration

Cu-K $_{\alpha}$ x-rays with $|\mathbf{k}| = 4.075 \text{ \AA}^{-1}$ were obtained from a Rigaku RU-300H generator operated at 18 kW maximum power. Measurements were made using the geometry shown in Fig. 3.3 in section 3.1.3. We worked with a symmetric resolution $\Delta\alpha = \Delta\beta = 0.044$. Thus, $\Delta q_{\parallel} = 1.9 \times 10^{-3} \text{ \AA}^{-1}$ and $\Delta q_{\perp} = 2.3 \times 10^{-4} q_z$. All slits were wide open vertically, while $S2_o$ was set at 3 mm, giving $\Delta q_y \simeq 0.1 \text{ \AA}^{-1}$. Therefore, the intensity is effectively integrated over this direction for the range of q_x values probed. The beam size on the sample was approximately $0.1 \times 3 \text{ mm}^2$ (H \times V). Further experimental details can be found in sec. 3.1. During the experiments we have used three types of scans, all in the scattering plane: specular, radial diffuse and transverse diffuse scans, as recapitulated in Fig. 5.2.

5.3 Intensity calculation

In agreement with the considerations in chapter 2 to 4 we find a model for the scattered intensity that includes both the diffuse and specular contributions. Following Refs. [28, 45], consistent with the first Born approximation but including refraction, the expression in Eq. (2.38) can be written as follows

$$\frac{I(\mathbf{q})}{I_0} = \left[|R_F|^2 \exp(-q_z'^2 \sigma_{loc}^2) \cdot \int dx \exp(-iq_x x) G(x, q_z') \right] * R(\delta q_{\perp}, \delta q_{\parallel}) \quad (5.1)$$

with

$$G(x, q_z') = \sum_{m,n}^N \exp[-iq_z'(m-n)d] \exp[-q_z'^2 g_{mn}(x)/2]. \quad (5.2)$$

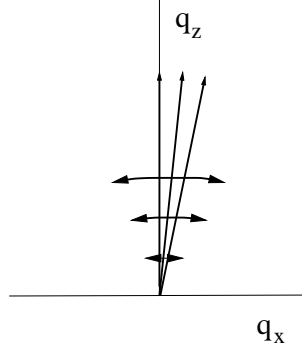


Figure 5.2: *The three types of scans: specular reflectivity scans, which probe the scattered intensity along q_z with $q_x = 0$, radial diffuse scans where both q_z and q_x are varied, and transverse diffuse (rocking) scans which for small angles probe essentially along q_x at fixed q_z .*

Here $g_{mn}(x) \equiv g(x, z_m, z_n)$, with $z_j = [j - \frac{1}{2}(N+1)]d$, is calculated using Eq. (4.40) in chapter 4 and the double sum runs over all N layers. The average z -component of the wave vector transfer in the film is given by Eq. (2.26). The term $|R_F|^2$ is the Fresnel reflectivity of a single layer calculated according to Eq. (2.19) [51], in which the smectic layer is approximated by the slab model of Fig. 5.3. It is smeared with a Gaussian of width σ_{loc} , which approximates the local (short wavelength) contribution to the total fluctuations. Using Eq. (3.27) the two-dimensional resolution convolution over $(\Delta q_{\parallel}, \Delta q_{\perp})$ is performed as a one-dimensional convolution along q_{\parallel} with half width Δq_{\parallel} , and a real space cutoff of $1/\Delta q_{\perp}$ to the structure factor integration along x . In this last case the convolution over $\delta \mathbf{q}_{\perp}$ is replaced by the Fourier transform in real space according to the Multiplication theorem [54]. The normalization Z to the integration can be calculated from the expression for the specular intensity for a smooth surface, when $g(x) = 0$ and $q_x = 0$, and where

$$Z \int_{-\infty}^{\infty} dx \exp(-x^2 \Delta q_{\perp}^2 / 2) = 1. \quad (5.3)$$

Hence, the normalization is $\Delta q_{\perp} / \sqrt{2\pi}$, which assures the proper q_z dependence for the diffuse component. The final expression for the scattered intensity is

$$\frac{I(\mathbf{q})}{I_0} = \left[|R_F|^2 \exp(-q_z'^2 \sigma_{loc}^2) \frac{\Delta q_{\perp}}{\sqrt{2\pi}} \int_{-\infty}^{\infty} dx \exp(-iq_x x) \exp[-\frac{1}{2}x^2 \Delta q_{\perp}^2] G(x, q_z') \right] \\ * \exp[-\frac{1}{2}q_{\parallel}^2 / \Delta q_{\parallel}^2]. \quad (5.4)$$

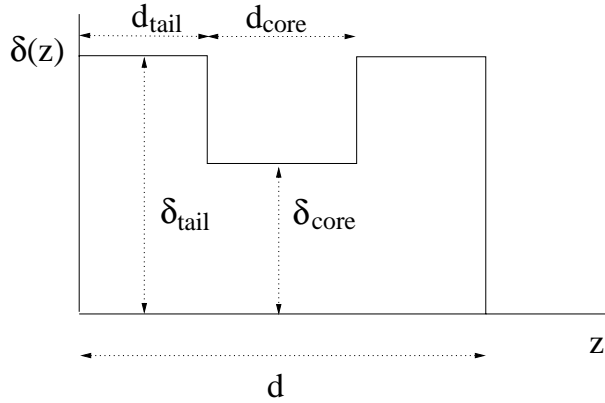


Figure 5.3: *The slab model for a single smectic layer.*

The cutoff to the integral in terms of the effective coherence length allows a calculation of $g_{mn}(x)$ without use of a resolution determining cutoff as in refs. [50, 81]. Note that the cutoff to the real-space integration in Eq. (5.4) is only possible with the separable resolution function obtained in section 3.1.5. It allows the extension the integration to infinity and leads to an expression for the intensity without an artificial separation of the specular and diffuse component.

5.4 Fitting parameters

In the fitting procedure we have three groups of significant model parameters: (N, d) , (γ, K, B) , and $(\sigma_{loc}, d_{tail}, \delta_{tail}/\delta_{core})$. All but the number of layers, N , are given a single value in the modelling of the data of all film thicknesses. To appreciate the experimental results it should be realized how they depend in a qualitative way on the various parameters. In the first group the total layer spacing d is fixed by the position of the Bragg peaks, while the number of layers follows from the repeat distance of the interference fringes.

The second group, (γ, K, B) , is related to the hydrodynamic fluctuations and is described in chapter 4. The roughness of the surfaces is determined by the surface tension and thus the overall falloff of the specular intensity along q_z , as well as with the lineshape of transverse diffuse scans at small q_x . Thus, at short in-plane distances we expect a simple power law behaviour $I(q_x) \sim 1/q_x^{1-\eta}$, with $\eta = k_B T q_m^2 / (4\pi\gamma)$, as found for simple liquids [50]. The combined effect of γ and the resolution width Δq_\perp determines the ratio of specular to diffuse intensity. The

bending elastic constant K is associated with the non-linearity of the transverse lineshape, when plotted on a log-log scale, at large q_x , even for $B \rightarrow \infty$. Thus, its effect is observable as a deviation from the power law behaviour at large q_x . For lateral length scales above R_c , as defined in sec. 4.4, capillary waves dominate the fluctuations, they were studied previously in light scattering experiments [82, 83]. Below the cutoff R_c the smectic fluctuations dominate. The compression elastic constant B is determined by the value of R_c and/or by the amplitude of the fluctuations. If in-plane distances are smaller than R_c conformality is lost, which will show up in the disappearance of interference fringes in radial diffuse scans as well as in the lineshapes of transverse diffuse scans across Bragg peaks compared to those at intermediate q_z positions.

The third group describes the molecular form factor and the local smectic (dis)order. The local density model used in the analysis makes no assumptions about the expected molecular density profile, but rather uses the most simple "slab" model (as shown in Fig. 5.3) which can describe the layer form factor. We assume up-down symmetry of the molecules in the smectic film and approximate a single smectic layer as consisting of regions of constant index of refraction, with a centre region of a given index of refraction $n_{core} = 1 - \delta_{core}$ and length d_{core} , and two identical tail regions of given index $n_{tail} = 1 - \delta_{tail}$ and length d_{tail} , so that $d_{core} = d - 2d_{tail}$. The layer averaged $\delta_{av} = (\delta_{tail}d_{tail} + \delta_{core}d_{core})/d$ determines the critical angle, as $q_c = 2k\sqrt{2\delta_{av}}$. However, shadowing effects of the film holder made it impossible to measure near q_c and thus a scaling factor was added to the calculated intensity. Two parameters strongly influence the fitting; $\delta_{tail}/\delta_{core}$, which determines the strength of the Bragg peaks, and d_{tail}/d , which affects the relative strength of the second to the first Bragg peak. These parameters show very little interdependence.

Finally, a Gaussian smearing of width σ_{loc} is included in the local layer profile. The various contributions to the fluctuations are assumed to be independent Gaussian random variables, related by $\sigma_{tot}^2 = \sigma_{loc}^2 + \sigma^2$. Here σ_{tot} is the specular falloff given by $\exp(-q_z^2\sigma_{tot}^2)$ and $\sigma = \sigma(0, z)$ is determined by the hydrodynamic fluctuations, as obtained from a fit to the transverse diffuse scans. A Gaussian smearing with width σ_{loc} leads to an overall falloff of the specular intensity, which is stronger the larger q_z , while another form of the local disorder might preferentially modulate the Bragg peaks. The consequences of our choice for the local molecular disorder are discussed in chapter 7.

5.5 Experimental results

Figure 5.4 shows specular (at $q_x = 0$) and radial diffuse scans (measured along $q_x = 2.62 \times 10^{-3}q_z$ and $q_x = 1.31 \times 10^{-2}q_z$) of 3, 4, 6, 12, 20 and 34 layers. For the 34 layer film a radial diffuse scan at $q_x = -1.31 \times 10^{-2}q_z$ was measured as well. It almost coincides almost with the scan at positive q_x , showing the equivalence of scans at $\pm q_x$. Note the similarity of the specular and diffuse radial scans, indicating conformality between the interfaces over the in-plane length scales measured. The 3 and 4 layer film lasted long enough to complete the two radial scans shown. The film of (150 ± 5) layers thinned after the completion of the set of transverse scans, during the diffuse radial scan displayed in Fig. 5.5. Before the thinning, the moderate resolution used was insufficient to resolve any interference fringes.

Transverse diffuse scans were done across the first and second Bragg peaks and across intermediate q_z positions at the maxima of interference fringes, as shown in Fig. 5.6. Note that all curves have been shifted. The similarity of the line shapes over almost the entire q_x range indicates conformality over the range of in-plane distances measured. Note the excellent agreement of the lineshapes at $\pm q_x$, as a result of the symmetric resolution. For $N = 34$ the figure contains a transverse scan across a minimum of an interference fringe as well. At a maximum of a fringe or Bragg peak the diffuse scattering is strongly peaked, implying long length scale displacement-displacement correlations across the interfaces. At the minimum of a fringe destructive interference of scattering from top and bottom of the film occurs. Thus, loss of conformality will show up at smaller q_x , *i.e.* the scan will turn flat earlier, as observed for the 34 layer film.

The positions of the Bragg peaks and the Kiessig fringes in the specular reflectivity curve fix d and N , respectively. We find $d = 29.40 \pm 0.04 \text{ \AA}$, independent of layer position and film thickness. With the obtained N and d , the transverse line shapes at fixed q_z were fit, for each film (the thickest film data excluded) separately, varying only γ , K , and B . Best fits for all films occur for values of $\gamma = (13.0 \pm 0.5) \times 10^{-3} \text{ N/m}$, $K = (1.0 \pm 0.5) \times 10^{-11} \text{ N}$, and $B = (7.5 \pm 2.5) \times 10^8 \text{ N/m}^2$. Fits using these values are given as the solid lines in Fig. 5.6. Fits to the specular scans (Fig. 5.4) were then performed with only the third group (σ_{loc} , d_{tail} , $\delta_{tail}/\delta_{core}$) as adjustable parameters, using the obtained values of γ , B , and K in Eq. (5.4). We find $\sigma_{loc} = 2.6 \text{ \AA}$, $d_{tail} = 0.19d$, and $\delta_{tail}/\delta_{core} = 1.14$. These values are essentially independent of both layer number and film thickness. Finally fits to the radial diffuse scans could be made using the above obtained set of pa-

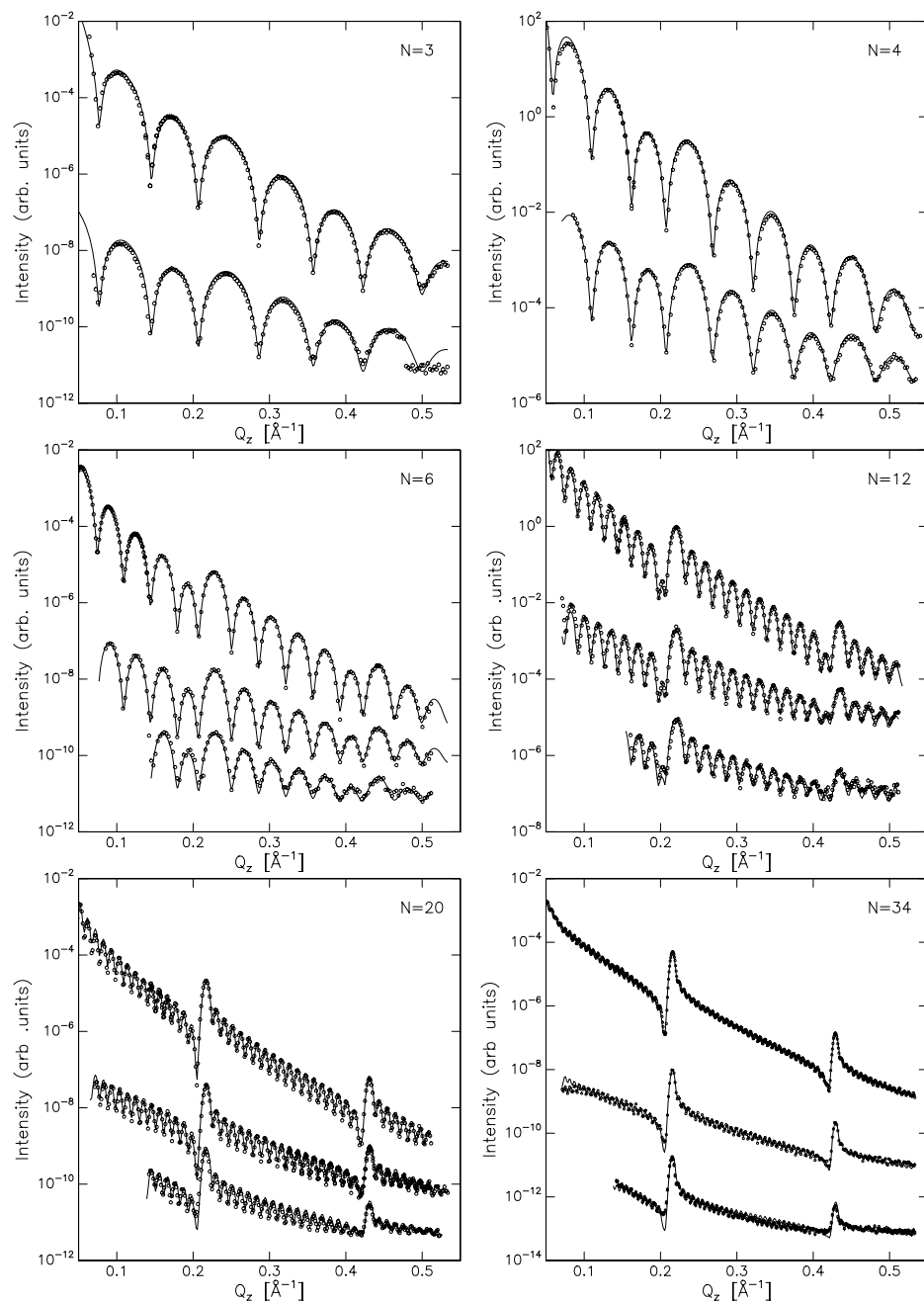


Figure 5.4: From top to bottom: Specular ($\omega = 0$), diffuse ($\omega = 0.15^\circ$ and $\omega = 0.75^\circ$) radial scans, with solid line fits as described in the text. Curves have been shifted for clarity and N is the number of layers.

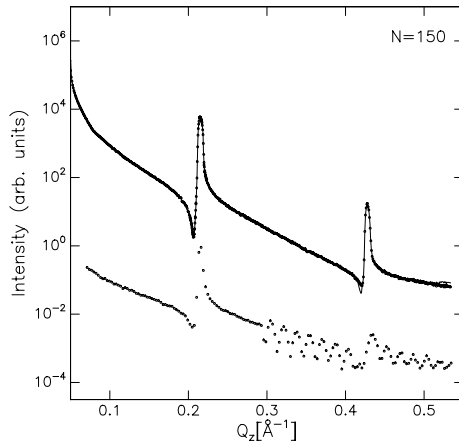


Figure 5.5: *Specular reflectivity curve of a (150 ± 5) layer film (upper curve) with the fit (solid line), and a radial diffuse scan at $\omega = 0.15^\circ$, during which the film thinned at 0.3 \AA^{-1} .*

rameters, without further adjustments. The moderate resolution was insufficient to resolve the Kiessig fringes of the thickest film, therefore the thickness was determined by modelling the specular reflectivity using the fit values obtained for the other films, while varying the number of layers. The fit obtained for $N = 150 \pm 5$ is shown in Fig. 5.5.

5.6 Discussion

Let us first discuss the results for the various parameters as obtained from the analysis. The value of $13 \times 10^{-3} \text{ N/m}$ obtained for the surface tension is smaller than the values reported for non-fluorinated liquid crystals, which lie in the range $(20 - 26) \times 10^{-3} \text{ N/m}$ [84, 85]. An independent conformation of our result by a direct measurement of the surface tension of FPP gave $(12.5 \pm 0.5) \times 10^{-3} \text{ N/m}$ [86]. Values in the same range were found for other fluorinated compounds. Apparently, fluorination of an alkyl chain of liquid crystals leads to a considerable reduction of the surface energy [24]. The value obtained for K is quite normal compared to other systems [2]. On the other hand, the value of B is about two orders of magnitude larger than values reported for other SmA systems [87, 88]. However,

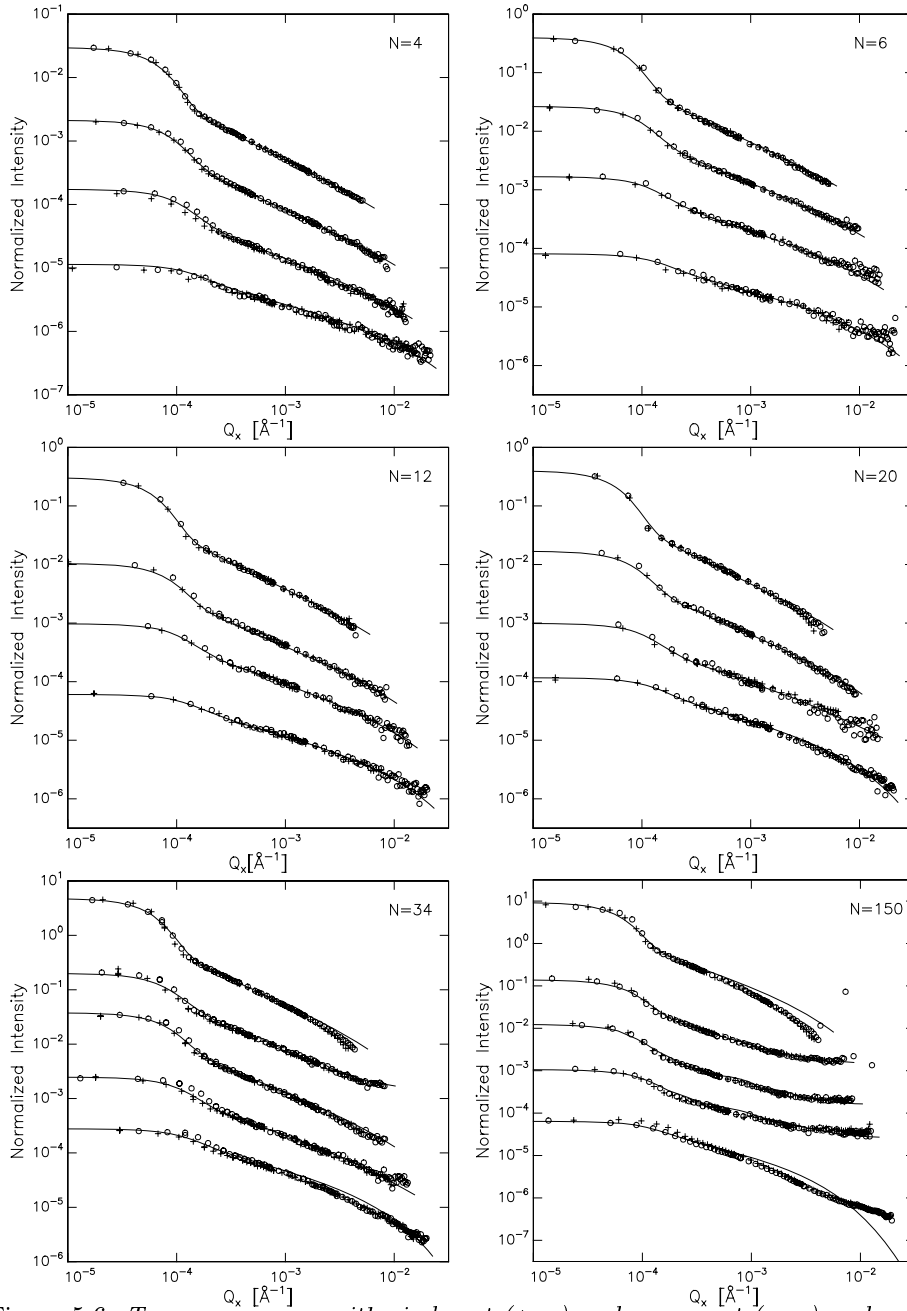


Figure 5.6: *Transverse scans with circles at $(+q_x)$ and crosses at $(-q_x)$ and solid line fits as discussed in the text. N is the number of layers. Top and bottom curves were measured at the Bragg peaks ($q_z \approx 0.22$ and 0.44 \AA^{-1}), respectively, and the middle curves at the maxima of interference fringes in between.*

most of these published data were taken close to a second order Smectic-A to Nematic phase transition, where $B \rightarrow 0$. This could easily explain an order of magnitude difference with our situation. Another order of magnitude might be a result of the fluorinated chain, which is bulkier and stiffer than a hydrogenated chain. In fact, the average cross-section of a fluorinated tail is approximately 30% larger than that of a hydrocarbon chain [89]. In addition, gauche-conformers can practically be excluded, leading to rigid rod-like fluorinated chains [90]. The resulting structural molecular model consists of a rigid aromatic core with a flexible hydrocarbon tail on one side and a rigid fluorinated tail on the other side.

Clearly our FPP system is nearly incompressible, with layers fluctuating in unison down the shortest in-plane wavelengths measured. Using Eq. (4.46) in sec. 4.4 this leads to $R_c \approx 20 \text{ \AA}$ for a 34 layer film, which is of the order of molecular dimensions. If the 150 layer film is approximated as a bulk system, Eq. (4.47) gives $R_c \approx 140 \text{ \AA}$, which is just within the experimental reach. Thus, loss of conformality of the fluctuations can only be expected for large in-plane q -values or even thicker films. The transverse diffuse intensity for the 4 layer film has a logarithmic dependence at all q_x values measured, in agreement with $\log_{10}(1/R_l) \approx -1.3 \text{ \AA}^{-1}$ as calculated using Eq. (4.53). For the 20 and 34 layer film $\log_{10}(1/R_l)$ is equal to -1.7 and -1.8 , respectively, just within the accessible q -range. Indeed, deviations from the logarithmic dependence can be seen in the bottom curves of the 20 and 34 layer film (at the second Bragg peak). The difference in slope between a transverse scan at a minimum and at a maximum confirms this behaviour. For the 150 layer film we find $\log_{10}(1/R_l) \approx -2.2 \text{ \AA}^{-1}$, in this case deviations from logarithmic behaviour are clearly visible in the figure.

Films of different thicknesses have different sensitivities to the various parameters. The larger logarithmic range of the transverse data for thin films results in a very accurate determination of γ . However, the data for the 4 and 6 layer film gives only a lower limit $B \geq (7.5 \pm 2.5) \times 10^8 \text{ N/m}^2$ and could equally well be fit using Eq. (4.56) derived for $B \rightarrow \infty$. Thicker films are necessary to determine the actual value of B . The effect of a variation of B is illustrated in Fig. 5.7 for the 34 layer film. It is clear that changing B by an order of magnitude can only lead to worse fits. The thicker the film becomes, the smaller the contribution of the surface tension to the fluctuations. Figure 5.8 displays a transverse scan at the first Bragg peak, $q_z = 0.215 \text{ \AA}^{-1}$, and at $q_z = 0.363 \text{ \AA}^{-1}$ for the 150 layer film. The solid line is from the film model used to fit the data and the dashed line in the

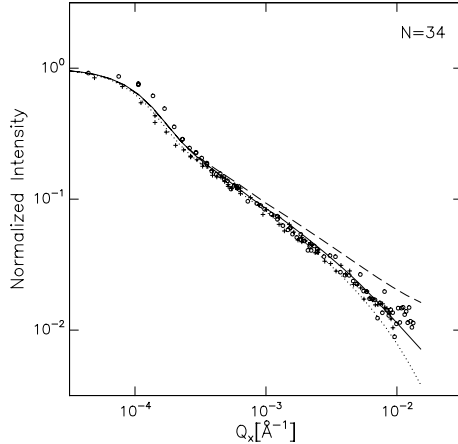


Figure 5.7: Calculation of the scattered intensity in a transverse diffuse scan for a 34 layer FPP film at $q_z = 0.358 \text{ \AA}^{-1}$, with $B = 10^8 \text{ N/m}^2$ (dashed line), $7.5 \times 10^8 \text{ N/m}^2$ (solid line) and $5 \times 10^9 \text{ N/m}^2$ (dotted line).

figure is calculated using Eq. (4.46) for a bulk liquid crystal. This figure indicates that even films of this thickness cannot be approximated by bulk systems yet. The relatively small surface tension of FPP leads to a stronger diffuse scattering than expected from the theory for bulk systems.

Finally we come to the third group of parameters containing all the molecular information. The value of $\sigma_{loc} = 2.6 \text{ \AA}$ for the local fluctuations, which is independent of the film thickness, can be compared with σ_{tot} . This last value can be obtained from a fit to the specular reflectivity calculated with a standard reflectivity program using dynamical methods [91], thus without taking the correlation function into account. The total fluctuation amplitude has contributions from both the thermal fluctuations and the local molecular disorder, as shown in Eq. (2.39). We find that σ_{tot} is almost independent of the film thickness, being 4.8 \AA for the 4 layer film and 4.5 \AA for the 34 layer film. Using $\sigma_{tot}^2 = \sigma^2 + \sigma_{loc}^2$ this gives values of $\sigma = 4.1 \text{ \AA}$ and $\sigma = 3.7 \text{ \AA}$, respectively, for the hydrodynamic part of the fluctuations in these extreme cases. Evidently the local fluctuations add a non-negligible contribution to the total fluctuation profile for FPP, and so the common belief that these can be neglected [28, 39, 69] is not generally valid. A measurement of the non-fluorinated analogue of FPP (see chapter 7) with a similar analysis resulted in $\sigma_{loc} = 0.8 \text{ \AA}$, indicating that the large value of σ_{loc} for

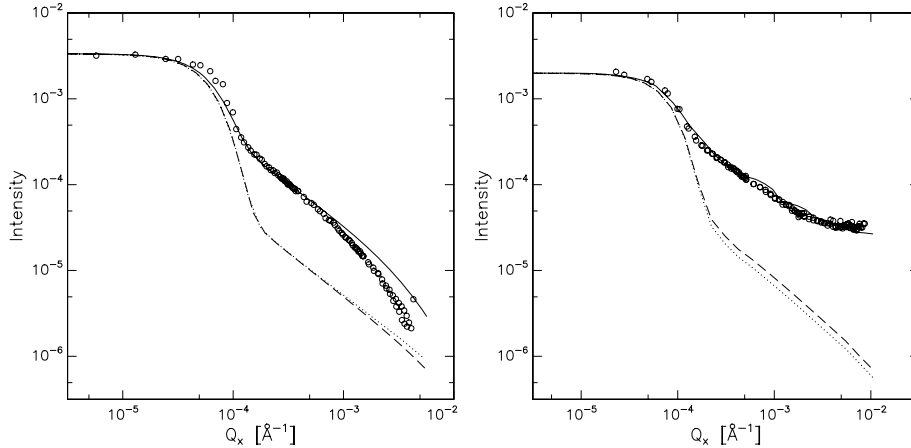


Figure 5.8: A comparison of the film model (solid line) with $B = 7.5 \times 10^8 \text{ N/m}^2$, $K = 1.0 \times 10^{-11} \text{ N}$ and $\gamma = 1.3 \times 10^{-2} \text{ N/m}$, and the bulk model (dashed line) with $B = 7.5 \times 10^8 \text{ N/m}^2$, $K = 1.0 \times 10^{-11} \text{ N}$ for a transverse scan at $q_z = 0.215 \text{ \AA}^{-1}$ (left) and $q_z = 0.363 \text{ \AA}^{-1}$ (right) for the 150 layer film. The dotted lines are calculated with $\gamma = \sqrt{KB}$.

FPP is not an artifact of the simple slab model used to describe the molecule.

Using the same parameters for every thickness film, the agreement between the model and the data for FPP is remarkable. It should be noted that the layer spacing used, $d = 29.4 \text{ \AA}$, was independent of the film thickness as well as of the position of the layer in the film. Allowing smaller d spacings for the surface layers [12], *i.e.* assuming tilted toplayers, for example as precursor of the SmC phase of FPP at lower temperatures, made the quality of the fits worse. This even applies to the thinnest films. Ellipsometric measurements indicate that such tilted toplayers are quite common up to about 2°C above the SmC-SmA phase transition [92]. In our case we are evidently outside this regime, as was recently confirmed by ellipsometric measurements [93]. Furthermore, the lower surface energy of the fluorinated groups could break the up-down symmetry at the surface. However, the data could not be modelled assuming polar ordering at the surface, in contrast to Ref. [24]. Such a polar ordering at the surface is rather unlikely, taking the large cross-section of the fluorinated tail compared to the alkyl chain into account. The molecular form factor of FPP will be discussed in detail in chapter 7.

Interestingly, the fits are of highest quality for the thinnest films where the continuum model is assumed to be less valid. However, the data exhibits deviations from the model for thick films at high q -values. This is most evident in the transverse line shapes at the Bragg positions of the 34 and 150 layer films (Fig. 5.6 top and bottom curves). In these cases varying B and K did not improve the fits. Off-Bragg-peak transverse diffuse scans of both films (Fig. 5.6 middle curves) agree much better with the model. As the Bragg positions are characterized by constructive interference of all the layers, the deviations could indicate that the mechanism of coupled fluctuations across smectic layers is more complicated than that incorporated in the model.

The values obtained for B and K result in $\lambda = \sqrt{K/B} = 1.2 \text{ \AA}$, an order of magnitude smaller than the layer spacing [28]. Thus, compression of the layers is hard compared to bending. Furthermore $\nu = 0.15$, and the profile of the hydrodynamic (collective) fluctuations along z is quite flat and nearly independent of N , as can be expected for a system with a high B and low γ [28]. However, as $\nu < 1$ an enhancement of the surface fluctuations as compared to the interior of the film should be anticipated. Figure 5.9 shows the fluctuation amplitude as a function of z , at large R where the correlation term is negligible, calculated using Eq. (4.37). Indeed, a slight enhancement of the surface fluctuations is observed.

The measurements of the displacement-displacement correlations presented here, shed new light on earlier results for freely suspended smectic films. Previous measurements [39] of the fluctuation profile using specular reflectivity could only test certain aspects of the Holyst theory, because the specular reflectivity is only sensitive to the laterally averaged electron density profile, and cannot distinguish between long-wavelength fluctuations and the local disorder. Also, the specular scattering is essentially unaffected by the correlations $\langle u(r)u(0) \rangle$, which in fact for the previous work were assumed to be zero. We stress that it is essential to use a combination of diffuse and specular scattering in order to obtain quantitatively reliable information on the total fluctuation profile.

5.7 Conclusions

We have quantitatively determined the correlations of the thermal fluctuations in freely suspended smectic-A films. This is accomplished by measuring, via the diffuse x-ray scattering, the in-plane wave vector dependence of the hydrodynamic

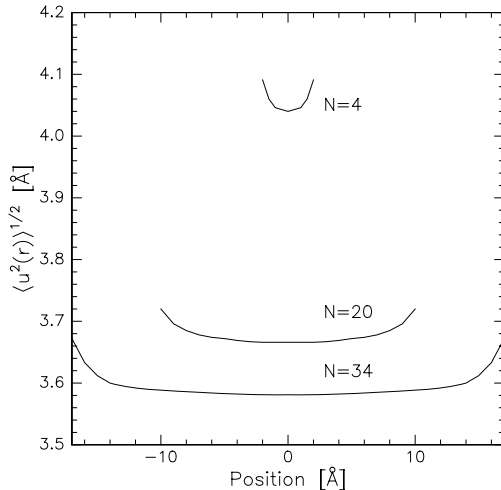


Figure 5.9: *The thermal fluctuation profile for a 4, 20 and 34 layer FPP film, respectively.*

(collective) fluctuations which are governed by the elastic parameters and the surface tension of the liquid crystal. This is to be contrasted with results reported so far which were restricted to specular scattering, which depends only weakly on the correlations in the fluctuations. The combination of diffuse and specular scattering measurements also enables separation of the contribution of the collective thermal fluctuations and of the local smectic disorder. In contrast to the usual assumptions we found the latter to be non-negligible.

All data (specular, radial diffuse and transverse diffuse scans) could be modelled using a single set of parameters. The films of the fluorinated compound we measured were conformal down to the smallest in-plane length scales probed, with the exception of the thickest of 150 layers which might indicate loss of conformality. We have shown that in order to analyse the data quantitatively, it is essential to use a symmetric separable resolution function, so that separation of the specular and diffuse contributions to the scattered intensity can be avoided. The separability of the resolution function allows a calculation of the correlation function without a resolution determining cutoff, as well as a simple normalization of the intensity.

6

Crossover from conformal to independent fluctuations

The thermal fluctuations in freely suspended smectic-A films have been studied for two film thicknesses using diffuse x-ray scattering. Using the appropriate scattering geometry the spectral dependence of the displacement-displacement correlation function could be measured down to molecular dimensions. At long lateral length scales the smectic layers were found to be conformal; i.e. top and bottom of the film fluctuated in unison, while at smaller in-plane length scales conformality was lost. Lateral correlations between adjacent layers, however, were shown to exist down to molecular in-plane length scales. In addition, close to the smectic-A–nematic phase transition layer-by-layer thinning was observed above the bulk phase transition temperature. The electron density profiles clearly demonstrate that the nematic layers are expelled from the interior of the film. The temperature dependence of the film thickness could be fitted to a power law.

6.1 Introduction

In the previous chapter it has been shown that diffuse scattering is a powerful tool to study the displacement-displacement correlation function. The aim of the experiments described in this chapter is to step across R_c , the in-plane length scale

where conformality is expected to vanish, or rather, to go beyond the crossover from conformal to independent fluctuations. This requires specific choices for the scattering geometry, as well as for the experimental conditions. As shown in chapter 4 the crossover distance is given by $R_c \sim \sqrt{L/B}$. Therefore, in order to facilitate the observation of loss of conformality in a x-ray scattering experiment, one should choose the experimental conditions such that R_c shifts to large values, and thus to small in-plane wave vector transfer. Both L and B can easily be chosen appropriately. The compressional elastic constant B is expected to vanish, or to reach a finite small value at the SmA-N phase transition [1, 94, 95]. Experimentally, values as small as $1 \times 10^6 \text{ N/m}^2$ have been observed [87, 88, 96]. The compound investigated shows a second order or continuous transition [97], and thus B should indeed vanish. By measuring close to T_{NA} , where the SmA-N transition occurs, one possibility for shifting R_c to larger values has been fulfilled. Moreover, the measurements have been performed on a relatively thick film, additionally a thinner one was investigated to observe effect of thickness on R_c . The use of a (2+2) grazing incidence scattering set-up, as described in sec. 3.2, allowed measurements of the displacement-displacement correlation function down to molecular in-plane distances. The use of this set-up, in combination with the relatively large values of R_c , allowed the observation of the crossover from conformal to independent thermal fluctuations of the smectic layers.

The feasibility of approaching the SmA-N phase transition was restricted by the phenomenon of layer-by-layer thinning. These thinning transitions were recently observed in freely suspended films close to the SmA-I phase transition [84] and close to a weak first order SmA-N phase transition [98]. Instead of rupturing at the bulk phase transition the films lose layers in discrete steps as a function of temperature. In order to obtain the appropriate temperature for the conformality experiment, we have investigated freely suspended films close to the second order bulk SmA-N phase transition using specular reflectivity. This allowed us to ascertain the profile of the total fluctuation amplitude in the film just before thinning. A strong enhancement of the fluctuations in the centre of the film as compared to at the surfaces was observed with fluctuation amplitudes of up to 10 \AA in the interior. In the regime where the thinning transitions occur, the dependence of the film thickness on the temperature can be described by a power law.

In the first section of this chapter the liquid crystal investigated is introduced. Next the specifics of the beamline BM32 at ESRF and the various scan types are

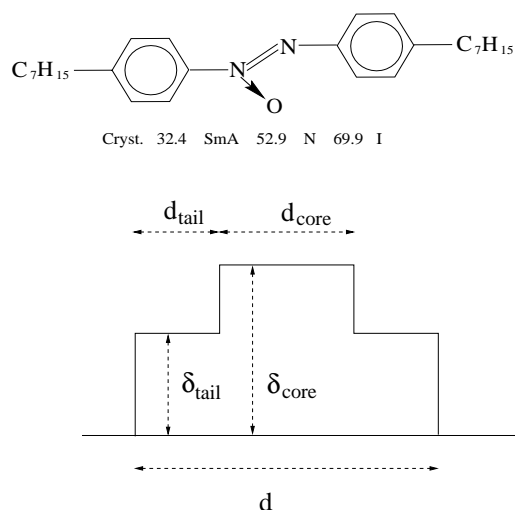


Figure 6.1: *The chemical structure of 7AB with the bulk phase transition temperatures (top), and the model for a single smectic layer (bottom).*

recapitulated. Section 6.3 describes the layer-by-layer thinning results, followed by a discussion. In sec. 6.4 the results of the diffuse measurements on the crossover to non-conformality are presented, followed by a discussion in sec. 6.4.2.

6.2 Experimental

6.2.1 The sample

The compound investigated, 4,4'-diheptyl-azoxybenzene (7AB), is pictured in Fig. 6.1, where the bulk phase sequence is also given. 7AB was obtained from Frinton (Vineland, USA) and was recrystallized several times. The freely suspended films covered an area of $28 \times 10 \text{ mm}^2$, determined by four knife-like blades of a rectangular hole in a steel holder (see sec. 3.3.2). The sample holder was mounted in a cylindrical two-stage oven, described in sec. 3.3.3, which was evacuated and sealed. The thinning experiment has been performed on two films, with thicknesses of 28 and 46 layers. The films were heated in steps of $0.10 \text{ }^\circ\text{C}$ and allowed to equilibrate at each thickness for at least an hour. No thinning was observed over periods of days when the temperature was constant. Likewise, the films did not thicken when the temperature was lowered again.

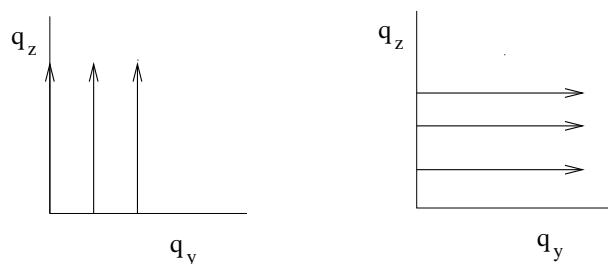


Figure 6.2: *The scans performed: Specular longitudinal scans along the q_z -axis and longitudinal diffuse scans parallel to q_z at an offset q_y (left). Transverse diffuse scans varying q_y at fixed q_z (right).*

The diffuse x-ray scattering measurements were performed at 52.2 ± 0.1 °C, close to the bulk phase transition but far enough to avoid thinning transitions. The investigated film originally had a thickness of 100 layers and was later thinned to 24 layers. Films thicker than about 100 layers were found to be both less uniform and less stable.

6.2.2 Scattering configuration

The layer-by-layer thinning was studied using the in-house specular x-ray reflectivity setup, as described in sec. 3.2.1. The conformality experiment was performed at the beam-line BM32 at the European Synchrotron Radiation Facility ESRF (Grenoble, France). Using a so called (2+2) surface x-ray diffractometer [62], as shown in Fig. 3.14, we measured diffuse intensity by moving the detector and sample out of the plane of reflection, while the angles of the incoming and outgoing wave vector are kept constant with respect to the sample surface. Similar set-ups have recently been used to perform diffuse scattering measurements of multilayers [99, 100] and amphiphilic films [101]. We have taken three types of scans, which are recapitulated in Fig. 6.2: specular longitudinal scans, diffuse longitudinal scans and diffuse transverse scans. Details of the scan types, the applied corrections and the resolution can be found in sec. 3.2.

The out-of-plane grazing incidence (2+2)-scattering set-up does not restrict the accessible in-plane q -range. In combination with the high flux and low background at BM32 at ESRF this allowed the measurement of the diffuse intensity at distances down to molecular dimensions ($\approx 4\text{-}5$ Å), corresponding to $q_y \approx 1.6$ Å⁻¹. Furthermore, transverse scans with large in-plane momentum transfer q_y have been

measured at small q_z where the scattered intensity was high. Thus, both correlations between neighbouring and next nearest layers at $q_z = q_0$ and $q_z = q_0/2$, respectively, could be probed. This in contrast with the set-up used for the experiments in the previous chapter where the maximum in-plane momentum transfer, corresponding to $q_x \approx 0.022 \text{ \AA}^{-1}$, could be reached at the second Bragg peak [48, 60] where the intensity is low. In this case the correlations were probed in q_x , which is equivalent to q_y as the SmA samples are uniaxial along the z axis.

6.3 Thinning transitions

6.3.1 Results

Figure 6.3 shows specular reflectivity curves of films with initially 46 and 28 layers. The curves displayed in the figure have been measured $0.1 \text{ }^\circ\text{C}$ below $T_c(N)$, the maximum temperature where a N layer film is stable. As a function of temperature, melting occurred as a series of discrete transitions. Both the 46 and 28 layer film thinned layer-by-layer, although lack of time prevented measuring more than one thinning transition for the 46 layer film. The 46 layer film lost a layer at $0.9 \text{ }^\circ\text{C}$ above the bulk phase transition, while the thinnest measured film of 12 layers was stable up to $10 \text{ }^\circ\text{C}$ above this transition. Note that even layered films thin layer-by-layer as well, although two inner layers are equivalent.

Reflectivity curves over a larger q_z range than in Fig. 6.3 were measured for a 24 layer film at 45.0 , 52.2 , as well as $56.5 \text{ }^\circ\text{C}$, respectively 11.6 , 4.4 and $0.1 \text{ }^\circ\text{C}$ below $T_c(24)$. These specular scans are displayed in Fig. 6.4. The data at $52.2 \text{ }^\circ\text{C}$ was obtained in a separate experiment at ESRF. Besides the data on the 24 layer film the specular reflectivity of a 12 layer film at $63.2 \text{ }^\circ\text{C}$, $0.1 \text{ }^\circ\text{C}$ below $T_c(12)$, is shown in this figure. The solid line fits are calculated with the reflectivity program *SPEEDO* [91], using the model for a single layer shown in Fig. 6.1. The positions of the Bragg peaks and the Kiessig fringes in the specular reflectivity curve fix d and N , respectively. We find $d = 28.75 \pm 0.05 \text{ \AA}$, $d_{core} = 0.54d$ and $\delta_{core}/\delta_{tail} = 1.5$, independent of film thickness or temperature. The insets of Fig. 6.4 show the profile of the total amplitude of the fluctuations, or layer roughness, in the film. The fluctuations are strongly enhanced in the interior of the film as compared to the surfaces.

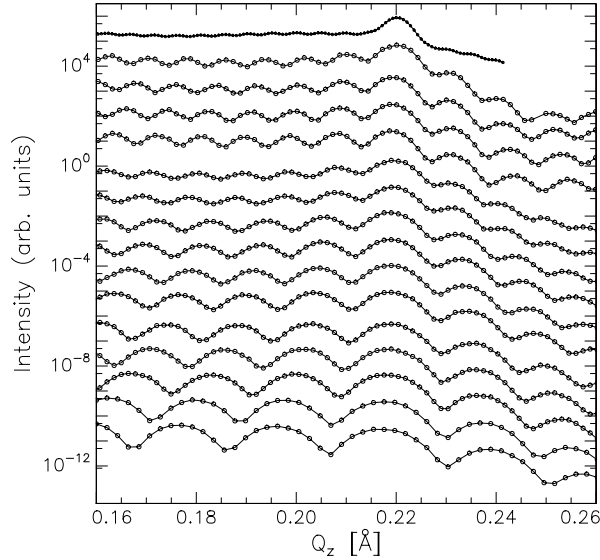


Figure 6.3: *Specular reflectivity curves at 0.1°C below the temperature $T_c(N)$ of melting of the N th layer. The number of layers from top to bottom is 46,28-23,21,19-12. Data for $N = 22$ and $N = 20$ are missing.*

6.3.2 Discussion

Although mean-field models of thinning transitions have been developed [102, 103], a quantitative explanation is still not available. However, the layer thinning data can be described by a simple power law of the form $N(t) = l_0 t^{-\nu}$, where $t = [T_c(N) - T_0]/T_0$ [84, 98]. Figure 6.5 shows a fit of this power law to the experimental data, which yields the following parameters: $l_0 = 4.9 \pm 0.3$, $\nu = 0.68 \pm 0.03$, and $T_0 = 52.10 \pm 0.05^\circ\text{C}$. The value for the exponent can be related to ξ_{\parallel} , the correlation length of the smectic order parameter in the direction parallel to the director [98]. The temperature dependence of ξ_{\parallel} is also described by a power law with an exponent ν_{\parallel} . The value obtained for 7AB is in good agreement with the previously determined values of ν_{\parallel} for other systems [1]. It is in fact in excellent agreement with the critical exponent determined earlier for 7AB using a Fréedericksz transition technique [104]. It also agrees well with the exponents determined by layer-by-layer thinning experiments [84, 98] on other compounds. However, in the case of a second order SmA-N phase transition T_0 should be equal

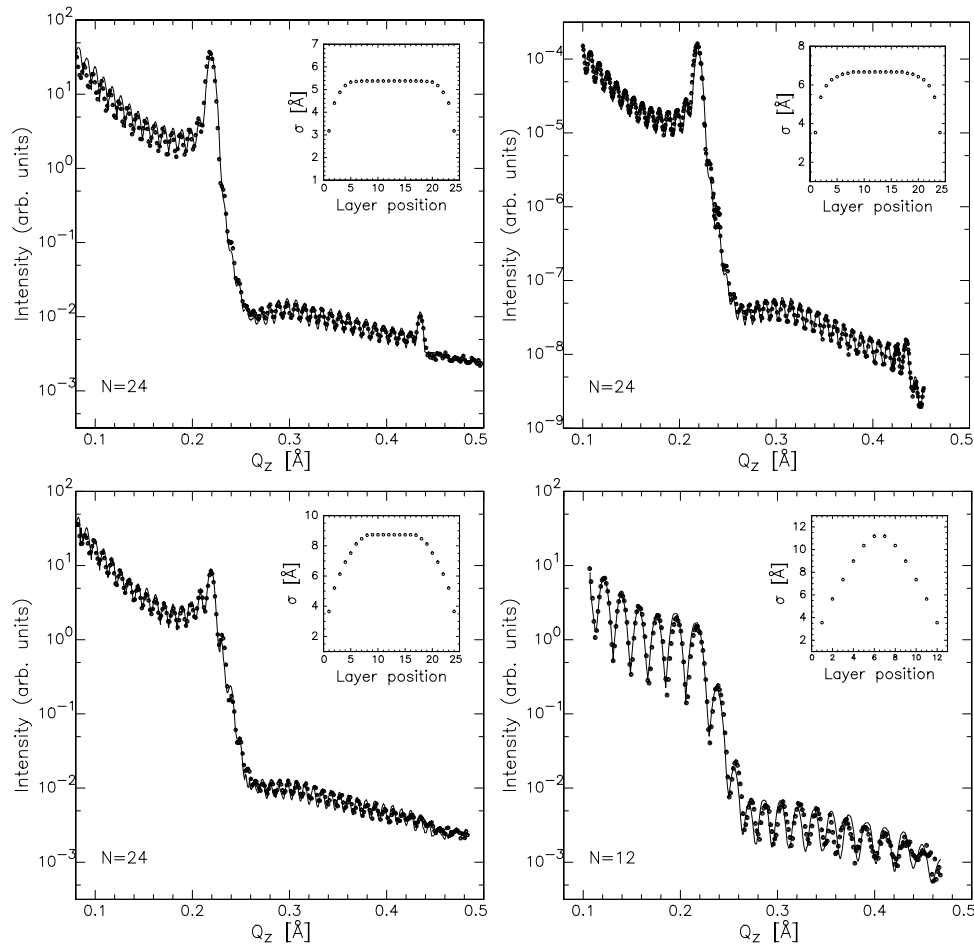


Figure 6.4: *Specular reflectivity curves with a solid line fit to the data. A 24 layer film at 45.0 , 52.2 and 56.2 °C, where $T_c(24) = 56.3^\circ\text{C}$, and a 12 layer film at 63.0°C, 0.1°C below $T_c(12)$. The inset shows the total amplitude of the fluctuations in the film.*

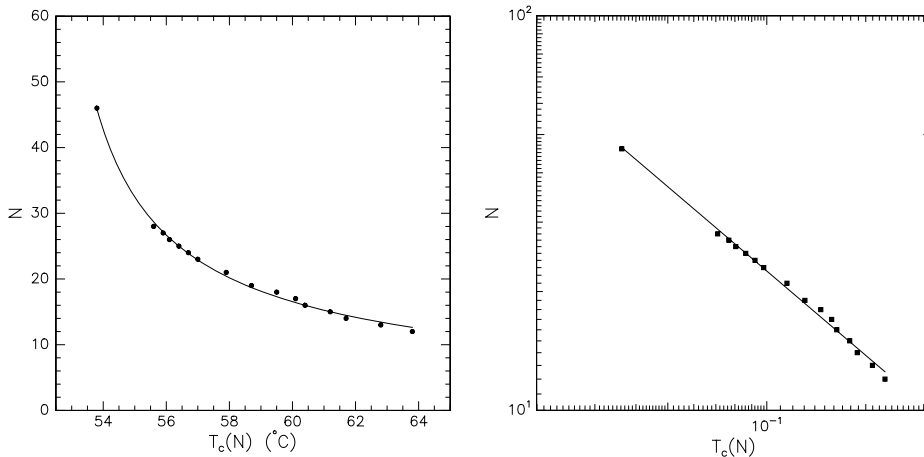


Figure 6.5: *The number of layers of a freely suspended film versus $T_c(N)$, the highest temperature where the N layer film is stable.*

to T_{NA} whereas we find a value that is 0.8°C lower. This discrepancy is the consequence of the absence of accurate thick film data. Inclusion of the roughly determined thinning temperature for a 100 layer film, obtained in a separate experiment at ESRF, gives $T_0 = T_{NA} \pm 0.07^\circ\text{C}$. Thus, more accurate measurements of thicker films are needed to provide a better determination of T_0 .

Qualitatively, Fig. 6.4 shows that melting starts in the interior of the film, for the Bragg peaks disappear upon approaching T_{NA} , while the amplitude of the Kiessig fringes is constant [105]. The enhanced order at the surfaces of the film is quite distinct in the electron density profiles shown in Fig. 6.6. In our analysis the melting can be described by divergence of the amplitude of the total fluctuations, as shown in the insets of Fig. 6.4. While the amplitude of the fluctuations remains relatively constant at a value of approximately 3.5 \AA in the surface layers of the film, the amplitude in the centre increases from 5.4 to 9.3 \AA for the 24 layer film upon approaching T_{NA} . In the latter case the film is still 0.1°C from the thinning transition. From the fit to the 12 layer film data an even larger fluctuation amplitude, 11.2 \AA , of the interior layers is obtained. It is interesting to recall that all the data of the 24 layer film could be fit using the same molecular form factor, *i.e.* using the same values for d , d_{core} , and $\delta_{core}/\delta_{tail}$. The equivalence of the molecular form factor at the lowest and highest temperature scans is reasonable, as

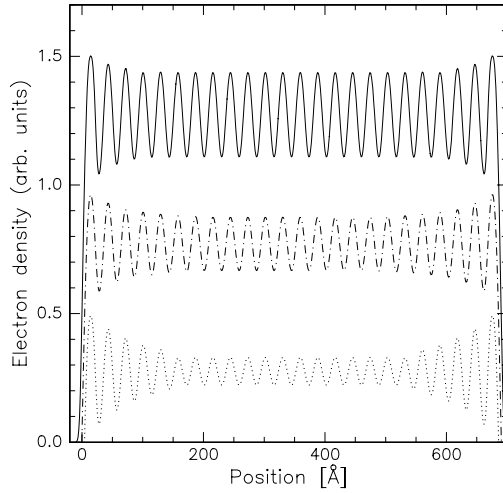


Figure 6.6: *The electron density profile in a 24 layer film at, from top to bottom, 45.0, 52.2 and 56.2 °C. The bottom two curves are shifted.*

the temperature difference is only 11 °C. It is therefore unlikely that the molecular conformation will show large variations. This strongly suggests that the complete disappearance of the second order Bragg peak is rather due to the profile of the fluctuations than to the large amplitude of the fluctuations.

The layer-by-layer thinning experiment clearly demonstrates a strong profile of the total amplitude of the fluctuations in the film close to the bulk SmA-N phase transition. The specular reflectivity depends both on the contribution of the layer fluctuations and the uncorrelated local molecular disorder: $\sigma_{tot}^2 = \sigma^2 + \sigma_{loc}^2$. It cannot separate thermal fluctuations and local disorder, however. In order to study the correlation in the thermal fluctuations we continue with the diffuse x-ray scattering experiment.

6.4 Loss of Conformality

6.4.1 Results

The specular and diffuse longitudinal scans for the 24 layer film are presented in Fig. 6.7. At small q_y the film is conformal and the diffuse scattering is the

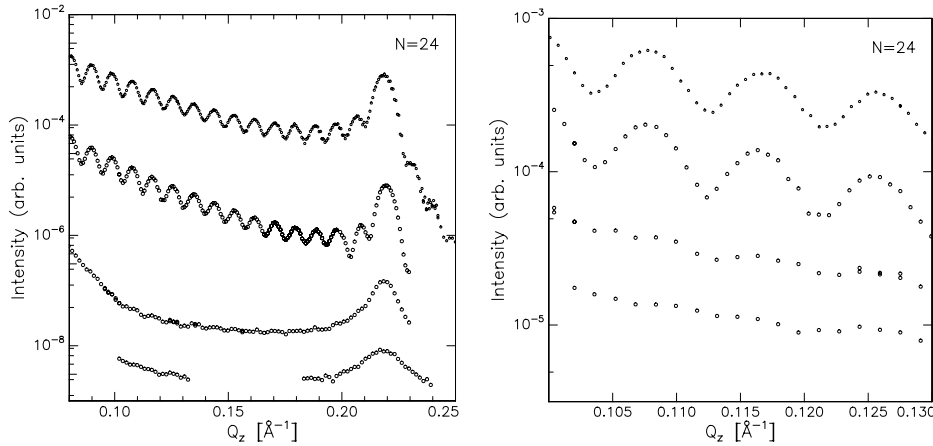


Figure 6.7: *Specular* ($q_y = 0$, upper curves) and *diffuse radial scans* with from top to bottom $q_y = 0.0064 \text{ \AA}^{-1}$, $q_y = 0.0191 \text{ \AA}^{-1}$ and $q_y = 0.0414 \text{ \AA}^{-1}$ for a 24 layer film. Curves have been shifted for clarity; q_z -range up to Bragg peak (left) and a magnification of small q_z range (right).

coherent superposition of scattering from each layer, showing maxima and minima at the same positions as the specular reflectivity [42]. The disappearance of the interference fringes with increasing q_y indicates that the top and bottom of the film no longer fluctuate in unison. This disappearance is more apparent in the enlargement of a smaller q_z -range in Fig. 6.7. The persistence of the Bragg peak up to $q_y = 0.0414 \text{ \AA}^{-1}$ ($R \approx 150 \text{ \AA}$), however, shows that lateral correlation between adjacent layers still exists. The broadening and weakening of the Bragg peak reveals that the correlation length ξ_{\parallel} is smaller than the total film thickness; with increasing in-plane momentum transfer more layers fluctuate independently and thus less layers are contributing coherently to the diffuse signal.

More direct information about the displacement-displacement correlation function can be obtained from the transverse diffuse scans. Scans were done across the first Bragg peak where $q_z = 0.218 \text{ \AA}^{-1}(q_0)$, across a sub-harmonic of the Bragg peak at $q_z = 0.109 \text{ \AA}^{-1}(0.5q_0)$ and at an intermediate interference fringe at $q_z = 0.152 \text{ \AA}^{-1}(0.7q_0)$. Transverse scans for a 100 and a 24 layer film of 7AB are shown in Fig. 6.8. The curves are not shifted with respect to each other. At small q_y the slopes of the transverse scans are approximately parallel at all q_z , therefore

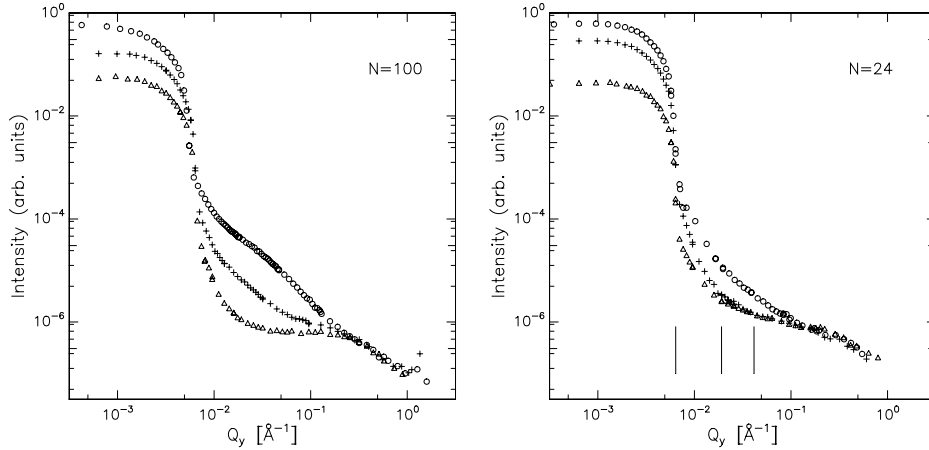


Figure 6.8: *Transverse diffuse scans at the positions $q_z = 0.218 \text{ \AA}^{-1}(q_0)$ (dots), $q_z = 0.109 \text{ \AA}^{-1}(0.5q_0)$ (crosses) and $q_z = 0.152 \text{ \AA}^{-1}(0.7q_0)$ (triangles). The vertical solid lines indicate the offsets where longitudinal diffuse scans have been taken. Curves have not been shifted with respect to each other.*

all the layers are fluctuating in unison. The development of different slopes in the various scans is the signature of loss of conformality of the thermal fluctuations with increasing in-plane momentum transfer (decreasing length scales).

All the curves in Fig. 6.8 coincide at a large q_y , corresponding to $R \leq 40 \text{ \AA}$ for both films. For shorter in-plane distances the diffuse intensity decays logarithmically with decreasing distance. The absolute diffuse intensities of the 24 and 100 layer film coincide in this q_y range as well. In this regime of short lateral distances correlations between individual molecules are probed and the application of continuum theory is questionable.

6.4.2 Discussion

The occurrence of loss of conformality is immediately clear from Fig. 6.7. This qualitative result is confirmed by the transverse scans. The slopes are still very similar, even for $R < R_c$, at the Bragg peak and at the sub-harmonic, in particular for the 100 layer film. The dominant contributions to the diffuse scattering are from lateral correlations between adjacent and next nearest layers, respectively. This indicates that lateral correlations between adjacent and next nearest layers

persist down to molecular length scales. At the same time the very different slope of the scan at $q_z = 0.7q_0$, where only correlations between more distant layers are constructively interfering, confirms that conformality between top and bottom of the film is lost. However, quantitative analysis of the data was arduous. The data has been fitted using

$$\frac{I(\mathbf{q})}{I_0} = \left[|R_F|^2 \exp(-q_z^2 \sigma_{loc}^2) \frac{\Delta q_x \Delta q_y}{2\pi} \int_{-\infty}^{\infty} \int_{-\infty}^{\infty} dx dy \exp(-i(q_x x + q_y y)) \cdot \exp\left[-\frac{1}{2}x^2 \Delta q_x^2\right] \exp\left[-\frac{1}{2}y^2 \Delta q_y^2\right] G(R, q'_z) \right] * \exp\left[-\frac{1}{2}q_z^2 / \Delta q_z^2\right], \quad (6.1)$$

with

$$G(R, q'_z) = \sum_{m,n}^N \exp[iq'_z(m-n)d] \exp[-q_z'^2 g_{mn}(R)/2]. \quad (6.2)$$

This expression is completely analogous to Eq. (5.4) in sec. 5.3, but now involves a three dimensional resolution convolution. The correlation function $g_{mn}(R)$ has been calculated using Eq. (4.42).

Several problems arose in the fitting. Firstly, as discussed in sec. 3.2.4, the resolution component Δq_x was not as well known as in previous in-house experiments. Secondly, in the transverse scans the region at small q_y where capillary waves dominate the fluctuations, as discussed in sec. 4.4, is hidden by the relatively large experimental resolution. Therefore we determined the surface tension of 7AB from the line shape of a transverse scan in a two circle reflectivity set-up as in refs. [48, 60], giving $\gamma = 25.0 \times 10^3$ N/m². This is in excellent agreement with the results of a direct surface tension measurements of 7AB [106]. As the large q_y values caused the fitting to be very time-consuming, K was not treated as an independent parameter, but assumed to have the nematic value of $K = 1.2 \times 10^{-11}$ N [104, 107, 108]. Best fits to the transverse scans using those values are shown in Fig. 6.9 for both film thicknesses. This results in $B = (1.0 \pm 0.5) \times 10^7$ N/m², which is in the same range as values obtained from measurements on other bulk systems close to the smectic-nematic phase transition [87, 88]. Using the above values for B, K and γ , and the values for d, d_{core} and $\delta_{core}/\delta_{tail}$ from sec. 6.3.1 the longitudinal diffuse scans were fitted, as shown in Fig. 6.10

The fits do show the same general trend as the data. However, agreement of data and theory is limited to small q_y -values, at larger q_y considerable deviations exist, especially for the 100 layer film. Although all fits were performed using $\sigma_{loc} = 1.0$ Å the specular scan and the longitudinal diffuse scan with

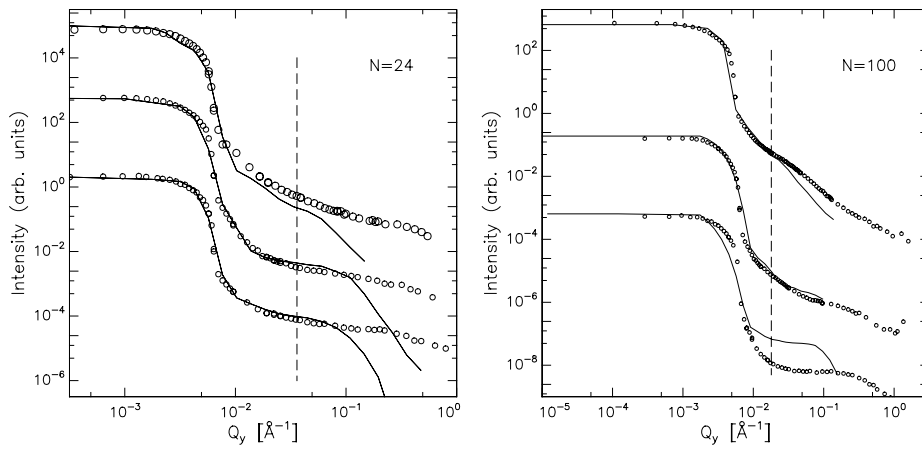


Figure 6.9: The transverse scans from Fig 6.8 with as the solid line the fit as described in the text. From top to bottom $q_z = q_0$, $q_z = 0.5q_0$ and $q_z = 0.7q_0$. The vertical dashed line indicates $2\pi/R_c$.

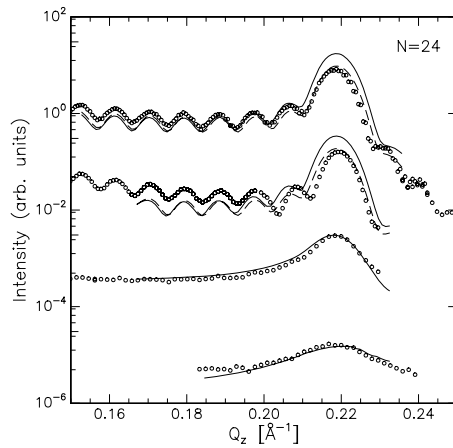


Figure 6.10: Longitudinal scans from Fig. 6.7 with as the solid line the fit as described in the text.

$q_y = 0.0064 \text{ \AA}^{-1}$ can be better modelled assuming a profile of σ_{loc} . Figure 6.10 shows as the dashed line a fit were σ_{loc} varies from 1 to 4 \AA from the surface to the interior of the film for these two scans. It is obvious that the other two curves cannot be fit using this profile. The mere existence of a profile of the local smectic (dis)order can easily be calculated. Since $\nu = \gamma/\sqrt{KB} = 2.2$, as discussed in sec. 4.4, the surface tension quenches the fluctuations at the surfaces of the film compared to the interior. For the above values of B , K and γ the amplitudes of the thermal fluctuations, σ , are 3.4 \AA and 3.7 \AA at the surface and centre of the 24 layer film, respectively. Therefore, the thermal fluctuations hardly have a profile. As σ_{tot} is known from Fig. 6.4, we calculate using $\sigma_{tot}^2 = \sigma_{loc}^2 + \sigma^2$, a profile for the local disorder with amplitudes σ_{loc} , 5.3 and 0.9 \AA at the interior and surface of the film, respectively. This is in reasonable agreement with the local profile shown in the dashed lines in Fig. 6.10. Thus, although the thermal fluctuations hardly have a profile, the local fluctuations are strongly enhanced at the interior of the film. The existence of such a pronounced profile in the amplitude of local fluctuations strongly suggests the existence of a profile in the smectic order parameter. B is proportional to the square of the smectic order parameter [10], which was introduced in sec. 1.3. Therefore, a profile of B in the film would not only influence the profile of the local fluctuational amplitude in the film, but also the correlations between the fluctuations [109]. This is an issue still under investigation, as it could possibly explain the deviations between data and fits. We stress once again that the uncertainty about Δq_x could also be of importance here.

The vertical dashed lines in Fig. 6.9 indicate the in-plane wave vector transfer corresponding to $R_c = 2\sqrt{L\lambda}$ (see sec. 4.4), where loss of conformality is expected. The values for both the 24 layer and 100 layer films, $R_c \approx 170 \text{ \AA}$ and $R_c \approx 350 \text{ \AA}$, respectively, agree reasonably well with our experimental observations. The first and second diffuse longitudinal scan for the 24 layer film were taken at $R > R_c$, this is consistent with the presence of interference fringes. The third scan is taken in the regime where correlations between the layers are vanishing ($R < R_c$). Figure 6.11 shows $\langle [u(\mathbf{R}, z) - u(0, z')]^2 \rangle$ as a function of lateral distance for different layer indices for both films. It is obvious that the slopes for nearest and next-nearest layers are quite similar, while the curve for *e.g.* top and bottom of the film shows an immediate crossover at R_c .

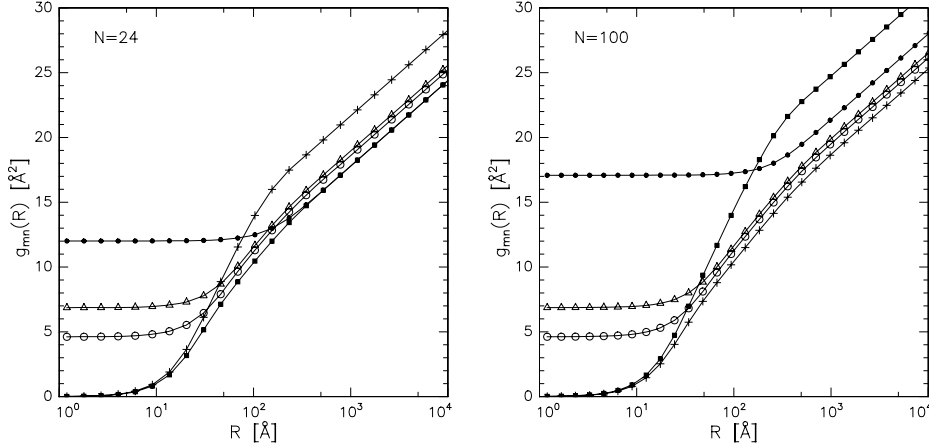


Figure 6.11: The full correlation function for a 24 and 100 layer γAB film, respectively calculated using $B = 1 \times 10^7 N/m^2$, $\gamma = 2.5 \times 10^{-2} N/m$ and $K = 1.2 \times 10^{-11} N$. Left: $g_{1,1}$ (filled squares), $g_{1,2}$ (open circles), $g_{1,3}$ (triangles), $g_{1,24}$ (filled circles) and $g_{12,12}$ (crosses). Right: $g_{1,1}$ (crosses), $g_{1,2}$ (open circles), $g_{1,3}$ (open triangles), $g_{1,100}$ (filled circles) and $g_{50,50}$ (filled squares).

6.5 Conclusions

A crossover from conformal to independent fluctuations was observed in freely suspended SmA films of 100 and 24 layers. The adapted scattering geometry for diffuse scattering, in combination with the high flux and low background at BM32 at ESRF, allowed us to determine the in-plane wave vector dependence of the hydrodynamic (collective) fluctuations down to in-plane length scales comparable to the lateral distances between molecules ($R \approx 4-5 \text{ \AA}$). Conformality was lost first between top and bottom of the film, while lateral correlations between adjacent layers and next nearest layers were shown to persist down to molecular length scales. Quantitative analysis strongly suggests the necessity of including a profile of the smectic order parameter in the theoretical model. Layer thinning transitions in freely suspended films indicate a strong enhancement of the amplitude of the fluctuations in the interior of freely suspended films.

7

The molecular formfactor

7.1 Introduction

The packing of liquid crystalline molecules is an important aspect of the very existence of smectic phases. Nevertheless, quantitative aspects of the packing problem have usually been restricted to a comparison of d -spacings, as measured by x-ray diffraction, and the length l of the molecules. A more complete approach should also include the molecular volume, the molecular formfactor and the effects of fluctuations on the distribution of the centres of mass of the molecules in the layers [8]. The origin of the smectic layering is in principle well known. In the first place the anisotropic molecular shape does not only contribute to the orientational order, but also to the smectic layering. Computer simulations of hard spherocylinders have demonstrated both a nematic and smectic phase [110]. Secondly, the difference in interactions between the aromatic core and the aliphatic chains should be considered. In the smectic model of McMillan [111] the attractive interactions are assumed to be more or less localized in the central part of the molecules. The alkyl chains are assumed merely to fill space. In this picture the formation of smectic layering is related to the incompatibility of the core and the endgroups [112]. This incompatibility is in fact very similar to the microphase separation in diblock copolymers.

The expression “smectic layers” is somewhat misleading, for the density mod-

ulation in the z direction is weak. As has been already discussed in chapter 1 this modulation can be considered as a convolution of the molecular formfactor and the distribution function of the centres of gravity of the molecules $f(z)$, where the latter is defined in Eq. (1.4). Therefore, in an x-ray experiment the formfactor $F(z)$ and the distribution function cannot be separated. The order parameter ratio τ_2/τ_1 can be related to the scattered intensity I at the first and second Bragg peak [8, 113]:

$$\frac{I(2q_0)}{I(q_0)} = \frac{1}{2} \left| \frac{F(2q_0)\tau_2}{F(q_0)\tau_1} \right|^2, \quad (7.1)$$

where $\tau_{1,2}$ have been defined in Eq. (1.5) and q_0 is the position of the Bragg peak. Usually the formfactor is calculated assuming a reasonable average conformation and orientation of the molecules [39, 114], which introduces considerable ambiguities. On the other hand it is quite common to make assumptions about the distribution function [8, 115]. In the analysis of the data described in this thesis we have assumed the fluctuations of the molecular centres of mass along the z -axis to be of Gaussian form. In this case we can write

$$f(z) = \frac{1}{\sqrt{2\pi\sigma_{tot}^2}} \exp\left(\frac{-z^2}{2\sigma_{tot}^2}\right), \quad (7.2)$$

which fixes the order parameters to

$$\tau_n = \exp\left(\frac{-2\pi^2 n^2 \sigma_{tot}^2}{d^2}\right) = \tau_1^{n^2}. \quad (7.3)$$

Inserting this in Eq. (7.1) leads to

$$\frac{I(2q_0)}{I(q_0)} = \frac{F(2q_0)^2}{2F(q_0)^2} \exp\left(\frac{-6\pi^2 \sigma_{tot}^2}{d^2}\right). \quad (7.4)$$

The above expression clearly demonstrates that if a Gaussian distribution function is assumed, the intensity ratio of the first and second Bragg peak is fixed.

Both the collective layer fluctuations and the local molecular disorder contribute to $f(z)$:

$$\sigma_{tot}^2 = \sigma^2 + \sigma_{loc}^2. \quad (7.5)$$

Quite generally the latter contribution has been neglected [8, 28, 39]. The use of diffuse x-ray scattering allowed us to determine the collective layer fluctuations.

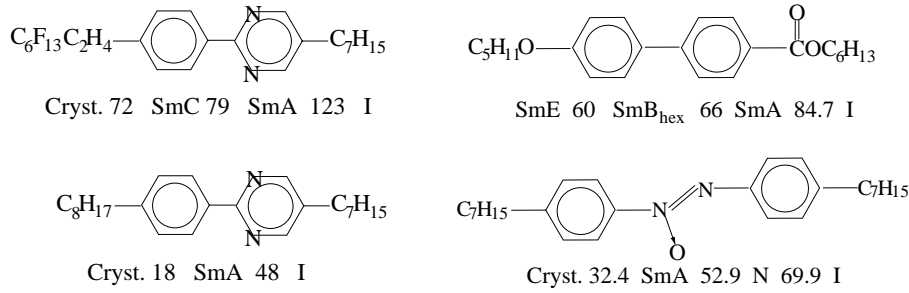


Figure 7.1: Structure formulas of the liquid crystals: FPP (top left), HPP (bottom left), 65OBC (top right), and 7AB (bottom right).

Therefore one contribution to the distribution function can be independently determined. In the analysis it is assumed that both thermal and local fluctuations are well described by Gaussians. Furthermore, a simple slab model is used to model a single smectic layer. In this final chapter some of the consequences of these assumptions will be elucidated. In sec. 7.2 the molecules that we compared will be (re)introduced, followed by the experimental details. In sec. 7.2 the results are presented, followed by a discussion on basis of the slab model. In the final section the formfactor which is obtained from the simple slab model will then be compared with a formfactor calculated assuming a reasonable molecular conformation.

7.2 Experimental results

Four liquid crystals have been investigated, two of which, FPP and 7AB, were already introduced in chapter 5 and 6, respectively. The other compounds are 4-heptyl-2-[4-heptyl-phenyl]-pyrimidin (HPP) and hexyl-4'-pentyloxy-biphenyl-4-carboxylate (65OBC). The molecules are pictured in Fig. 7.1. Measurements have been performed at 88 °C for FPP, at 25 °C for HPP, at 45 °C for 7AB, and at 76 °C for 65OBC, respectively, all well into the SmA phase. The compounds were studied with specular and diffuse reflectivity using the setup described in sec. 3.1. Corrections and resolution factors have all been accounted for as described in that section. Most data of FPP and 7AB has been presented in the chapters 5 and 6. For 7AB we only show a specular scan obtained at the Troika beamline at ESRF, using a high resolution setup ($\Delta q_z = 3 \times 10^{-4} \text{ \AA}^{-1}$). For HPP both specular and diffuse data have been measured, although transverse rocking scans were only

Table 7.1: *The best fit parameters for the four compounds studied. The missing parameters for 65OBC have not been determined. Parameters indicated with * were obtained from literature, as described in the text. For 7AB both values at the surface and interior of the film are given.*

parameter	FPP	HPP	7AB	65OBC
d (Å)	29.40 ± 0.04	28.15 ± 0.05	28.75 ± 0.05	25.99 ± 0.05
d_{core}/d	0.62	0.50	0.54	0.57
$\delta_{core}/\delta_{tail}$	0.88	1.51	1.50	1.61
σ_{loc} (Å)	2.6	0.8 ± 0.3	$0.8 - 3.9$	-
σ_{tot} (Å)	4.6	3.0	$3.5 - 5.4$	2.9
B ($\times 10^{-7}$ N/m ²)	75 ± 25	3.0 ± 1.5	1.0 ± 0.5	-
K ($\times 10^{11}$ N)	1.0 ± 0.5	1.5 *	1.2 *	-
γ ($\times 10^3$ N/m)	13.0 ± 0.5	25.0 ± 1.0	25.0 ± 0.5	20.8 ± 0.5 *

possible at the first Bragg peak. The compound 65OBC was only studied using specular reflectivity.

Figure 7.2 shows the specular reflectivity curves for a 33 layer 7AB film, for 4 and 10 layer 65OBC films, for 2, 13, 20 and 25 layer HPP films, and finally a comparison of a 20 layer HPP film to a 20 layer FPP film. Note the strong second order Bragg peak in both the 65OBC and FPP films, compared to the total absence of a second order for the HPP samples, even for the thicker films.

In the analysis of the data a single smectic layer has been approximated by the simple slab model shown in Fig. 7.3. The 7AB and FPP data were modelled using the parameters as described in chapters 5 and 6; the fit parameters used are collected in table 7.1. The values of 7AB are given for surface and interior of the film, respectively. The data of 65OBC were only fitted using a standard dynamical reflectivity program (*SPEEDO*). For 7AB the existence of a strong profile in the fluctuations has been described in chapter 6. The value of K for 7AB shown in the table was obtained from [104, 107, 108], while the value for σ_{loc} has been calculated assuming a constant B throughout the film. Contrary to 7AB, σ_{tot} is independent of layer position for the other compounds. For HPP, transverse scans were only possible at the Bragg peak, which only allowed determination of the surface tension. The bending elastic constant K of HPP is not known, therefore

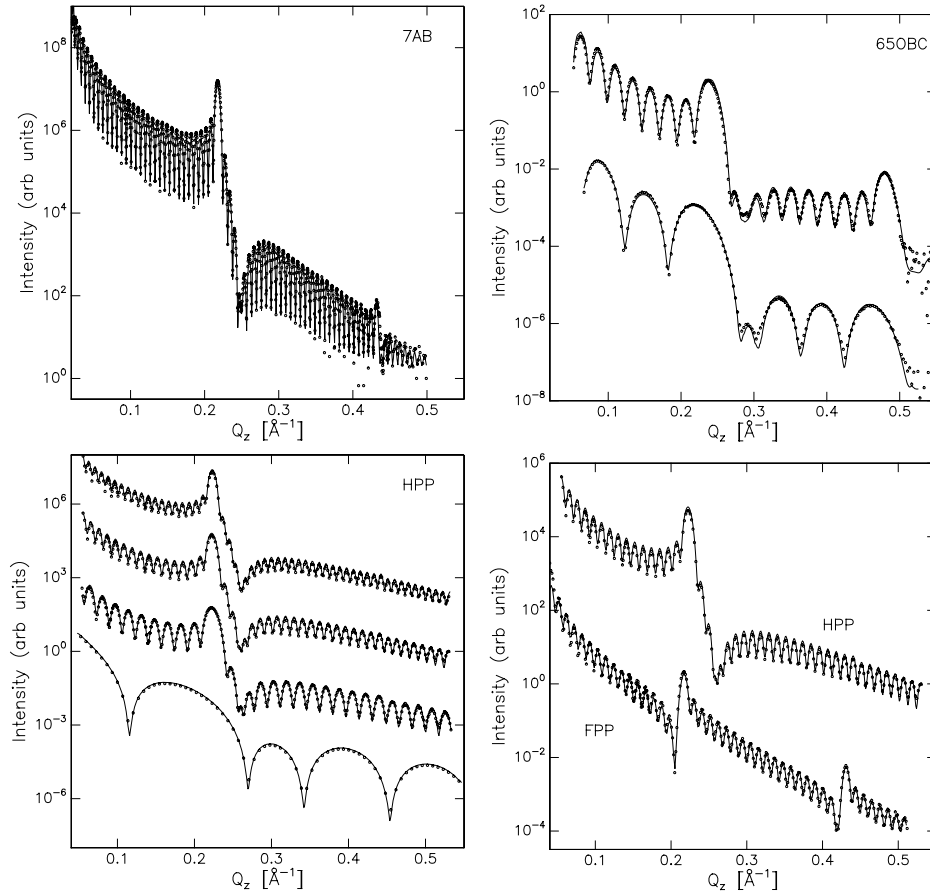


Figure 7.2: *Specular reflectivity curve for a 33 layer 7AB film (top left), for 4 and 10 layer 65OBC films (top right), for 2, 13, 20 and 25 layer HPP films (bottom left) and finally for 20 layer HPP and FPP films (bottom right).*

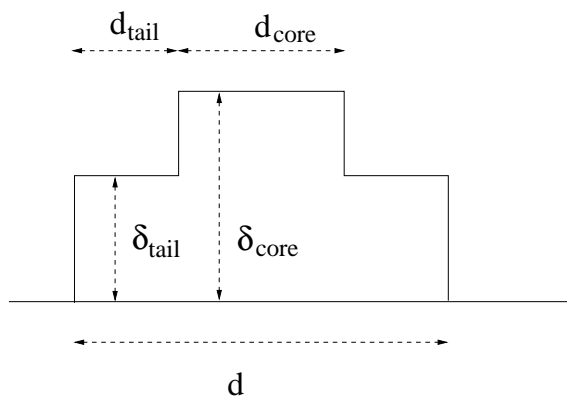


Figure 7.3: *The slab model used to describe a single smectic layer. The molecules are assumed to be up-down symmetric in the layers.*

we assumed its value to be similar to that of an alkyloxy-phenylpyrimidin of the same length [116]. This is a reasonable assumption as K was very similar for other compounds that differed only with respect to the alkyl or alkyloxy chain [117]. In essence this allows a crude determination of B on the basis of Eq. (7.5), for σ cannot be larger or much smaller than σ_{tot} . With this assumption for K we approximate $B = 3.0 \pm 1.5 \times 10^7 \text{ N/m}^2$, which gives $\sigma_{loc} = 0.8 \pm 0.3 \text{ \AA}$. Neither σ , nor σ_{loc} show a profile assuming these values.

7.3 Discussion

First we note that FPP and HPP, which differ only in one alkyl chain, have very different properties. The fluorinated tail causes B to be large and γ to be small. The higher amplitude of the thermal fluctuations of FPP, however, can be entirely related to the difference in surface tension. The ratio $\nu = \gamma/\sqrt{KB}$ determines not only whether the thermal fluctuations are enhanced or compressed at the surface, but also the magnitude of the amplitude. For FPP, $\nu \lesssim 1$, therefore the thermal fluctuations are slightly enhanced at the surfaces. The same is true for the amplitude of the local molecular disorder. For HPP, $\nu \gtrsim 1$ and thus the surface tension slightly suppresses the amplitude of the fluctuations at the surface of the film. For FPP, the large value of B suppresses the amplitude of the fluctuations, however, this is more than compensated by the small surface tension. In the case of 65OBC diffuse measurements have not been performed. In spite of this, since the

surface tension is known [85], some statements can be made. As σ_{tot} is relatively small (see table 7.1), ν also must be small, which implies that \sqrt{KB} must be rather large. To illustrate this; if K were 1×10^{-11} N, which is a reasonable value, we find $B > 5 \times 10^8$ N/m². On the other hand if a common value for B is assumed, such as $B = 5 \times 10^7$ N/m², a value of $K > 5 \times 10^{-11}$ N is obtained.

Let us now discuss the parameters $d, d_{core}/d$ and $\delta_{core}/\delta_{tail}$ for the various compounds, which are summarized in table 7.1. Starting with the d values, we found that the HPP data could only be fitted well assuming a 9° tilt of the toplayers. In fact, the d -spacing of the 2 layer film was only 27.65 Å, corresponding to an even slightly higher tilt of 11° for both layers. Without introducing these tilted outerlayers the model calculation gave rise to a much too deep minimum in intensity after the first Bragg peak. For none of the other compounds evidence for tilted toplayers has been found. Both the 4 and 10 layer 65OBC data could be modelled assuming $d = 26.0$ Å. We have already discussed in chapter 5 that all data of films with thicknesses varying from 3 to 150 layers of FPP could be fitted assuming the same d spacing. This was also true for 7AB, and in fact independent ellisometric measurements on freely suspended films of 7AB [93] confirmed the absence of a tilt.

In the slab model the ratio d_{core}/d determines the strength of the second harmonic. The formfactors calculated from the slab model are shown as the solid lines in Fig. 7.4. For HPP the second order Bragg peak is totally absent as $d_{core} = 2d_{tail}$, so that the formfactor has a minimum exactly at position $q_z = 2q_0$. Thus, on the basis of the slab model, the disappearance of the second order Bragg peak of HPP is entirely due to the molecular formfactor. For 7AB, a weak peak remains, with a minimum of the formfactor at $q_z \gtrsim 2q_0$. The compound 65OBC has a strong second order Bragg peak as the minimum of the formfactor is found for $q_z > 2q_0$. The high ratio $\delta_{core}/\delta_{tail}$, which determines the strength of the Bragg peaks, makes this effect even more pronounced. FPP has a strong second order peak as well. Now the interference minimum shifts has been shifted to $q_z < 2q_0$, as the density termination at the air-film interface is highest ($\delta_{tail} > \delta_{core}$) due to the fluorinated tail of FPP. Fluorinated compounds are well-known for their strong higher order peaks [90, 115, 118]. In the case of the thickest investigated FPP film of 150 layers, originally shown in Fig. 5.5, a third order Bragg peak could even be measured. Both the specular and transverse rocking scans at the third Bragg peak are displayed in Fig. 7.5. The well-defined peak in the latter indicates that the

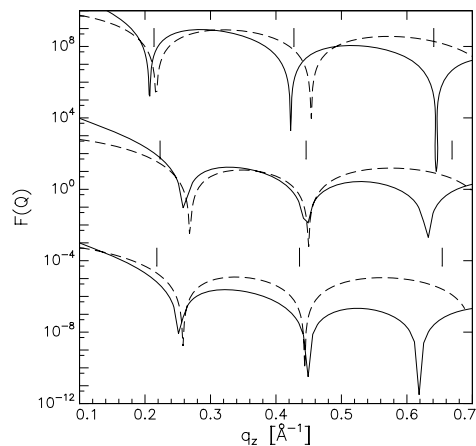


Figure 7.4: *The molecular formfactors, where the solid line is calculated using the slab model and the dashed line is the Fourier transform of the electron density of an up-down symmetric molecule projected on the z -axis. From top to bottom FPP, HPP and TAB. The vertical solid lines indicate q_0 and $2q_0$, respectively.*

specular peak is not only caused by diffuse scattering. The solid line through the data is the fit using the parameters from chapter 5, in which information about the third order was not included. Evidently, the simple slab model convoluted with a Gaussian distribution function describes all three orders of Bragg peaks well.

Although the model agrees with the data, the parameters cannot always be related to the structure of the molecules themselves. For the three non-fluorinated compounds we find $d_{core}/d \approx 0.50$, which corresponds to $d_{core} \approx 14 \text{ \AA}$, whereas the length of the core from a molecular model is only $9 - 10 \text{ \AA}$. Likewise d_{tail} of the fluorinated liquid crystal appears to be short, while the ratio $\delta_{tail}/\delta_{core}$ of 1.14, as obtained from the fit, is expected to be around 1.50 from the molecular models. It is clear that the electron density profile of two up-down symmetric molecules cannot directly resemble the schematic in Fig. 7.3. To investigate this problem further, the molecular formfactors obtained from the slab model in Fig. 7.3 have been compared with the formfactors calculated by Fourier transforming the electron density profiles of up-down symmetric molecules projected onto the z -axis [114]. The optimum conformations of the molecules were calculated using the commercially available molecular modelling package *CHEM-X* [119]. Assuming

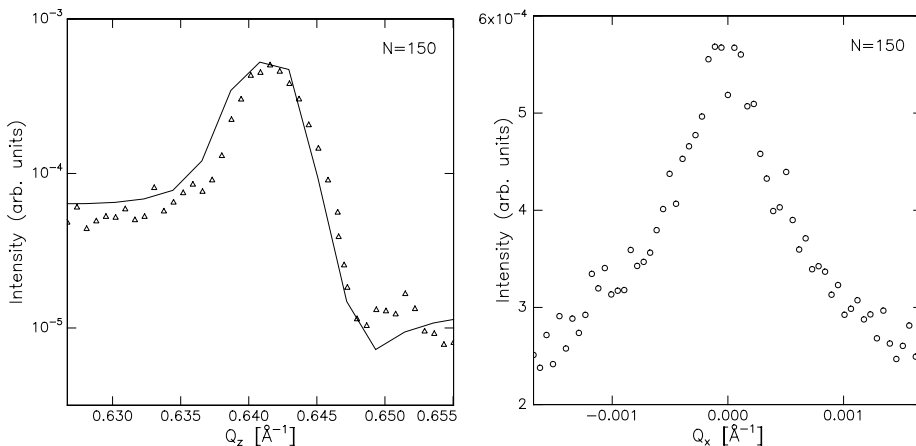


Figure 7.5: *Specular reflectivity curve of a 150 layer FPP film (left) and the transverse scan across the peak (right). The solid line is the fit using the parameters discussed in chapter 5.*

up-down symmetry in the layers we calculate

$$F(q_z) = q_z^2 \left| \int \rho(z) \exp(iq_z z) dz \right|^2. \quad (7.6)$$

In this calculation we disregard orientational disorder of the molecules. The formfactors obtained this way are shown as the dashed lines in Fig. 7.4, while those using the slab model are displayed as the solid lines. The molecular calculations are very sensitive to details in the molecular models in the vicinity of wavevectors where $q_z = nq_0$ [90]. In all cases the first minimum shifts to larger q_z if the z axis was chosen to be the axis through the two outermost para-positions of the aromatic rings. Best agreement with the slab model was obtained when the z axis was taken parallel to the alkyl chains. For HPP and 7AB both formfactor models predict a minimum near the position of the second Bragg peak, while the position of the first intensity minimum with respect to the first Bragg peak is also accounted for. For FPP the agreement between the two models is less satisfactory at the second Bragg peak. Here the molecular model predicts a minimum in intensity at the high q_z side with respect to the Bragg peak, while exactly the opposite is found in reality. This could be related to the existence of a SmA_d phase, in which the molecules partially overlap, and the fluorinated tails phase separate from the core

and alkyl chains [90, 120, 121]. Such a SmA_d model allows the determination of a compromise between the degree of overlap of two molecules and the value for d . However, this would introduce even more free fitting parameters. On the basis of our analysis we cannot yet discriminate between a SmA or SmA_d phase.

On the basis of the comparison given none of the formfactor models can be rejected. The molecular model is more intuitive, but has the disadvantage of being rather sensitive to the molecular conformation in the vicinity of $q_z = nq_0$. Thus it should be treated with some caution. The slab model has the advantage of being restricted to a fewer parameters. It is questionable what the parameters d_{core}/d and $\delta_{core}/\delta_{tail}$ really mean, however. Finally, the order parameters have been fixed by the assumption of a Gaussian distribution function. All differences between molecules have been lumped together in the formfactor, while they could possibly also be explained by a non-Gaussian distribution. This would allow different ratios of τ_2/τ_1 for various types of molecules. In principle it is difficult to decide whether such differences or variations in the formfactor determine the x-ray intensity. However, given the fact that three orders of Bragg peaks for FPP can be well described, we can conclude that the Gaussian form is a reasonable assumption for this case within the framework of our model.

7.4 Conclusions

The molecular formfactor, as obtained from a simple slab model, has been compared to a formfactor obtained directly from molecular modelling. They have been found to be quite similar. The deviations can in principle be contributed to the simplifications in the molecular modelling, with respect to the choice of the long molecular axis and the neglect of orientational disorder. A crucial element in our model is the choice for a Gaussian distribution function of the centres of mass of the molecules. The results indicate that this choice is quite plausible.

Bibliography

- [1] *See e.g.* P. G. de Gennes and J. Prost, *Physics of Liquid Crystals* (Clarendon Press, Oxford, 1993).
- [2] *See e.g.* G. Vertogen and W. H. de Jeu, *Thermotropic Liquid Crystals, Fundamentals* (Springer, Berlin, 1988).
- [3] *See e.g.* P. M. Chaikin and T. C. Lubensky, *Principles of condensed matter physics* (Cambridge university press, Cambridge, 1995).
- [4] D. Y. Noh *et al.*, Phys. Rev. B **43**, 842 (1991).
- [5] A. Caillé, C. R. Acad. Sci. Ser. B **247**, 891 (1972).
- [6] J. Als-Nielsen *et al.*, Phys. Rev. B **22**, 312 (1980).
- [7] C. R. Safinya *et al.*, Phys. Rev. Lett. **57**, 2718 (1986).
- [8] A. J. Leadbetter, in *The molecular physics of liquid crystals*, edited by G. R. Luckhurst and G. W. Gray (Academic Press, London, 1979), Vol. 1, Chap. 13, pp. 284–316.
- [9] E. F. Gramsbergen and W. H. de Jeu, Liq. Cryst. **4**, 449 (1989).
- [10] P. G. de Gennes, Solid State Commun. **10**, 753 (1972).
- [11] *See e.g.* B. Jérôme, Rep. Prog. Phys. **54**, 391 (1991).
- [12] *See e.g.* C. Bahr, Int. J. of Modern Phys. **8**, 1 (1994).
- [13] R. Pindak, D. J. Bishop, and W. O. Sprenger, Phys. Rev. Lett. **44**, 1461 (1980).
- [14] J. Als-Nielsen, F. Christensen, and P. S. Pershan, Phys. Rev. Lett. **48**, 1107 (1982).
- [15] B. M. Ocko *et al.*, Phys. Rev. Lett. **57**, 94 (1986).
- [16] P. S. Pershan, J. Phys. **50**, 1 (1989).
- [17] J. W. M. Frenken and J. F. van der Veen, Phys. Rev. Lett. **85**, 134 (1985).
- [18] J. W. M. Frenken, H. M. van Pinxteren, and L. Kuipers, Surface Science **283**, 283 (1993).
- [19] G. Friedel, Ann. Phys. **18**, 273 (1922).
- [20] C. Y. Young, R. Pindak, N. A. Clark, and R. B. Meyer, Phys. Rev. Lett. **40**, 773 (1978).
- [21] C. Rosenblatt, R. Pindak, N. A. Clark, and R. B. Meyer, Phys. Rev. Lett. **42**, 1220 (1979).
- [22] *see e.g.* P. S. Pershan, *Structures of liquid crystals* (World Scientific, Singapore, 1988).
- [23] R. B. Meyer, Phys. Rev. Lett. **42**, 1220 (1979).
- [24] J. Pang and N. A. Clark, Phys. Rev. Lett. **73**, 2332 (1994).
- [25] E. B. Sirota, P. S. Pershan, L. B. Sorensen, and J. Collet, Phys. Rev. A **36**, 2890 (1987).
- [26] D. E. Moncton and R. Pindak, Phys. Rev. Lett. **43**, 701 (1979).
- [27] *See e.g.* E. I. Demikhov, Mol. Cryst. Liq. Cryst. **265**, 403 (1995).
- [28] R. H. yst, Phys. Rev. A **44**, 3692 (1991).

- [29] V. P. Romanov and A. N. Shalaginov, *Sov. Phys. JETP* **75**, 483 (1992).
- [30] *See e.g.* P. F. Micelli, *Physica A* **194**, 364 (1993).
- [31] *Surface x-ray and Neutron Scattering*, Vol. 61 of *Springer Proceedings in Physics*, edited by H. Zabel and I. K. Robinson (Springer-Verlag, Berlin, 1992).
- [32] D. K. Schwartz *et al.*, *Phys. Rev. A* **41**, 5687 (1990).
- [33] K. Kjeur *et al.*, *Phys. Rev. Lett.* **58**, 2224 (1987).
- [34] A. Braslau *et al.*, *Phys. Rev. Lett.* **54**, 114 (1985).
- [35] A. Braslau *et al.*, *Phys. Rev. A* **38**, 2457 (1988).
- [36] J. Als-Nielsen, in *Structure and Dynamics of Surfaces*, Vol. 2 of *Topics in current Physics*, edited by W. Schommers and P. von Blanckenhagen (Springer-Verlag, Berlin, 1986), Chap. 5, pp. 181–222.
- [37] T. P. Russel, *Mat. Science Reports* **5**, 171 (1990).
- [38] S. Gierlotka, P. Lambooy, and W. H. de Jeu, *Europhys. Lett.* **12**, 341 (1990).
- [39] D. J. Tweet *et al.*, *Phys. Rev. Lett.* **65**, 2157 (1990).
- [40] *See e.g.* J. Lekner, *Theory of reflectivity* (Nijhoff Publishers, Dordrecht, 1987), Vol. 61.
- [41] J. Als-Nielsen, in *Handbook on Synchrotron Radiation*, edited by G. Brown and D. E. Moncton (Elsevier Science Publishers, Amsterdam, 1991), Vol. 3, Chap. 12, pp. 471–505.
- [42] S. K. Sinha, *Physica B* **173**, 25 (1991).
- [43] M. L. Schlossman and P. S. Pershan, in *Light scattering by liquid surfaces and complementary techniques*, edited by D. Langevin (Marcel Dekker, New York, 1992), Vol. 2, Chap. 18, pp. 365–403.
- [44] B. Cull *et al.*, *Phys. Rev. E* **51**, 526 (1995).
- [45] S. K. Sinha, E. B. Sirota, S. Garoff, and H. B. Stanley, *Phys. Rev. B* **38**, 2297 (1988).
- [46] D. E. Savage *et al.*, *J. Appl. Phys.* **69**, 1411 (1991).
- [47] V. Holy and T. Baumbach, *Phys. Rev. B* **49**, 10668 (1994).
- [48] E. A. L. Mol, J. D. Shindler, A. N. Shalaginov, and W. H. de Jeu, *Phys. Rev. E* **54**, 536 (1996).
- [49] R. Schlatmann, J. D. Shindler, and J. Verhoeven, *Phys. Rev. B* **51**, 5345 (1995).
- [50] M. K. Sanyal, S. K. Sinha, K. G. Huang, and B. M. Ocko, *Phys. Rev. Lett.* **66**, 628 (1991).
- [51] L. G. Parrat, *Phys. Rev.* **95**, 359 (1954).
- [52] *See e.g.* M. Born and E. Wolf, *Principles of Optics* (Pergamon Press, Oxford, 1959).
- [53] H. Kiessig, *Ann. Phys.* **10**, 769 (1931).
- [54] *See e.g.* J. M. Cowley, *Diffraction Physics*, 2 ed. (North Holland Physics Publishing, Amsterdam, 1986).
- [55] I. W. Hamley and J. S. Pedersen, *J. Appl. Cryst.* **27**, 29 (1994).
- [56] Y. Yoneda, *Phys. Rev.* **131**, 2010 (1963).
- [57] P. Lambooy, *Order and disorder in thin films of liquid crystals and polymers* (Ph.D. thesis, Amsterdam, 1992).
- [58] J. D. Shindler and R. M. Suter, *Rev. Sci. Instrum.* **63**, 5343 (1992).
- [59] M. Versteeg, Spectrometer control program MV.
- [60] J. D. Shindler, E. A. L. Mol, A. N. Shalaginov, and W. H. de Jeu, *Phys. Rev. Lett.* **74**, 722 (1995).
- [61] W. H. de Jeu, J. D. Shindler, and E. A. L. Mol, *J. appl. cryst.* **29**, 511 (1996).
- [62] K. W. Evans-Lutterodt and M. T. Tang, *J. Appl. Cryst.* **28**, 318 (1995).
- [63] Beamline Handbook ESRF, 1994 and additional information from F. Rieutord.
- [64] F. Rieutord, personal communication.
- [65] E. Vlieg, to be published in *J. Appl. Cryst.*

- [66] P. P. L. Beliard *et al.*, *Physica A* **194**, 364 (1993).
- [67] A. Poniewierski and R. Hyst, *Phys. Rev. B* **47**, 9840 (1993).
- [68] A. N. Shalaginov and V. P. Romanov, *Phys. Rev. E* **48**, 1073 (1993).
- [69] R. Hyst, D. J. Tweet, and L. B. Sorensen, *Phys. Rev. Lett.* **65**, 2153 (1990).
- [70] G. Grinstein and R. A. Pelcovits, *Phys. Rev. A* **26**, 915 (1982).
- [71] G. Grinstein and R. A. Pelcovits, *Phys. Rev. Lett.* **47**, 856 (1981).
- [72] Y. Imry and L. Gunther, *Phys. Rev. B* **3**, 3939 (1971).
- [73] L. Gunther, Y. Imry, and J. Lajzerowich, *Phys. Rev. A* **22**, 1733 (1980).
- [74] I. S. Gradshteyn and I. M. Ryzhik, *Table of Integrals, Series and Products* (Academic Press, London, 1980).
- [75] G. S. Smith, C. R. Safinya, D. Roux, and N. A. Clark, *Molec. Cryst. Liq. Cryst.* **144**, 235 (1987).
- [76] I. M. Tidswell, T. A. Rabedeau, P. S. Pershan, and S. D. Kosowsky, *Phys. Rev. Lett.* **66**, 2108 (1991).
- [77] J. Daillant and O. B elorgey, *J. Chem. Phys.* **97**, 5824 (1992).
- [78] R. E. Geer, R. Shashidhar, A. F. Thibodeaux, and R. S. Duran, *Phys. Rev. Lett.* **71**, 1391 (1993).
- [79] R. E. Geer and R. Shashidar, *Phys. Rev. E* **51**, R8 (1995).
- [80] R. E. Geer, S. B. Q. R. Shashidar, A. F. Thibodeaux, and R. S. Duran, *Phys. Rev. E* **52**, 671 (1995).
- [81] P. Dutta and S. K. Sinha, *Phys. Rev. Lett.* **47**, 50 (1981).
- [82] A. Vrij, J. G. H. Joosten, and H. M. Fijnaut, in *Advances in Chemical Physics*, edited by I. Prigogine and S. A. Rice (Wiley and Sons, New York, 1981), Vol. 48, Chap. 6, pp. 329–395.
- [83] A. B ottger and J. G. H. Joosten, *Europhys. Lett.* **4**, 1297 (1987).
- [84] T. Stoebe, P. Mach, and C. C. Huang, *Phys. Rev. E* **49**, R3587 (1994).
- [85] P. Mach *et al.*, *J. Phys. II* **5**, 217 (1995).
- [86] C. C. Huang, personal communication.
- [87] M. R. Fisch, P. S. Pershan, and L. B. Sorensen, *Phys. Rev. A* **29**, 2741 (1984).
- [88] M. Benzekri, J. P. Marcerou, H. T. Nguyen, and J. C. Rouillon, *Phys. Rev. B* **41**, 9032 (1990).
- [89] T. P. Rieker and E. J. Janulis, *Liq. Cryst.* **17**, 681 (1994).
- [90] T. A. Lobko, B. I. Ostrovski, A. I. Pavluchenko, and S. N. Sulianov, *Liq. Cryst.* **15**, 361 (1993).
- [91] M. Knewtson, R. M. Suter, and J. D. Shindler, Reflectivity program SPEEDO.
- [92] Ch. Bahr, preprint 1996.
- [93] Ch. Bahr, personal communication.
- [94] T. C. Lubensky, *J. Chim. Phys.* **80**, 31 (1983).
- [95] D. R. Nelson and J. Toner, *Phys. Rev. B* **24**, 363 (1981).
- [96] M. Benzekri, T. Claverie, J. P. Marcerou, and J. C. Rouillon, *Phys. Rev. Lett.* **68**, 2480 (1992).
- [97] E. F. Gramsbergen and W. H. de Jeu, *J. Chem. Soc., Faraday Trans 2* **84**, 1015 (1988).
- [98] E. I. Demikhov, V. K. Delganov, and K. P. Meletov, *Phys. Rev. E* **52**, R1285 (1995).
- [99] T. Salditt, T. H. Metzger, and J. Peisl, *Phys. Rev. Lett.* **73**, 2228 (1994).
- [100] T. Salditt, T. H. Metzger, J. Peisl, and G. Goerig, *J. Phys. D: Appl. Phys.* **28**, A236 (1995).
- [101] J. Daillant, K. Quinn, G. Gourier, and F. Rieutord, *J. Chem. Soc., Faraday Trans.* **4**, 505 (1996).
- [102] T. Krancj and S.  zumer, *J. Chem. Phys.* **105**, 5242 (1996).

- [103] L. V. Mirantsev, Phys. Lett. A **205**, 412 (1995).
- [104] S. Garg and K. A. Crandell, Phys. Rev. E **48**, 1123 (1993).
- [105] P. Lambooy, S. Gierlotka, and W. H. de Jeu, in *Phase transitions in liquid crystals*, edited by S. Martellucci (A.N. Chester, New York, 1992), Chap. 17, pp. 239–243.
- [106] P. Mach and C. C. Huang, personal communication.
- [107] W. H. de Jeu and W. A. P. Claassen, J. of Chem. Phys. **67**, 3705 (1977).
- [108] W. H. de Jeu and W. A. P. Claassen, J. of Chem. Phys. **68**, 102 (1978).
- [109] A. N. Shalaginov, *to be published*.
- [110] A. Stroobants, H. N. W. Lekkerkerker, and D. Frenkel, Phys. Rev. Lett. **49**, 145 (1986).
- [111] W. L. McMillan, Phys. Rev. A **4**, 133 (1971).
- [112] D. Gouillon, G. Poeti, A. Skoulios, and E. Fanelli, J. Phys. Lett. **44**, L (1983).
- [113] W. L. McMillan, Phys. Rev. A **6**, 936 (1972).
- [114] E. F. Gramsbergen and W. H. de Jeu, J. Phys. **47**, 711 (1986).
- [115] Y. Takanishi, A. Ikeda, H. Takezoe, and A. Fukuda, Phys. Rev. E **51**, 400 (1995).
- [116] A. Scharkowski, H. Schmiedel, R. Stannarius, and E. W. huhn, Z. Naturforsch. **45a**, 37 (1989).
- [117] M. Schadt and P. R. Gerber, Z. Naturforsch. **37a**, 165 (1982).
- [118] T. P. Rieker and E. J. Janulis, Phys. Rev. E **52**, 2688 (1995).
- [119] *CHEM-X* for small molecule modelling, Chemical Design Ltd., Oxon, England.
- [120] H. T. Nguyen *et al.*, Liq. Cryst. **3**, 389 (1991).
- [121] E. P. Janulis *et al.*, Ferroelec. **85**, 375 (1988).

Summary

This thesis describes a series of experiments on freely suspended smectic-A films. To illustrate the nature of smectic liquid, we recall that in a solid, consisting of elongated molecules, the molecules are located on a three dimensional lattice, and all the long axes of the molecules will be aligned (long range order). This contrary to a liquid, in which all the molecules are totally disordered, both in their position and their orientation (only short range order). In a smectic-A liquid crystalline phase the axis of molecules are on average parallel, while the centres of mass are on average positioned in layers. However, the positional order is restricted to one direction, in the other two directions it is short range (“stacks of liquid layers”). The layering in a smectic phase is not truly long range, the positional correlation between two layers decays algebraically with distance. The decrease of the long range order is due to an increase in magnitude of the thermal fluctuations of the layers, that diverges with the size of the smectic system. The combination of this particular type of ordering and the unique ability of smectic films to hang freely suspended on a frame, makes smectic liquid crystals unique model systems.

In this thesis we describe a quantitative study of the thermal fluctuations in freely suspended smectic films. In the bulk these fluctuations are determined by the elastic constants for bending and compression of the layers K and B , respectively. An interesting feature of the freely suspended films is that they can be made varying from two (60 Å) to hundreds of layers (some μm) thick. Therefore, the ratio of surface and volume can be influenced. Because of the surface a third contribution to the fluctuations exists: the surface tension γ of the film. Depending the ratio γ/\sqrt{KB} the fluctuations at the surface of the film will be enhanced or compressed compared to the interior. We are particularly interested in the spectral dependence of the fluctuations. For large wavelengths “conformality”; is expected: top and bottom of a film fluctuate in unison. For short wavelengths they will fluctuate independently. The crossover depends on the elastic properties, surface tension and film thickness and can be modelled theoretically.

We have studied our films using specular and diffuse x-ray reflectivity. Specular reflectivity is well-known; x-rays, incident under angle θ on an interface between two media with different index of refraction are reflected under the same angle. In layered films such as the smectic phase, constructive or destructive interference of x-rays occurs as a function of the incoming angle, depending on the film thickness and the smectic layer periodicity. Due to the fluctuations, part of the x-rays is not reflected at angle θ , but under other angles; this scattering is diffuse. If the fluctuations from different smectic layers are correlated, the diffuse scattering will show the same interference pattern of the specular scattering. Thus, the interference pattern will directly show the degree of conformality of the film. In addition, by studying the diffuse scattering the hydrodynamical parameters B , K and γ can be obtained.

Two essentially different smectic systems are addressed. The first one consists of very stiff molecules, thus hard to compress (large B). As a result the whole film fluctuates conformally at all the length scales investigated. The other system, has been investigated close to the smectic-A-nematic phase transition, where B is rather small. In this case we observe the crossover from conformal to independent fluctuations. Another remarkable property of the latter system, is the ability to thin layer-by-layer when the temperature is raised just above the bulk smectic-nematic phase transition. Finally, we have also compared the fluctuational behaviour and the molecular formfactor of several chemically different liquid crystals.

Samenvatting

In dit proefschrift worden experimenten aan vrijstaande smectisch-A (SmA) films beschreven. De SmA fase behoort tot de vloeibaar kristallijne fase en heeft eigenschappen tussen die van vaste stoffen en vloeistoffen in. In vaste vorm bevinden de langgerekte moleculen zich in een drie dimensionaal rooster, terwijl de lange assen van de moleculen georiënteerd zijn. Er is lange afstands ordening. In vloeibare vorm zijn de moleculen wanordelijk verdeeld, zowel wat positie als orientatie betreft. In de SmA fase zijn de lange assen van de moleculen gemiddeld parallel, terwijl de zwaartepunten van de moleculen min of meer in lagen geordend zijn. Echter, deze positionele ordening is beperkt tot één richting, in de andere twee richtingen is er geen ordening. In die richtingen is een smectisch kristal te beschouwen als een vloeistof. De ordening van de lagen vertoont een verval met de afstand. De afwezigheid van echte lange afstands ordening is te wijten aan de grootte van de thermische fluctuaties in de lagen. Deze divergeren met de grootte van het smectisch systeem. De combinatie van deze bijzondere ordening en de unieke eigenschap van smectische films om vrij aan een “raam” te hangen (“smectisch” betekent zeep), maakt vloeibare kristallen tot unieke model systemen.

In dit proefschrift beschrijven we een studie van de thermische fluctuaties in vrijstaande SmA films. In de bulk SmA fase worden deze fluctuaties bepaald door de elastisch constanten voor buiging (K) en compressie (B) van de lagen. Opmerkelijk genoeg kunnen vrijstaande films gemaakt worden variërend in dikte van twee (60 Å) tot honderden (enkele μm) lagen. Hierdoor kan de verhouding tussen oppervlakte en volume beïnvloed worden. Om dit effect in rekening te brengen, bestaat een derde bijdrage aan de thermische fluctuaties: de oppervlakte spanning γ van de film. Afhankelijk van de verhouding γ/\sqrt{KB} zullen de fluctuaties aan het oppervlak worden onderdrukt dan wel versterkt ten opzichte van lagen binnen in de film. Wij zijn in het bijzonder geïnteresseerd in de spectrale afhankelijkheid van de fluctuaties. Voor grote golflengtes wordt “conformaliteit” verwacht; top en bodem van de film fluctueren in fase. Bij kortere golflengte zullen ze onafhankelijk fluctueren. De overgang hangt af van de elastische eigenschappen, de oppervlakte spanning en de dikte van de film, en kan theoretisch gemodelleerd worden.

We hebben de films bestudeerd met speculaire en diffuse röntgenreflectiviteit. Speculaire reflectiviteit is algemeen bekend; röntgenstraling valt onder een hoek θ op een oppervlakte tussen twee media met een verschil in brekingsindex en wordt onder gelijke hoek gereflecteerd. In gelaagde systemen, zoals een SmA film, zal constructieve en destructieve interferentie optreden als functie van de invalshoek, afhankelijk van de film- en laag dikte. Door de fluctuaties zal een deel van de straling niet gereflecteerd worden onder een hoek θ , maar onder andere hoeken; deze verstrooiing is diffuus. Als de fluctuaties van verschillende smectische lagen gecorreleerd zijn, zal de diffuse verstrooiing een vergelijkbaar interferentie patroon vertonen als de speculaire reflectiviteit. Uit dit patroon kan de mate van conformaliteit worden bepaald. Tevens kunnen de constanten B , K en γ worden bepaald.

Twee geheel verschillende systemen worden behandeld. Het eerste bestaat uit starre moleculen, en dus is de film moeilijk samen te drukken (B is groot). Daardoor fluctueren alle lagen in de film conformeel over alle bestudeerde golflengtes. Het andere systeem werd dicht bij de smectisch-nematisch fase overgang bestudeerd, waar B klein is. In dit geval werd de overgang naar onafhankelijke fluctuaties waargenomen. Een opmerkelijke eigenschap van dit laatste systeem is dat de film laag voor laag dunner wordt als de temperatuur juist boven de bulk fase temperatuur wordt verhoogd. Tenslotte hebben we de het gedrag van de fluctuaties en de moleculaire vormfactor van een aantal chemisch zeer verschillende moleculen bestudeerd.

Bedankt!

Wim de Jeu, Daan Frenkel, Joe Shindler, Arcadi Shalaginov, Gerard Wong, Blaindine Jerome, Roland Meister, Rutger Schlatmann, Willem Jan Huisman, Jan Commandeur, Paul Schuddeboom, Richard Sear, Bela Mulder, Levent Demirel, Wim Bouwman, Peter Lambooy, Elias Vlieg, Rene Koper, Steven de Vries, Peter Bolhuis, Maarten Hagen, Alfons van Blaaderen, Joost Frenken, Wim Brouwer, Wim Barsingerhorn, Henk Neerings, Ruud Boddenberg, Herman Ficke, Illiya Cerjak, Dick Glastra van Loon, Jan van Elst, Ben Okhuizen, C. C. Huang, Dr. Eidenschink, Christiaan Bahr, François Rieutord, Jean-Marc Petit, Rolf Simon, Willem Kegel, Marianne Westendorp, Saskia Verdurmen, Jacco Farla, Andre van Kuijk, Carsten Byrman, Klaas Jan van den Berg, Edwin Kellerbach, Joke Timmerman, Ronald Knechtel, Agnes Peels, Petra van der Ree, Sylvia Mellenberg, Chris Hendrycks, Sandra Mol, Joost Mol, Kjell Swedborg, Åsa Brännström, Billy Byatt

CURRICULUM VITAE

De auteur van dit proefschrift werd geboren op 14 augustus 1967 in Breda. Vanaf 1979 bezocht zij het Mgr. Frencken College in Oosterhout, waar in 1985 het diploma werd behaald. Aansluitend studeerde zij scheikunde aan de toenmalige Rijksuniversiteit Utrecht. Het propaedeutisch examen werd behaald in 1987 en het doctoraal examen, met als afstudeerrichting Fysische- en Colloïd chemie, in 1991. Voorafgaand aan haar promotie volbracht de auteur een negen maanden durend onderzoek in de groep van dr. P. Claesson aan Ytkemiska Institutet in Stockholm. Sinds september 1992 is de auteur als onderzoeker in opleiding verbonden aan het FOM-instituut voor Atoom- en Molecuulfysica (AMOLF) te Amsterdam, waar het in dit proefschrift beschreven onderzoek tot stand kwam.